Spin Hall nano-oscillator arrays: towards GHz neuromorphics

Mohammad Zahedinejad

UNIVERSITY OF GOTHENBURG

Doctoral Dissertation in Physics

Department of Physics
University of Gothenburg
412 96 Gothenburg, Sweden

September 27, 2019

ISBN: 978-91-7833-572-5 (printed)
ISBN: 978-91-7833-573-2 (pdf)
URL: http://hdl.handle.net/2077/61238

Cover: Schematic representation of a 4×4 SHNO array with $(w, p) = (120, 300)$. The schematic shows the direction of the applied magnetic field (H), in-plane component (H_{IP}) and the charge current direction. The black orbiting arrows indicate the precessing magnetization of each nano–constriction. The Pt, Hf, and NiFe layers are colored gray, red, and blue and their thickness is shown in nm.

Printed by Brandfactory AB, Gothenburg, 2019

Typeset using LuaLaTeX

"We carry inside us the wonders we seek outside us."

RUMI

Abstract

This thesis explores the vibrant phenomena of spin Hall nano–oscillators (SHNOs); from wideband oscillation at the GHz range, through propagating spin–wave emission, to mutual synchronization in two–dimensional SHNO arrays, and tries to lay the foundation for a far-reaching SHNO technology, targeting magnonics, microwave signal generation, and neuromorphic computing.

After a short introduction to the theoretical background in Chapter 1, in Chapter 2, ways of improving the spin transport properties between NiFe and Pt are explored: an 0.4 nm ultra–thin layer of Hf at the NiFe/Pt interface is found to reduce the threshold current by 20% as a result of the change in spin mixing conductance $G_{\text{eff}}^{\uparrow\downarrow}$. Then, W/CoFeB/MgO stacks with perpendicular magnetic anisotropy (PMA) are used to demonstrate wide frequency tunability and sub–mA threshold currents in CMOS compatible SHNOs. By further increasing the PMA, the auto–oscillation frequency exceeds the ferromagnetic resonance (FMR) frequency, turning the SHNO into a propagating spin–wave emitter in which the propagation wave–vector is tunable with applied current and field. Finally, a GHz nano-scale SHNO modulated by an 80 MHz radio–frequency (RF) current is presented. The modulation needs no bulky microwave mixer, promising a compact modulator unit.

Chapter 3 introduces two–dimensional SHNO arrays. Robust mutual synchronization is demonstrated in arrays accommodating up to 64 oscillators, achieving record high quality factors of 170,000 at an operating frequency of 10 GHz. Injection of two external microwave signals reproduces the two-dimensional synchronization maps used in neuromorphic vowel recognition.

Chapter 4 emphasizes the importance of individual SHNO control in arrays. Gated SHNOs are demonstrated with substantial voltage tuning of the threshold current and the SHNO frequency. Voltage controlled mutual synchronization is also demonstrated. The $MgO/AlO_x/Si_3N_4$ gate is found to exhibit a memristive behavior governed by ion migration and acts as an embedded memory making each SHNO a complete non-volatile oscillator with integrated weights. The exciting nature of coupled non-volatile oscillator arrays controlled by electric field could lead to a paradigm shift in non–conventional computing.

Chapter 5 discusses the implications of the demonstrated SHNO technology and how it may impact future applications.

Keywords: spin Hall effect, spin Hall nano-oscillators, microwave, spin wave, synchronization, neuromorphic computing, memristor.

Contents

Abstract v

Table of Contents vi

List of Figures ix

List of Symbols and Abbreviations xi

Publications xv

Acknowledgments xvii

Introduction 1

1 Background and methods 5
- 1.1 Theoretical background . . . 5
  - 1.1.1 Anisotropic magnetoresistance . . . 5
  - 1.1.2 The spin Hall effect . . . 5
  - 1.1.3 Dynamic properties of magnetization . . . 6
  - 1.1.4 Perpendicular magnetic anisotropy . . . 8
  - 1.1.5 Spin Hall nano-oscillators . . . 9
  - 1.1.6 Frequency–amplitude non–linearity . . . 11
  - 1.1.7 Synchronization in SHNO . . . 11
  - 1.1.8 Memristors . . . 15
- 1.2 Methods . . . 16
  - 1.2.1 SHNO fabrication . . . 16
  - 1.2.2 Choice of substrate and thin film deposition . . . 16
  - 1.2.3 Optical lithography . . . 17
  - 1.2.4 Electron beam lithography . . . 18
  - 1.2.5 Ion beam etching . . . 21
  - 1.2.6 Defining the measurement contacts . . . 22
  - 1.2.7 Characterization techniques . . . 23

2 CMOS-compatible spin Hall nano-oscillators 27
- 2.1 Hafnium dusting of NiFe/Pt SHNOs . . . 27
  - 2.1.1 Fabrication of NiFe/Hf/Pt ST-FMR samples . . . 28
  - 2.1.2 Characterization of the NiFe/Hf/Pt samples . . . 29
- 2.2 CoFeB-based spin Hall nano-oscillators . . . 31

2.2.1 Characterization of the W/CoFeB/MgO devices 32
2.3 Propagating spin waves in CoFeB–based spin Hall nano-oscillators 35
2.3.1 Device characterization 36
2.4 Current modulation of spin Hall nano oscillator 38

3 Two-dimensional spin Hall nano-oscillator arrays 43
3.1 Fabrication of 2D SHNO arrays 44
3.2 Microwave measurements on 2D SHNO arrays 45
3.3 Neuromorphic computing using 2D SHNO arrays 51

4 Voltage controlled SHNOs: The oscillator remembers 55
4.1 Sample fabrication 56
4.2 Electrical measurement I: Voltage controlled PMA and damping 58
4.3 Electrical measurement II: The gate is a memristor 59
4.4 Electrical measurement III: Memristive control of mutual synchronization 62

5 Future approaches and prospects 65

Bibliography 69

List of Figures

1.1 Representation of the magnetization vector in an applied magnetic field. 7
1.2 Different types of SHNO devices. 10
1.3 Mechanical model of coupled oscillators 12
1.4 The first memristor proposed by HP. 16
1.5 AFM microscopy of a fabricated SHNO surface. 19
1.6 Electron-beam lithography of an 80 nm wide SHNO. 19
1.7 Comparison of EBL for SHNO chains for maN-2400 and HSQ electron resists. 20
1.8 a sub-20 nm SHNO fabricated using HSQ electron resist. 21
1.9 Comparison of the high-contrast and standard EBL processes for HSQ. 22
1.10 Optical microscope image of the fabricated CPW to measure the SHNO 23
1.11 ST-FMR measurement setup schematic 24
1.12 Schematic of AO measurement setup. 25

2.1 Hf thickness-dependency of AMR 28
2.2 Extracted parameters from ST-FMR characterization for Pt/Hf/NiFe stacks. 29
2.3 Spin Hall efficiency and normalized current density versus Hf thickness 30
2.4 AGM characterization of W/CoFeB/MgO stack. 32
2.5 Three-dimensional schematic of the W/CoFeB/MgO SHNO . . 33
2.6 Microwave characterization of a W/CoFeB/MgO-based SHNO. 34
2.7 AO response to the OOP angle and the magnetic field sweep . 35
2.8 Nonlinearity as a function of PMA and $\mu_0 H$. 36
2.9 Micromagnetic simulations of propagating SW. 37
2.10 SHNO current modulation setup and experimental results. . . . 39
2.11 RF Modulation of the SHNO for different SHNO operating points 40

3.1 Schematic representation of a 4×4 SHNO array. 44
3.2 SEM images of two-dimensional SHNO arrays. 45
3.3 AO PSD measurements for SHNO arrays. 46
3.4 PSDs and BLS line scans showing synchronization along chains. 47
3.5 The 4×4 SHNO array measured at $\theta = 82°$. 48
3.6 Linewidth and peak power analysis of the 4×4 SHNO array. . . 49

3.7 Linewidth and peak power values for SHNO arrays in synchronized state. 50
3.8 Synchronization map of a 4×4 SHNO array for two input microwave signals 52

4.1 VSM measurement of W/$(Co_{0.75}Fe_{.25})_{75}B_{25}$ (t)/MgO/AlO_x stacks. 57
4.2 Schematic of the gated SHNO alongside optical SEM images of the fabricated device. 58
4.3 AO measurements, extracted damping, and frequency change for gated SHNOs. 59
4.4 Memristive switching of the fabricated gate on the SHNO. . . . 60
4.5 Memristive gate behavior on the AO of the SHNO. 61
4.6 PSD for SHNO *vs.* I_{SHNO} with no applied gate voltage. 62
4.7 Synchronization of SHNOs via memristor gate. 63

List of Symbols and Abbreviations

List of Symbols

α	Gilbert damping constant
H, H_{ext}	external magnetic field
I_{dc}	bias current
H_{ext}	external magnetic field
M_{eff}	effective magnetization
H_{ex}	exchange field
H_A, H_k	anisotropy field
H_{int}	internal magnetic field
θ_H	external magnetic field angle
θ_{int}	out-of-plane angle of the magnetization
θ_{SH}	spin Hall angle
Ψ_{IP}	in-plane angle
M	magnetization
M_s	saturation magnetization
p	spin polarization
R_P	resistance in the parallel state
R_{AP}	resistance in the antiparallel state
ρ	resistivity
f_{FMR}	ferromagnetic resonance frequency
$\Delta\varphi$	relative phase shift
$TMAH$	Tetra Methyl Ammonium Hydroxide
J_e	charge current density
J_s	spin current density
$G_\mathrm{eff}^{\uparrow\downarrow}$	effective spin-mixing conductance

List of Physical Constants

$\gamma/(2\pi)$	gyromagnetic ratio of an electron	$28.024\,\mathrm{GHz/T}$
μ_0	vacuum permeability	$4\pi \times 10^{-7}\,\mathrm{V\,s/(A\,m)}$
μ_B	Bohr magneton	$9.274 \times 10^{-24}\,\mathrm{J/T}$
e	elementary charge	$1.602 \times 10^{-19}\,\mathrm{C}$
$\hbar$	reduced Planck constant	$1.055 \times 10^{-34}\,\mathrm{J\,s}$

List of Abbreviations

AFM	atomic force microscopy
CMOS	complementary metal-oxide semiconductor
STT	spin transfer torque
GSG	ground-signal-ground
STO	spin torque oscillator
SHNO	spin Hall nano-oscillator
SW	spin wave
HM	heavy metal layer
PSW	propagating spin wave
MR	magnetoresistance
GMR	giant magnetoresistance
TMR	tunneling magnetoresistance
AMR	anisotropy magnetoresistance
μ-BLS	microfocused Brillouin light scattering
dc	direct current
ac	alternating current
FM	ferromagnetic layer
HM	heavy metal layer
NM	normal metal layer
MTJ	magnetic tunnel junction
NP	nanopillar
NC	nanocontact
PMA	perpendicular magnetic anisotropy
NCSTO	nanocontact spin-torque oscillator
SHE	spin Hall effect
SHA	spin Hall angle
LLGS	Landau–Lifshitz–Gilbert–Slonczewski
FMR	ferromagnetic resonance
LNA	low-noise amplifier
FWHM	full width at half maximum
DUT	device under test
VBW	video bandwidth
RBW	resolution bandwidth
EBL	electron beam lithography
SEM	scanning electron microscope
IBE	ion beam etching
SIMS	secondary ion mass spectroscopy
RIE	reactive ion etching
IP	in-plane
OOP	out-of-plane
μ-BLS	micro-focused Brillouin light scattering
$\beta-$W	β phase tungsten
HfO	Hafnium oxide
MgO	Magnesium oxide
TaO	Tantalum oxide

List of Abbreviations (continued)

CoFeB	Cobalt–Iron–Boron
HSQ	Hydrogen silsesquioxane
NaOH	Sodium hydroxide
NaCl	Sodium chloride
MRAM	Magnetoresistive random-access memory
BEOL	Back end of line
VSM	vibrating sample magnetometer
AGM	alternating gradient magnetometer
SiO_2	Silicon dioxide
AO	auto–oscillation
PSD	power spectral density

Publications

List of papers and manuscripts included in this thesis:

I Mazraati, H., **Zahedinejad, M.**, Åkerman, J., "*Improving the magnetodynamical properties of NiFe/Pt bilayers through Hf dusting*", Applied Physics Letters **113**, 092401 (2018).

Contributions: Fabrication of the samples, Electrical measurement. Contributed to writing the manuscript.

II **Zahedinejad M.**, Mazraati, H., Fulara, H., Yue, J., Jiang, S., Awad, A.A, Åkerman, J., "*CMOS compatible W/CoFeB/MgO spin Hall nano-oscillators with wide frequency tunability*", Applied Physics Letters, **112**, 132404 (2018).

Contributions: Sample fabrication, Electrical measurement, data analysis. Contributed to writing the manuscript.

III Fulara, H., **Zahedinejad, M.**, Khymyn, R., Awad, A. A., Muralidhar, S., Dvornik, M., Åkerman, J., "*Spin–Orbit–Torque Driven Propagating Spin Waves*", available on arxiv (2019), Manuscript accepted for publication in Science Advances.

Contributions: Fabrication of the samples, electrical measurements. Contributed to writing the manuscript.

IV **Zahedinejad, M.**, Awad, A.A., Dürrenfel, P., Houshang, A., Yin, Y., Muduli, P.K., Åkerman, J., "*Current modulation of nanoconstriction spin-hall nano-oscillators.*", IEEE Magn. Lett. **8**, 1 (2017).

Contributions: Electrical measurement, data analysis, developing the model. Contributed to writing the manuscript.

V **Zahedinejad, M.**, Awad, A. A., Muralidhar, S., Khymyn, R., Fulara, H., Mazraati, H., Dvornik, M., Åkerman, J., "*Two-dimensional mutually synchronized spin Hall nano-oscillator arrays for neuromorphic computing*", available on arxiv (2018), Manuscript submitted to Nature Nanotechnology.

Contributions: Fabrication of the samples, electrical measurement, and data analysis. Contributed to writing the manuscript.

VI Fulara, H., **Zahedinejad, M.**, Khymyn, R., Dvornik, M., Fukami, S., Kanai, S., Ohno, H., Åkerman, J., "*Large voltage-tunability of spin*

Hall nano-oscillator threshold current and frequency", Manuscript in preparation.

Contributions: Fabrication of the samples, electrical measurements, and data analysis. Contributed to writing the manuscript.

VII **Zahedinejad, M.**, Fukami, S., Kanai, S., Ohno, H., Åkerman, J., "*Memristive control of mutual SHNO synchronization for neuromorhphic computing*", Manuscript in preparation.

Contributions: Design and fabrication of the samples, electrical measurements, and data analysis. Contributed to writing the manuscript.

List of papers related to, but not included in this thesis:

1 Albertsson, D. I., **Zahedinejad, M.**, Åkerman, J., Rodriguez, S., Ruso, A. "*Compact Macrospin-Based Model of Three-Terminal Spin-Hall Nano Oscillators*", IEEE Transaction on Magnetics, 1-8 (2019). DOI: 10.1109/TMAG.2019.2925781

2 Zarei, S., **Zahedinejad, M.**, Mohajerzadeh, S. "*Metal-assisted chemical etching for realisation of deep silicon microstructures*", Micro & Nano Letters ,(2019). DOI: 10.1049/mnl.2019.0113

3 Jiang, S., Khymyn, R., Chung, S., Le, QT., Herrera Diez, L., Houshang, A.,**Zahedinejad, M.**, Ravelosona, D., Åkerman, J., "*Tuning spin torque nano-oscillator nonlinearity using He+ irradiation*", available on arxiv (2018), Manuscript submitted to Physical Review Applied.

4 Mazraati, H., Muralidhar, S., Etesami, SR., **Zahedinejad, M.**, Banuazizi, SA,, Chung, S., Awad, AA., Dvornik, M., Åkerman, J., "*Mutual synchronization of constriction-based spin Hall nano-oscillators in weak in-plane fields*", available on arxiv (2018), Manuscript submitted to Physical Review Applied.

Acknowledgments

It has been a fantastic four years of my life that I had the pleasure to work with many wonderfully talented people. This thesis is the result of their fruitful collaborations and insights.

Like any other big change in life, moving abroad, starting Ph.D. in physics while having an engineering mindset challenged me in a way I had never experienced before. I never deny that, in the beginning, I thought of quitting my job as I did not find myself as a good fit. But, I survived and eventually loved what I was doing. My scientific survival was not possible without Johan Åkerman, my supervisor. Though many people may like otherwise, I was never micromanaged by Johan to do my research. I was allowed to do what I felt is more fun, and nothing is more fun than independency. Do not get me wrong, he was always there to discuss, to listen, to advice, to criticize, and to be criticized. Apart from the scientific journey and accomplishments, if any, my Ph.D. study period has reshaped and challenged my character. If there is one rule which I have learned, that is "try to be a coachable person", no matter where I stand in the carrier ladder. The four years of working with Johan has impacted my attitude to "*never give up until it works*". Thank you, Johan. I always stick to the change you made on my vision.

My boundless gratitude also goes to my co–advisor Ahmad Awad, who thought me everything from scratch ever since I joined the group. Ahmad helped my a lot to get on–board and his bright mind always had something to advice when I needed him. I would like to thank all other senior colleagues Mykola Dvornik, Roman Khymyn, Mohammad Haidar, Martina Ahlberg, Sunjae Chung, Sheng Jiang, and of course Fredrik Magnusson from NanOsc AB.

I am grateful for having Shreyas Muralidhar, Afshin Houshang, Hamid Mazraati, and Philipp Dürrenfeld who were always there for me anytime I needed them. I felt welcome asking for any favor, and I treasure their company. My special thanks go to Himanshu Fulara, who helped me a lot during our two years of collaboration. His never-ending stamina and contribution have led to more than half of the papers included in this thesis.

I feel so blessed to have Raimund Feifel as my examiner. He is an absolutely thoughtful and kind person who does his best to help out the Ph.D. candidates throughout their studies. I cannot thank Bea Tensfeldt and Pernilla Larsson enough for constantly welcoming me to their offices with endless administrative requests I had. You do such a great job day in, day out! Keep it up.

All those fantastic sample images you see in this thesis were not even imaginable without the wonderful scientists of MC2 cleanroom. Without any

doubt, MC2 cleanroom is one of the best cleanrooms in Europe thanks to the commitment and endeavor of MC2 staff. I would especially like to thank Johan Karl Andersson, Marcus Rommel, Niclas Lindvall, Mats Hagberg, Henrik Frederiksen, Bengt Nilsson, and Göran Alestig, among many others. I appreciate your patience and kindness in training and backing me up.

To many friends I have out there, you have made my life enjoyable by your kindness and support. I would like to especially thank Saeed Taheri, Nastaran Dashti, Shahrzad Shams, Nima Sasanian, Moin Hadian, Mahdi Rahman, and Hamed Vavadi. Words cannot express my feelings, nor my thanks for all your companion.

And to my lovely family. This thesis is the least I can dedicate to appreciate your boundless love. My lovely mother, thank you for your passion and love. I hope someday that I am at least half the person you are. To my Dad, who never gave up believing in me, I dedicate this thesis to all the dreams you had for me, and now they have come true. Love you, Dad. To my lovely sister, Elahe, who I missed the most, and my brothers, Ali and Ehsan, you all have been my role models throughout my life. Thank you for your unconditional support and love. And finally, I dedicate this thesis to my strong warrior, my best friend, and my treasure, Shima. As John Nash says, "*You are the only reason I am. You are all my reasons.*" You gave me a thousand reasons to fight for having you by my side, while we lived a thousand miles away from each other.

Introduction

As we approach the era of the Internet of Things (IoT), communication systems and processing hardware are advancing together to meet the requirements of multiple converging technologies, including real-time analysis, wirelessly connected sensors, machine learning, connected objects, and embedded systems. Following Moore's Law, recent technological advances in the microelectronics industry have led to unprecedented improvements in processing speed and power consumption, by pushing CMOS technology to ever smaller nodes. However, with the looming end of Moore's Law and the increasing demand for higher speeds in mobile applications, we are on the verge of a new revolutionary technology that will replace the model of Von Neumann computing that has ruled the industry for over fifty years. In particular, emerging paradigms—such as big data and machine learning for connected objects—require the storage and handling of enormous amounts of data, which must then be fed to processing units running on massive CPU or GPU clusters or cloud–based computing platforms. Compared to what will be required for such systems, even current state-of-the-art processing, storage, and wireless units will seem bulky, power-hungry, and slow in the very near future.

The field of spintronics, which revolutionized the mass storage industry in the late 1990s with the discovery of GMR [1, 2], has been actively addressing these challenges. Spin transfer torque magnetic random access memory (STT-MRAM) has been recognized by Intel and Samsung [3, 4] as an appealing candidate for a fast, nonvolatile replacement for embedded flash, which is facing insurmountable scaling challenges. It also holds great promise even for the realization of universal memory [5–7]. Extensive research by the spintronics community has aimed at achieving nanoscale spin-based microwave components, such as microwave generators [8–11], rectifiers [12], spin diodes [13], spin–wave generators [14, 15], and modulators [16–23], which could be used as building blocks of communication systems.

Spin transfer torque (STT) and spin-orbit torque (SOT) driven oscillators are promising candidates for such next–generation microwave devices. Studies of STT-driven oscillators in extended magnetic layers have shown the existence of high-frequency SWs [24], including propagating SWs [25–28], SW localized SW modes [29–31], and magnetic droplets [32, 33]. In such devices, the magnetodynamics is excited when the spins produced by the ferromagnetic spin polarizer layer pass through a spin transparent layer and reach the adjacent magnetic free layer. Spin valves (SV) and magnetic tunnel junctions (MTJ) are examples of such devices.

However, the main issue with spin–based microwave components is the low

level of output power and the high level of phase noise. Synchronization of multiple oscillators has been proposed to mitigate both these drawbacks [8, 34–36]. Synchronizing many STT oscillators involves a number of significant fabrication challenges. With SOT and the spin Hall effect (SHE) attracting more attention, a new concept of oscillators driven by pure spin current has been proposed in the form of spin Hall nano-oscillators (SHNOs) [37, 38]. While SHNOs face the same challenges as STT oscillators in terms of output power and coherency, they offer a realistic path towards much larger ensembles of synchronized oscillators. Synchronization of nine SHNOs was demonstrated in 2017 [9], achieving a dramatic increase in the output power and improvement in the signal coherency. Thanks to their open geometry, the magnetodynamics in SHNOs can also be studied directly by optical means, such as BLS [9, 39] and Kerr microscopy [40, 41].

This thesis investigates a number of approaches and geometries in order to study SHNOs for applications such as CMOS compatible wideband microwave signal generation, signal modulation, emission of propagating SWs, and neuromorphic computing. Through the synchronization of two-dimensional SHNO arrays, the thesis explores an efficient approach to remarkably coherent microwave signals. In two-dimensional SHNO arrays, an individual SHNO operating at a gigahertz frequency is coupled to neighboring SHNOs, imitating the oscillatory behavior of neurons connected to their neighbors via synapses. There are proposals to use coupled oscillators network as ultrafast and efficient non-Von Neumann computing paradigms for a range of applications [42–51]. Implementing such paradigms will transform spintronics in a technology capable of providing all the pieces of the IoT puzzle, from fast memory to ultra–compact communication systems and processing units.

The thesis is organized as follows:

Chapter 1 presents an introduction to the underlying physics needed to understand and explain the experimental results presented in the later chapters. The chapter provides schematic illustrations of the measurement techniques and setups to help readers grasp the measurement conditions and the notation used throughout the thesis. A brief introduction to the Kuramoto model for coupled synchronized oscillators is provided to familiarize readers with synchronization phenomena. The fabrication processes and materials developed by us for micro-nano-fabrication are explained and compared with conventional methods. Where further processing steps are needed for a device, a detailed description of these steps is provided in the section introducing the device.

Chapter 2 begins with a description of the Hf dusting of the NiFe/Pt interface, which helps achieve a lower Gilbert damping constant, with a direct impact on the auto-oscillation (AO) threshold current in both the SHNO and in two-dimensional SHNO arrays. We then describe the physics behind modulating the damping constant. An SHNO based on W/CoFeB/MgO is then introduced; in this device, a record high spin Hall angle of 53% is obtained, leading to a significantly improved threshold current. Such devices show large frequency tunability thanks to the moderate perpendicular magnetic anisotropy (PMA) at the CoFeB/MgO interface. We later discuss how introducing substantial

PMA pushes the AO frequency to exceed the ferromagnetic resonance (FMR) frequency. As a result, the localized SW mode becomes a propagating SW mode, which is an exciting phenomenon for magnonic and wave-based computing. The chapter concludes with a promising application of SHNOs as signal modulators. An SHNO operating in the GHz regime is modulated at 80 MHz and its modulation behavior modeled analytically for use in designing the demodulator at the receiver end.

Chapter 3 introduces two–dimensional SHNO arrays in a range of sizes; a record quality factor of $Q = 170{,}000$ is achieved for the largest array of 8×8 synchronized SHNOs operating at 10 GHz. An analysis of linewidth and peak power versus the number of synchronized SHNOs, N, shows perfect N^{-1} scaling for the linewidth. The peak power, however, does not follow N^2 scaling, instead experiencing a rollover caused by the phase shift among the SHNOs. The chapter discusses how the complex nature of coupled oscillators would open up new approaches to bioinspired and neuromorphic computing.

Chapter 4 describes a route towards controlling the frequency of an SHNO and the coupling between SHNOs using a gating mechanism. The electric field supplied by the gating has a direct effect on both the PMA and the damping, which alters the operating frequency and the threshold current of the SHNO. Controlling individual oscillators is an essential part of computing based on oscillatory networks, where it is needed to allow inputs to the system and to alter the state of the artificial neuronal activities. Our gating structure also operates as an embedded memristor that controls the SHNO frequency. This memristor associates the SHNO frequency with its internal resistance state, acting as a short-term memory element.

Chapter 5 summarizes the entire thesis and discusses the prospects of the SHNO devices described throughout the thesis.

1

Background and methods

1.1 Theoretical background

1.1.1 Anisotropic magnetoresistance

Magnetoresistance (MR) is a property of materials that causes their electrical resistance to change when an external magnetic field is applied. This phenomenon is more common in ferromagnetic (FM) materials. MR can arise in magnetic materials from a variety of effects, including negative magnetoresistance and anisotropic magnetoresistance (AMR) [52]. In multilayer ferromagnetic systems, MR can have other origins, such as giant magnetoresistance (GMR) [53] and tunneling magnetoresistance (TMR) [54], which are both stronger effects than AMR. Throughout this thesis, we use only AMR. However, all results and devices presented in the thesis may later be further enhanced using either GMR or TMR.

AMR refers to a change in a material's resistance caused by the relative orientations of magnetic moments and of the current passing through the material; this is a phenomenon that emerges from the spin-orbit interaction. In AMR, the resistance of the material is at a maximum when the current and magnetization are in a parallel configuration, and at a minimum when perpendicular. For a typical thin ferromagnetic layer, the AMR value is less than 1% at room temperature [55]; however, in emerging semimetal topological materials, it can reach a few hundred percent [56]. The resistivity can then be described through the angular dependency:

$$\rho = \rho_{\perp} + (\rho_{||} - \rho_{\perp})\cos^2\theta, \tag{1.1}$$

where $\rho_{\perp}$ and $\rho_{||}$ stand for the resistivities with the magnetization respectively parallel and perpendicular to the direction of the current; θ is the relative angle between the magnetization and the current. The AMR value is finally defined as the ratio $(\rho_{||} - \rho_{\perp})/\rho_{\perp} \times 100$, expressed as a percentage.

1.1.2 The spin Hall effect

What is now called the spin Hall effect (SHE) was predicted in 1971 by two Russian scientists, M. I. Dyakonov and V. I. Perel, who also introduced the

term “spin current” [57, 58]. The term “spin Hall effect”, was introduced by Hirsch in 1999 [59]. About a century prior to that, E. H. Hall had discovered the normal Hall effect, in which a charge current is generated in a conductor upon applying crossed electric and magnetic fields. Caused by the Lorentz force, the generated charge current is transverse to both applied fields. Analogous to the normal Hall effect, the SHE emerges as a pure spin current transverse to the applied electric field in the absence of the applied magnetic field. The spin Hall effect was experimentally demonstrated in 1984 by Bakun et al. [60], about a decade after its prediction. A consequence of this phenomenon is the accumulation of spin-up and spin-down electrons moving in opposite directions, with no overall charge current; this can be considered a flow of spin angular momentum.

The SHE is more dominant in certain nonmagnetic metals with strong spin-orbit interactions, such as platinum (Pt) [61], tungsten (W) [55, 62, 63], tantalum (T) [64], and palladium (Pd) [65], but is not limited to these materials, as there are many emerging materials being discovered, including topological insulators [66] and heavy metal alloys [67], that show very large spin Hall angle values.

The spin Hall angle (θ_{SH}) of a material is therefore the effective ratio at which the charge current is converted into a pure transverse spin current. It is defined as $\theta_{\mathrm{SH}} = J_{\mathrm{s}}/J_{\mathrm{e}}$, where $(\hbar/2e)J_{\mathrm{s}}$ and J_{e} are the spin and charge current densities, respectively. The spin Hall angle can take a positive or negative value, depending on whether the magnetic moment of the generated spins rotating around the charge current follows the right-hand or the left-hand rule.

1.1.3 Dynamic properties of magnetization

A magnetic moment experiences a torque τ when an applied magnetic field $\boldsymbol{H}$ acts so as to bring the moment and the H vector into alignment. This torque can be expressed as $\tau = \boldsymbol{m}\times\boldsymbol{H}$. Considering the classical mechanical approach, torque is defined as the time evolution change in angular momentum $\boldsymbol{L}$, described as $\tau = \frac{\partial \boldsymbol{L}}{\partial t}$. The angular momentum from which the electron's magnetic moment arises is given by:

$$\boldsymbol{m} = -\gamma \boldsymbol{L}, \tag{1.2}$$

where γ is a material-dependent constant called the gyromagnetic ratio. Taking the time derivative of Eq. 1.2 results in the precessional term of the magnetization dynamics:

$$\frac{\partial \boldsymbol{m}}{\partial t} = -\gamma(\boldsymbol{m} \times \boldsymbol{H}) \tag{1.3}$$

This equation can also be used for the macroscopic scale magnetization $\boldsymbol{M}$, which will be referred to throughout this section. The dynamics at the atomic levels involves interactions between spins, electrons, and phonons, with energy being transferred during these interactions, causing relaxation. The relaxation emerges as a damping torque which brings the precessional motion towards the applied magnetic field, seeking to align the magnetic moment with $\boldsymbol{H}$. In

1935, Landau and Lifshitz formulated the precessional dynamics [68], and in 1955, T. L. Gilbert reformulated their equation [69] expressing the sum of all relaxational processes through a single damping constant as the intrinsic property of the magnetic material—the so-called Gilbert damping, alpha. Since then, the Landau–Lifshitz–Gilbert (LLG) equation has been used to describe the magnetization dynamics:

$$\frac{\partial \boldsymbol{M}}{\partial t} = -\gamma \boldsymbol{M} \times \boldsymbol{H}_{\text{eff}} - \frac{\gamma \alpha}{M} \boldsymbol{M} \times (\boldsymbol{M} \times \boldsymbol{H}_{\text{eff}}), \tag{1.4}$$

In Eq. 1.4, $\boldsymbol{H}_{\text{eff}}$ accounts for the effective magnetic field, including demagnetization, the Zeeman effect, the anisotropic field, and the exchange field.

Solving the differential equation Eq. 1.3 (i.e. the zero damping version of Eq.1.4) in the frequency domain results in a steady state precession of the magnetization around the effective magnetic field when all field components other than the external applied magnetic field are omitted. It thus results in the precession frequency as expressed by the Larmor frequency, $\gamma/2\pi H_{\text{ext}}$. In reality, this is rarely the case, as other field components play major roles, introducing other terms in the Larmor frequency for an applied field $\vec{\boldsymbol{H}}$ at arbitrary angle, θ_H, as follows:

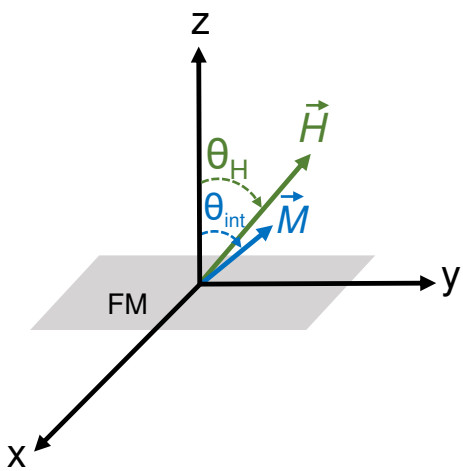

Figure 1.1: Representation of the magnetization vector $\vec{\boldsymbol{M}}$ in an applied magnetic field $\vec{\boldsymbol{H}}$ with the associated angles with respect to the film surface normal (z-axis)

$$\begin{aligned} f &= \frac{\mu_0 \gamma}{2\pi} \sqrt{H_1 H_2}, \\ H_1 &= H \cos(\theta_H - \theta_{int}) - 4\pi M_{\text{eff}} \sin^2 2\theta_{int}, \\ H_2 &= H \cos(\theta_H - \theta_{int}) + 4\pi M_{\text{eff}} \cos 2\theta_{int} + \frac{2K_2}{\text{s}} \sin^2 2\theta_{int}, \end{aligned} \tag{1.5}$$

where $\vec{\boldsymbol{M}}_{\text{eff}}$ is the effective magnetization field, defined as

$$M_{\text{eff}} = 4\pi M_{\text{s}} - \frac{2K_1}{M_{\text{s}}} - \frac{4K_2}{M_{\text{s}}}\cos^2\theta_{int}, \tag{1.6}$$

where K_1 and K_2 are the first and second order effective uniaxial anisotropies. $\vec{\boldsymbol{H}}$ and $\vec{\boldsymbol{M}}$ are the applied magnetic field and magnetization vector of the FM, with their corresponding angles θ_H and θ_{int}, respectively (Fig. 1.1). At the resonance conditions for the in-plane ($\theta_H = 90$) and out-of-plane ($\theta_H = 0$) applied fields, Eq. 1.5 will reduce to Eq. 1.7 for f_{IP} and f_{OOP}.

$$\begin{aligned} f_{\text{IP}} &= \frac{\mu_0\gamma}{2\pi}\sqrt{H_{\text{res}}\big(H_{\text{res}} + 4\pi M_{\text{s}} - \frac{2K_1}{M_{\text{s}}} - \frac{4K_2}{M_{\text{s}}}\big)}, \\ f_{\text{OOP}} &= \frac{\mu_0\gamma}{2\pi}\big(H_{\text{res}} - 4\pi M_{\text{s}} + \frac{2K_1}{M_{\text{s}}}\big). \end{aligned} \tag{1.7}$$

For an in-plane magnetized film, for example of NiFe, the anisotropy constants K_1 and K_2 are very small and can be neglected. However, as we will see in the following chapters, the anisotropy constants can be sufficiently large (in our case, as a result of perpendicular magnetic anisotropy) to partially cancel out the demagnetization field, even resulting in an out-of-plane magnetized magnetic layer.

After 40 years of use, another term was added to the LLG equation to account for spin transfer torque (STT), paving the way to the development of current driven spintronics. Slonczewski introduced the STT term in 1996 in a paper [24] entitled "Current-driven excitation of magnetic multilayers". He reformulated the LLG equation as Eq. 1.8, which is now known as the Landau–Lifshitz–Gilbert–Slonczewski (LLGS) equation.

$$\frac{\partial \boldsymbol{M}}{\partial t} = -\gamma \boldsymbol{M} \times \boldsymbol{H}_{\text{eff}} - \frac{\gamma\alpha}{M}\boldsymbol{M} \times (\boldsymbol{M} \times \boldsymbol{H}_{\text{eff}}) + \tau \boldsymbol{M} \times (\boldsymbol{M} \times \boldsymbol{P}), \tag{1.8}$$

Slonczewski's term stands for a current-induced spin torque from the polarization vector $\boldsymbol{P}$ of the spin current and τ is the driving torque. The STT term can act as an additional damping term or counteract the Gilbert damping torque term (the second term in the LLGS equation)—that is, act as negative damping—and ultimately compensate for it, resulting in a steady-state precession of the magnetization, or even flipping the magnetization to the opposite direction along the easy axis. The SHE has attracted considerable attention as an emerging method of generating pure spin current in GMR and TMR multilayers, outperforming the conventional method of using spin polarized layers.

1.1.4 Perpendicular magnetic anisotropy

At equilibrium, the magnetization of most ferromagnetic materials resides in the film plane. This is due to the so-called demagnetization field, which arises whenever the magnetization has a component along the normal of the surface of a magnetic material. The demagnetizing field makes it energetically

favorably for the magnetization to lie in a direction that minimizes the surface integral of this component, which in the thin film geometry strongly favors the in-plane orientation. However, strong spin-orbit interaction can lead to certain types of magnetic structures having a very large interfacial internal magnetic field perpendicular to the film plane, which counteracts for the demagnetization field, and which under certain condition overcomes the demagnetization field, bringing the magnetization to lie perpendicular to the film plane. A very well-known family of such structures is the $(Co/Pt)_n$ and $(Co/Pd)_n$ multilayers [70–72] in which the magnetic anisotropy arises from strong spin-orbit interaction of heavy metal layer. Perpendicular magnetic anisotropy (PMA) has been observed in a variety of different structures with amorphous and crystalline oxides, and also in transition metals, such as Co [73] and Fe [74], and in alloys such as CoFe [75] and CoFeB [76]. None of these materials have heavy atoms, nor do they have very strong spin-orbit interaction, yet they show a strong PMA. Oxide-based PMA has shown remarkable anisotropy amplitudes, comparable to traditional $(Co/Pt)_n$ interfaces. In fact, x-ray absorption (XAS) and x-ray photoemission (XPS) analysis show that the anisotropy arises from the interface between the oxide layer and the ferromagnetic layer, where chemical bonds form between the oxygen ions of the oxide and the ions of neighboring transition metal [77]. Ab initio calculations have confirmed the experimental analysis, showing that there is hybridization between the oxygen *sp* orbitals and the dz^2 orbitals in the transition metal (Co or Fe), producing strong anisotropy [78]. Since it was first described, Oxide-based PMA has been observed at many different oxide interfaces, such as HfO [79], MgO [78], AlO_x [80], and TaO_x [81].

The discovery of PMA in CoFeB-based MTJs—the most promising candidates for the commercialization of STT-based magnetoresistive random access memory (MRAM)—represented a great leap towards drastically reducing the threshold current for switching the free layer in MTJ cells. The threshold current in in-plane magnetized layers is strongly affected by the demagnetization field, as the STT needs to overcome the demagnetization field to flip the magnetization direction. As PMA offers substantial compensation for the demagnetization field, switching is now possible using very low currents [82]. As will be discussed in Chapter 2, PMA plays a major role in designing a new type of SHNO that is compatible with the CMOS process and with the conventional materials used in the MRAM industry.

1.1.5 Spin Hall nano-oscillators

Once the spin transfer torque overcomes the damping in the ferromagnetic layer, the magnetization enters steady–state precession around the effective magnetic field, $\boldsymbol{H}_{\text{eff}}$. As discussed earlier, the SHE is one way of producing the spin current. We would expect to obtain sustainable precession of the magnetization if the ferromagnetic layer is at the vicinity of the heavy metal, where the spins that accumulate at the HM–FM interface will eventually diffuse to the ferromagnetic layer, exciting the magnetization dynamics. However, there are also interfacial losses such as HM transparency loss [84, 85] and spin

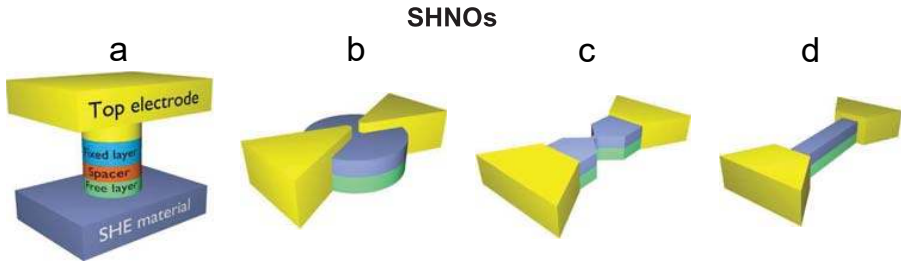

Figure 1.2: Different types of SHNO devices. (a) MTJ-SHNO, (b) nanogap SHNO, (c) nanoconstriction SHNO, and (d) nanowire SHNO
. Reproduced from [83]

memory loss [86, 87]. The former can reflect the spins back from the interface, while the latter accounts for spin information loss due to spin-flip scattering at the interface. Interfacial losses mean that the spin diffusion is not a lossless process. ξ_{SH} is the ratio for the spin current to the injected charge current, which accounts for losses in the spin diffusion. The value of ξ_{SH} will thus always be smaller than θ_{SH}.

In order to sustain precession in the FM layer (discussed in Section 1.1.3), the spin current density needs to reach a certain threshold. To satisfy the spin density requirement, STT-based spintronic devices are fabricated in nanoscale dimensions to provide a high charge current density, and consequently a high spin current density. The same current density requirement applied to SHE based oscillator. As the SHE provides spin current in the transverse direction, the SHE driven oscillators (also called SHNO) have been proposed in different nanoscale geometries. MTJ-SHNOs [64, 88], nanogap SHNOs [37, 89], nanoconstriction SHNOs (NC-SHNO) [38], and nanowire SHNOs [90] are examples of such SHE based devices schematically shown in Figure 1.2a–d [83]. In 2012, Demokritov et al. proposed the first magnetic oscillator driven by pure spin current [37]. Their device (shown schematically in Figure 1.2b) consisted of a NiFe/Pt bilayer in which two electrodes confine the current at the gap between two electrodes in order to deliver a high spin current density. The STT from the spin current maintains the magnetization precession, which leads to an oscillating device resistance through the AMR. The product of the resistance oscillation and the charge current then creates a microwave voltage across the electrodes. The excited mode in their device was a localized spin-wave mode, as localized dynamic objects free from radiation losses resulted in the lowest oscillation threshold current. Following the work of Demokritov et al., researchers at Cornell University published their results on a three-terminal MTJ (Figure 1.2a), in which the free layer at the bottom was excited by the adjacent Ta layer acting as an HM. This delivered higher power thanks to its high TMR [88], rather than the AMR used in the research of Demokritov et al.

Again in 2014, Demokritov's group pushed their idea further by proposing a nanoconstriction-based spin Hall nano-oscillator [38] as illustrated in Figure 1.2c, in which "the localized auto-oscillation mode arises due to

confinement in a potential well produced by the nonuniformity of the internal static magnetic field in a bow-tie-shaped magnetic nanoconstriction" [38]. The large volume of oscillating magnetization makes the oscillator less sensitive to thermal fluctuations. Their discovery opened the door to a new type of microwave spintronic device that is easily fabricated as single oscillators or as stacks of oscillators, and which can also be probed by optical means such as with a Brillouin light scattering microscope (BLS), as will be discussed later.

1.1.6 Frequency–amplitude non–linearity

The nature of a localized auto oscillation mode in SHNO keeps the frequency below FMR frequency where radiation losses are prevented since there is no propagation. The frequency behavior of the oscillator, however, can be described by a nonlinear equation as follows:

$$\omega(|c|^2) = \omega_0 + \mathcal{N}|c|^2, \tag{1.9}$$

Where ω_0 is the natural frequency of the SW, c is the complex dimensionless SW amplitude, and $\mathcal{N}$ is the coefficient of the nonlinear frequency shift for a normally magnetized film. Eq.1.9 clearly shows that the frequency of the SW mode depends on its amplitude. The $\mathcal{N}$ Can take both positive and negative values to shift the frequency of the oscillation up or down. For an isotropic magnet, the nonlinearity coefficient is zero. In SHNO, however, the in-plane shape anisotropy holds the magnetization vector in the film plane, keeping the $\mathcal{N}$ strongly dependent on the strength and orientation of the applied magnetic field. Also, introducing a strong PMA can counteract the shape anisotropy and cancel out the demagnetization field partially (or even completely), as well as bring the magnetization vector out of the film plane. The PMA then adds to the nonlinear coefficient a component with the opposite sign to the component associated with the shape anisotropy, leading to a global $\mathcal{N}$ calculated using the method proposed in [91, 92]. As we will see in the third chapter, Obtaining a substantial positive $\mathcal{N}$,*i.e,*, by tuning the PMA, can push the frequency of the localized SW to exceed the FMR frequency where spin–wave propagation is allowed.

1.1.7 Synchronization in SHNO

Synchronization in the classical context refers to the adjustment of the period of self-sustained periodic oscillators via weak interactions; that is, the adjustment in terms of phase–locking and unison of frequencies. In the seventeenth century, Christiaan Huygens [93, 94] discovered the phenomenon when he observed the synchronization of two pendulum clocks that he had built.

> "... It is quite worth noting that when we suspended two clocks so constructed from two hooks imbedded in the same wooden beam, the motions of each pendulum in opposite swings were so much in agreement that they never receded the least bit from each other, and the sound of each was always heard simultaneously.

> Further, if this agreement was disturbed by some interference, it reestablished itself in a short time. For a long time I was amazed at this unexpected result, but after a careful examination finally found that the cause of this is due to the motion of the beam, even though this is hardly perceptible.", he wrote.

The implications of his discovery were not fully understood until 1920, when B. Van der Pol developed a theory and experimentally demonstrated the synchronization of triode electronic generators [95]. Synchronization of self-sustained oscillators occurs on the basis of their phase ϕ, which is a value that parametrizes the motion along a stable limit cycle. The phase can be described as a time-varying variable $d\phi/dt = \omega_0$, where ω_0 is the natural frequency of the oscillation. Two interacting oscillators have the following generalized phase relationship:

$$\begin{aligned} \dot{\phi}_1 &= \omega_1 + f_1(\phi_2, \phi_1), \\ \dot{\phi}_2 &= \omega_2 + f_2(\phi_1, \phi_2). \end{aligned} \tag{1.10}$$

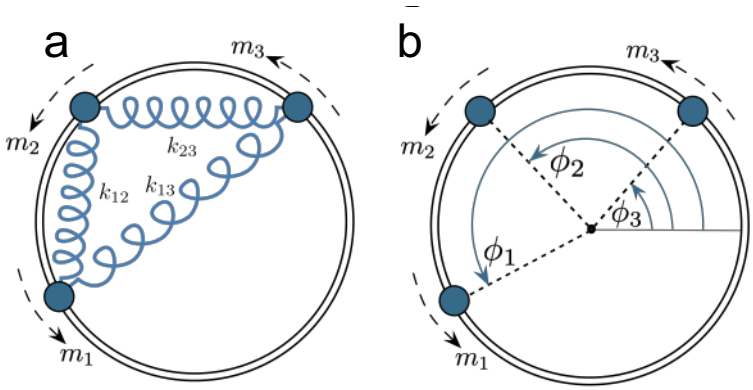

Figure 1.3: Mechanical analog model of coupled oscillators showing (a) non-symmetric couplings K_{ij}, $i, j = 1$, 2, and 3 .(b) phases ϕ_i for oscillators m_i, $i = 1$, 2, and 3.

Each oscillator is running on its own natural frequency ω_n. The influence of the second oscillator on the first is described by the function f_1, and influence of the first on the second by f_2. In general, these two functions can be different. In the injection locked case, one of the functions is zero. In the case of ideal mutual synchronization, Eqs. 1.10 can be modified by using symmetric influence functions:

$$\begin{aligned} \dot{\phi}_1 &= \omega_1 + f(\phi_2, \phi_1), \\ \dot{\phi}_2 &= \omega_2 + f(\phi_1, \phi_2). \end{aligned} \tag{1.11}$$

If we now assume that the interaction only depends on the phase difference

between the two oscillators, we have

$$\begin{aligned}\dot{\phi}_1 &= \omega_1 + f(\phi_2 - \phi_1),\\ \dot{\phi}_2 &= \omega_2 + f(\phi_1 - \phi_2).\end{aligned} \tag{1.12}$$

Considering only the f term, when we have $(\phi_2 - \phi_1)\text{mod} < \pi$, this means that the first oscillator is lagging behind the second oscillator on a circle as shown in Figure 1.3b. We would here like to speed up the first oscillator so that it catches up with the second oscillator. This can be done by requiring $f(\phi_2 - \phi_1) > 0$. This also means that the second oscillator slows down.

Likewise, if now the second oscillator falls behind the first, then $2\pi > (\phi_2 - \phi_1)\text{mod} > \pi$. The first oscillator should now be slowed down and the second should accelerate, giving $f(\phi_2 - \phi_1) < 0$. One particular coupling function f fulfilling these conditions is described by Eq. 1.13,

$$f(\phi_2 - \phi_1) = \frac{K}{2}\sin(\phi_2 - \phi_1), \tag{1.13}$$

where K is the coupling constant. Eq. 1.12 can be reformulated as follows:

$$\begin{aligned}\dot{\phi}_1 &= \omega_1 + \frac{K}{2}\sin(\phi_2 - \phi_1),\\ \dot{\phi}_2 &= \omega_2 + \frac{K}{2}\sin(\phi_1 - \phi_2).\end{aligned} \tag{1.14}$$

By subtracting the two equations in Eq. 1.14 and putting $x = \phi_2 - \phi_1$, Eq. 1.14 simplifies to

$$\dot{x} = \delta\omega - K\sin(x), \tag{1.15}$$

where $\delta\omega = \omega_2 - \omega_1$ is the difference in the natural frequencies. By solving Eq. 1.15 for the values of x, we obtain $\dot{x} = 0$, which means the two oscillators have the same time derivative of their phases. We need $K > K_c = \delta\omega$ for a stable answer for x as follows:

$$x = \phi_2 - \phi_1 = \alpha = \sin(\delta\omega/K). \tag{1.16}$$

The solution implies that:

- If the natural frequencies of both oscillators are the same, meaning that $\delta\omega = 0$, then the two oscillators will be synchronized with zero phase difference $\alpha = 0$.
- If $\delta\omega \neq 0$, the oscillators will be synchronized for coupling values $K > K_c$. In this case, they have a finite phase difference of $\sin(\delta\omega/K)$.

In 1975, Kuramoto proposed a model [96, 97] describing the synchronization of a large set of coupled oscillators. He took inspiration from chemical and biological oscillators which now have numerous applications in neuroscience. His model is built on the basis of a few assumptions including the existence of weak coupling, similarity of the oscillators, and sinusoidal dependence of the

phase difference between them. His model for the general case of N oscillators with all-to-all coupling can be written in a very similar way to Eq. 1.14:

$$\dot{\phi}_{\mathrm{n}} = \omega_{\mathrm{n}} + \frac{K}{N}\sum_{m}\sin(\phi_{\mathrm{m}} - \phi_{\mathrm{n}}). \tag{1.17}$$

The coupling between each pair of oscillators can be written as a matrix of K_{ij}, i and j are the i-th and j-th oscillators as shown in Figure 1.3a. Analyzing this case when we have a coupling matrix K_{ij} is difficult, and can result in very different and complex dynamics. However, we can summarize some of the general results:

- For any coupling strength, all the oscillators with the same natural frequencies will synchronize. This scenario implies a zero phase difference throughout the entire network.
- For modest differences in natural frequencies, and for reasonably large coupling, the network merges into a synchronized state exhibiting pairwise phase differences between oscillators within the network. The phase difference grows with the variance in natural frequencies.
- For weak coupling, and/or large variation in natural frequencies, the network of oscillators never synchronizes.
- For intermediate coupling, the oscillators might synchronize as small clusters, but fail to synchronize as an ensemble.

Synchronization of spin transfer torque and spin-orbit torque oscillators was proposed because they inherently suffer from large linewidth, resulting in high phase noise and low output power. Synchronization aims to increase the power and coherency of the output signal by suppressing phase noise. The first synchronization of spin transfer torque oscillators was reported back-to-back in two Nature papers in 2005 [34, 98], where propagating spin waves were responsible for the coupling between two nanocontact spin transfer torque oscillators (NC-STO) that shared the same free magnetic layer. It took researchers four years to increase the number of synchronized oscillators to four sub-GHz vortex oscillators [99] which synchronize via direct exchange interaction between neighboring vortices and antivortices. This slow progress lasted for another four years, until spin–wave synchronization of three high-frequency NC-STOs were reported in 2013 [36]. It was shown in the work of Sani et al. [36] that, as the number of synchronized oscillators increases, the output power and the signal coherency keep improving dramatically. In 2016, five NC-STOs were reported by Houshang et al. to synchronize when placed in such a way that their SW beams coincided [35]. Finally, in 2018, Tsunegi et al. showed an approach to scaling up to eight STOs coupled electrically via directional couplers, reaching 16 μW integrated power and a 54 kHz linewidth, operating at few hundred MHz. Although their research shows the importance of synchronization in improving the output signal, a bulky electronics setup is needed to realize it.

While progress has been slow for STT-based oscillators, the synchronization of SOT-based oscillators was achieved very rapidly. My colleagues reported the first mutually synchronized SHNOs in 2017, with up to nine oscillators lined up in a chain achieving synchronization [9]. SHNO chains offer significantly higher output power than single oscillators, while the signal coherency (linewidth) can be improved to reach sub-MHz values. They also are accessible to BLS microscopy in both the time and frequency domains, which allows us to study the high-frequency dynamics involved in synchronization. As we will see in Chapter 3, scaling up SHNO numbers in a two-dimensional arrays makes it possible to synchronize as many as 64 SHNOs and to obtain an order of magnitude improvement in the output signal quality factor (Q =170,000) compared to the earlier highest value reported (Q =18,000) in 2004 [100].

1.1.8 Memristors

A memristor is an element that relates charge q and flux ϕ, rather like how a resistor relates voltage V and current I, a capacitor relates voltage V and charge q, and an inductor relates current I and flux ϕ. Memristors were predicted in 1971 by Leon Chua [101], but were only realized in 2007 at Hewlett-Packard [102–104]. The device takes its name from both memory and resistors: its resistance depends on how much electric charge has passed, and in what direction, at the last operation. In other words, the device remembers its resistance when the electric power turned off. The Hewlett-Packard memristor is made of a few nanometer titanium dioxide layers sandwiched between two platinum contacts. The titanium dioxide layer has two parts, the first of which was doped with oxygen vacancies (TiO_x) and has low resistivity; the other part is a stoichiometric TiO_2 insulator (Fig. 1.4a). Upon applying voltage, the oxygen vacancies start to drift and expand the low resistivity zone (W), consequently reducing the thickness of the TiO_2 part. As the thickness of the TiO_2 part continues to drop, the field emission transport becomes dominant and the memristor is set in one of its low resistance states. If the voltage polarity is reversed, the oxygen vacancies are pushed back, and now the low resistivity TiO_x part is squeezed while the TiO_2 insulating layer extends its border, resetting the device to a high resistance state. Figure 1.4b shows the current–voltage (I–V) profile of a typical memristor, in which the low resistance state is defined by the current compliance (CC) of the voltage source.

If a device is to be a memristor, the I–V curve must be pinched at the origin of the I–V plot, which means that the memristor does not hold any energy when no power is supplied. Many different types of memristors have been proposed on the basis of different materials and technologies. For instance, redox-based memristors [105] include metal–ion and oxygen–ion devices [106]. The former operates on the basis of the migration of metal ions, which make a conductive path that can be reversibly formed into a conductive–nonconductive path. The latter category works on the basis of oxygen vacancies expanding or suppressing the low resistivity region, depending on the voltage polarity. Other types of memristors include electronic ones based on electron trapping [107, 108] and Mott insulators [109, 110]. Memristor types are not limited to these

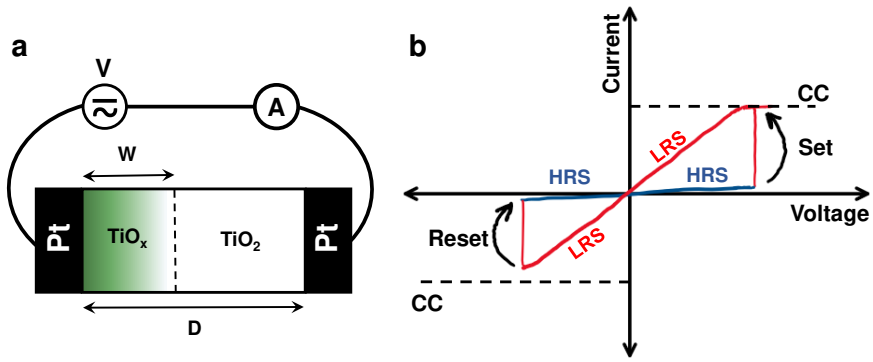

Figure 1.4: The first memristor proposed by HP [102, 104](a) Device schematic; (b) the I–V curve of a typical memristor.

categories. There are also spin transfer torque (STT) [111, 112] and phase change memristors [113, 114], which may be promising candidates for highly scalable and integrated memory cells and bioinspired computing.

1.2 Methods

1.2.1 SHNO fabrication

Fabrication of SHNOs has been described in previous works published by our group [115, 116]. However, in this thesis, a substantial modification will be introduced to improve the fidelity of the samples and their performance. In particular, it becomes essential to have identical oscillators to build long chains of mutually synchronized SHNOs and, even more importantly, for mutually synchronized two-dimensional SHNO arrays. We also demonstrate an entirely CMOS-compatible process and devices. We have adapted our choice of material and processing conditions to be suitable for high resistivity silicon substrates and have fabricated a number of different types of SHNOs. In this section, we explain the common processes used for all types. When we introduce the devices and the result pertaining to them in later chapters, more detailed fabrication processes will be provided.

1.2.2 Choice of substrate and thin film deposition

Selecting an appropriate substrate is a significant factor for the future application of SHNOs, as these devices should operate at rather high charge current densities. The high current density generates a significant amount of heat in nanoscale regions, which the substrate then needs to dissipate. Also, if SHNOs are become commercially viable, CMOS compatibility will be needed to provide on-chip readout circuitry. As CMOS technology is more mature and prefers silicon as its standard substrate, we have pushed our fabrication process toward entirely silicon-based processes. Silicon ($< 1\ 0\ 0 >$)

substrates, grown by float-zone techniques and possessing resistivities as high as 10,000 Ω.cm, are used as the starting substrates. Silicon also offers a very high thermal conductivity of 150 $Wm^{-1}k^{-1}$, giving it six times greater thermal conductivity than sapphire (25 $Wm^{-1}k^{-1}$) and 150 times greater than silicon oxide (1 $Wm^{-1}k^{-1}$), which are substrates typically used in prior spintronics reports [115, 116].

In order to deposit the multilayers used as starting stacks, an AJA Orion-8 ultrahigh vacuum sputtering system with 1×10^{-8} mTorr base pressure was used. The system accommodates seven guns in confocal configuration, and each gun can be used as both an RF and DC sputtering source. The AJA II-300 also enables us to co–sputter two materials at the time through the individual RF and DC sources. All layers were sputtered at 3 mTorr Ar pressure. The sputtering system can perform in-situ annealing at up to 800 °C and at a controllable rate. This option was used to induce PMA in CoFeB-based oscillators [55]. The deposition rate for each material was determined by using a quartz crystal thickness monitor (QCM), and the value obtained was confirmed using a Woollam M2000 ellipsometer for the elements and a Dektak profilometer for the alloys.

1.2.3 Optical lithography

In order to accurately allocate the SHNOs over the substrate, which is already covered with the multilayer stack, it is important to have some alignment markers to serve as references. The electron beam lithography (EBL) machine uses these alignment markers to coordinate the writing process. Since the EBL detection mechanism is based on secondary electrons when the electron beam hits the substance, it is important to use markers made of materials that give high contrast upon detection. Materials with rather low atomic numbers (Z) tend to show low contrast when they are scanned by the electron beam. It is thus necessary to define the markers with materials with higher Z numbers, and to make them thicker to increase the number of secondary electrons scattered from the markers. Tantalum (Ta) was chosen on account of its high atomic number ($Z = 73$) and excellent adhesion to many substrates. The Ta markers were defined by a lift-off process in which a double layer of 100 nm lift-off resist (LOR 1A) and 1.3 μm S1813 positive resist were spun coated on the substrate, followed by writing the marker patterns using a Heidelberg Instruments DWL 2000 laser writer. During the development process, the LOR layer dissolves much more rapidly than the S1813, resulting in an overdeveloped layer beneath the S1813. A 100 nm thick layer of Ta was then deposited by the sputtering machine while the S1813 layer shadowed the underdeveloped LOR regions, leaving no Ta deposited in those regions. After deposition, the sample was immersed in a warm photoresist remover kept at 50 °C to remove the S1813 and the LOR. The microscale regions shadowed by the S1813 allowed the remover to more easily attack the double layer at the edges of the pattern, leaving no polymer-based residuals behind.

1.2.4 Electron beam lithography

A state-of-the-art Raith EBPG 5200 EBL machine was used to define the nanostructures studied in this thesis. Compared to the conventional processes used for nanopatterning SHNOs—which employ polymer-based negative electron resists, such as maN-2400—in this thesis, we use hydrogen silsesquioxane (HSQ). HSQ is a class of inorganic compounds in which crosslinking is achieved through the exposure to an electron beam, resulting in a silicon dioxide structure that is insoluble in alkaline-based developers. The conversion of HSQ to silicon dioxide allows the electron resist to achieve very high contrast, thus enabling high resolutions of below 10 nm [117–120]. We developed two distinct processes to define the patterns with the HSQ. The first of these, the standard process, offers superior contrast to polymer-based election resists, while the second process has even higher contrast than the standard process; we refer to this as the high-contrast process. Both processes have their respective advantages and disadvantages.

1.2.4.1 The standard process

The standard process is used for all the fabrication processes throughout the thesis. It was designed to increase the layout fidelity of the fabricated SHNOs in the chains and arrays, where the nanoconstriction curvature and width play major roles in defining the natural frequency of the oscillator. As discussed in Section 1.1.7 on synchronization, having similar natural frequencies helps the oscillators synchronize with a smaller phase difference. The major drawback of polymer–based electron resists, such as maN-2400, is the excessive redeposition of the etched material on the resist sidewall during the etching process, and the difficulty of removing the plasma-exposed resist after the etching process. This sidewall redeposition, along with the excessive heat introduced by the plasma etching to the surface of the resist, causes fence-like structures left behind around the constriction region. These structures affect the magnetization dynamics and disturb the system, especially when we are aiming for larger arrays and chains. Figure 1.5 shows an AFM scan of the surface topology of an SHNO device in which the 100 nm maN-2400 resist used as the masking layer was removed after ion beam etching (IBE). The fence-like structures surrounding the SHNO have been determined to have a maximum height of 22 nm, while the bi-layer stack (Pt/NiFe) is only 11 nm thick, meaning that an extra 11 nm of redeposited materials have been left as the fence. In order to address these issues, we moved toward using HSQ as the standard electron resist in our processes. The 2% HSQ was spin-coated at 3000 rpm on the substrate containing the multilayer stack and the Ta markers, in order to leave a 37 nm uniform HSQ layer. Note that it is crucial for the HSQ to have excellent adhesion to the substrate, especially for lithography on noble metals such as Au, Pt, and Pd. In all these cases, we applied a waterborne adhesion promoter agent called SurrPass 4000 to facilitate lithography with HSQ. SurrPass 4000 can be spin-coated at 5000 rpm for 60 s. The adhesion can also be promoted by immersing the sample in SurrPass 4000 for 30 seconds and then rinsing it in DI water. After spin-coating, the sample was loaded

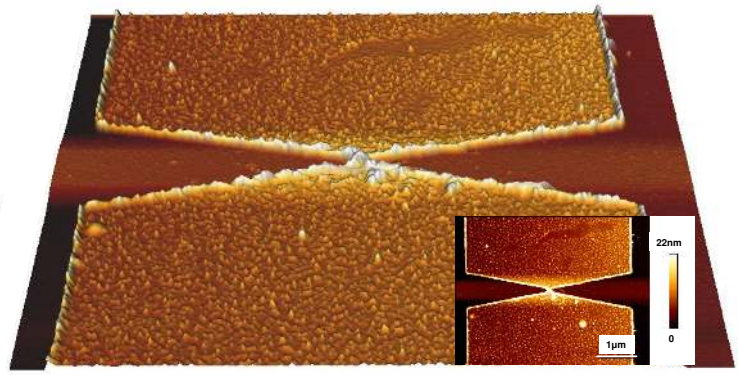

Figure 1.5: AFM microscopy of the surface of a SHNO fabricated SHNO using maN-2400 electron resist. The inset shows a height map of the structure where the bright regions correspond to the fence-like structures around the SHNO

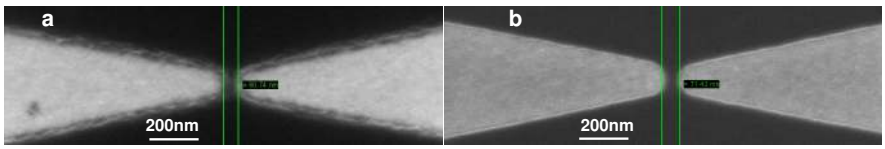

Figure 1.6: Electron-beam lithography of an 80 nm wide SHNO for (a) maN-2400 and (b) HSQ (standard process) electron resists.

into a Raith EBPG 5200 EBL machine at 100 kV. The exposure dose was chosen to be 2000 μC/cm^2, and the beam current was set to 2 nA. After exposure, the sample was immersed in MF CD-26 developer for 60 seconds. The exposure dose for HSQ is dramatically higher than for maN-2400, as there is no prebaking, and the crosslinking process is done entirely by electron beam.

The SEM images of EBL on maN-2400 (50 nm) and HSQ (37 nm) for 80 nm SHNOs are shown in Figure 1.6a and b, respectively. It is clear that the HSQ outperforms its polymer-based counterpart in terms of pattern fidelity and resolution. The superior performance offered by the HSQ becomes even more important when we are aiming for longer oscillator chains and arrays. Figure 1.7 shows SEM images of two chains of SHNOs: the oscillators for HSQ (Fig. 1.7b), are identical and the nanoconstriction curvatures are very smooth, compared to the same chain fabricated with maN-2400 (Fig. 1.7a). The standard process for HSQ can easily achieve sub-20 nm resolution for individual features. Figure 1.8 depicts a 20-nm SHNO obtained using the standard process on HSQ.

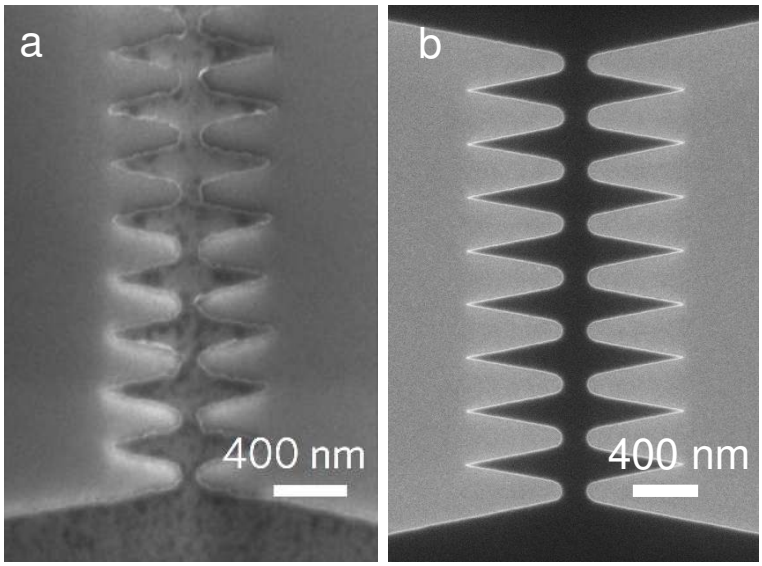

Figure 1.7: Electron-beam lithography for a chain of SHNOs. (a) maN-2400 and (b) HSQ (standard process) electron resists.

1.2.4.2 High-contrast process

The standard process for HSQ becomes challenging when the layout includes dense patterns with small pitches. Additionally, when the HSQ is used as the hard mask to etch rather thick layers (of more than 20 nm), the relatively high etch rate of HSQ in the IBE machine makes it not an ideal candidate for masking. It is thus important to have a sufficiently thick layer of HSQ while maintaining the high contrast and high resolution. The high-contrast process [121] uses 1 $wt\%$ NaOH and 4 $wt\%$ NaCl as a salty developer. Compared to other developers that have been proposed for the high-contrast process, such as 25 $wt\%$ TMAH, the salty developer is much safer to use in the cleanroom. It is also more compatible with the fabrication process, as it does not attack silicon, aluminum oxide, or aluminum.

Using the HSQ standard process, we obtained two-dimensional SHNO arrays with a reasonable resolution and pattern fidelity. Moreover, we developed the high-contrast process to further improve larger arrays with more SHNOs. Additionally, as we plan to extend our arrays to embed MTJs on top of the SHNOs, we will need high pattern fidelity and a thick HSQ mask to define the SHNOs and MTJ pillars on the thick MTJ-SHNO stacks. For the high–contrast process, it is crucial to have excellent adhesion of the HSQ to the substrate, as the salty developer used in this process is harsher than the standard process and can lift the whole crosslinked resist off if adhesion is poor. To address this, we could deposit a very thin layer of Ti (2 nm) or Cu (2 nm), to which the HSQ adheres very well when spin-coat over these layers. The 4% HSQ was spin-coated on the substrate at 1700 rpm, leaving a 90 nm uniform HSQ layer.

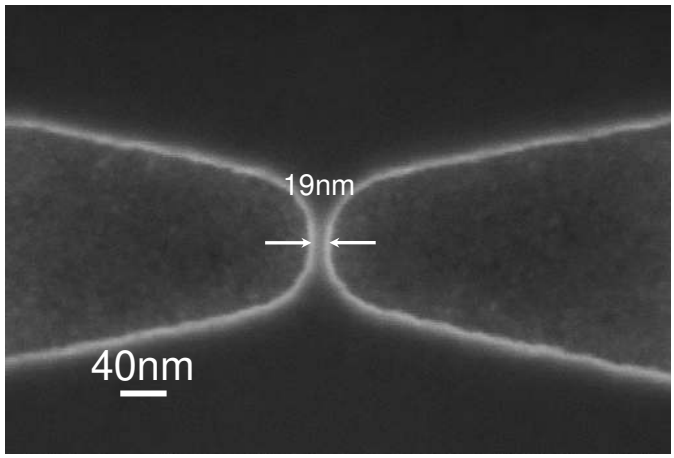

Figure 1.8: Electron-beam lithography for sub-20 nm SHNOs using the HSQ standard process.

The optimal electron-beam dose turned out to be 8000 μC/cm^2, which is four times higher than in the standard process. The thickness of the HSQ in the high-contrast process is the reason we need a higher dose than in the standard process to crosslink a substantial amount of the HSQ layer. In addition, since the salty developer is quite aggressive, the HSQ needs to be very strongly crosslinked to withstand it, and thus a higher dose is needed. The sample was developed in 1 $wt\%$ NaOH and 4 $wt\%$ NaCl developer for 60 seconds, before being immersed in DI water for five minutes and blow-drying with nitrogen. The immersion step is crucial to ensure there are no residual NaCl crystals are left on the sample. Figure 1.9 shows SEM images of 4×4 arrays of 50 nm wide SHNOs with a center-to-center distance of 50 nm. The high-contrast process can deliver decent pattern fidelity with a thick layer of HSQ (Fig. 1.9a), while the standard process achieves a reasonable process window only for thin HSQ layers (Fig. 1.9b).

1.2.5 Ion beam etching

After using HSQ to define the desired pattern, the sample is loaded into a dry etch Oxford Ionfab 300 Plus IBE machine equipped with an automatic load lock. The sample holder has a continuous rotation function that can be tilted for directional etching at oblique angles. We use an electron ammeter to ensure that the ion beam space charge is neutral. The tool is equipped with a Second Ion Mass Spectrometer (SIMS) used for endpoint detection, which is useful for stopping the etching process when a given layer is reached during etching. By adjusting the beam current, the etch rate can be set. Setting the beam voltage then defines the momentum being transferred to the layer during the etching process: the higher the beam voltage, the deeper the secondary ions

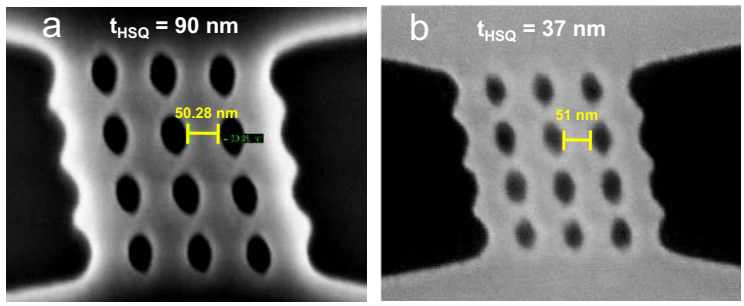

Figure 1.9: Comparison of the HSQ high-contrast process (a) with the standard process (b) in producing a 4×4 array of 50 nm wide SHNOs with a center-to-center distance of 50 nm.

come from. In practice, setting a very high beam voltage can result in damage to the layers underneath the target layer. In all IBE processes employed in this thesis, we used an incident angle of 30° with the sample in continuous rotation. The beam voltage was set to 500 V, the acceleration voltage to 300 V, and the beam current was kept at 10 mA. Though the setting we used for our samples is rather harsh, it does not introduce significant damage to the underneath layers, as we want to stop the etching process at the substrate. However, the etching conditions will have to substantially change when we eventually redesign the process for incorporating MTJs in the future.

1.2.6 Defining the measurement contacts

Defining the electrical contacts to conduct high-frequency measurements requires the definition of coplanar waveguides (CPW). The device under study and the fabrication materials determine the appropriate process for opening a via through the leftover HSQ mask. If other oxides are also present (such as MgO and AlO_x in W/CoFeB/MgO/SiO_2(AlO_x) devices), then a via through both HSQ and oxides is needed. In that case, we define the CPW pattern through the same process we used to define the alignment markers in Section 1.2.3 with LOR and S1813. The bilayer resist has openings to the HSQ at the ends of the SHNO mesa, where the metallic layers are buried under HSQ and possibly other oxides. For NiFe/Pt SHNOs, a very short exposure to buffered HF (BOE) 10:1 suffices to remove the HSQ at the openings, while the rest of the sample is protected by bilayer resist. In the case of W/CoFeB/MgO/SiO_2(AlO_x), where the BOE solution does not attack the MgO layer at a predictable rate, we used the IBE machine to remove both the HSQ and the other oxide layers. We obtained the etch rate for all materials in our stacks using SIMS during IBE to define the SHNOs. After opening the vias to provide access to the metallic layers, the sample was loaded into the sputtering machine to deposit a thick layer of Cu (700 nm)/Pt (20 nm) bilayer.

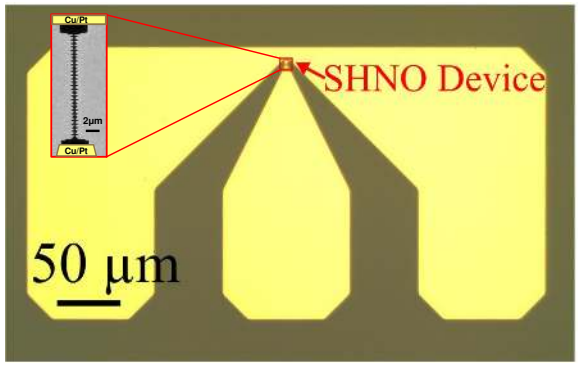

Figure 1.10: Optical microscope image of the fabricated CPW defining electric contacts on an SHNO. The inset shows an example of 51 SHNOs fabricated in a chain.

The Pt layer protects the Cu from oxidation. The bilayer resist was then lifted off by immersing the sample in the warm resist remover. The bilayer resist and sputtered materials came off the sample easily after about an hour of immersion. The sample was then immersed in a sequence of isopropanol (IPA) and DI water to ensure there were no residuals left on the sample. Finally, the sample was blow-dried in nitrogen. Figure 1.10 shows an optical microscope image of a CPW fabricated on top of an SHNO. The SHNO device being tested may have different geometries. As an example, a chain of 51 SHNOs is shown in the inset to Figure 1.10.

1.2.7 Characterization techniques

There are numerous characterization techniques used in this thesis, all of which were performed at room temperature. This section briefly introduces the techniques used.

1.2.7.1 AMR measurement

The first characterization of the fabricated SHNO devices to provide an estimate of the AMR ratio, one of the factors determining the level of the output power delivered by the sample. As discussed in Section 1.1.1, AMR is a change in the material's resistance caused by the relative orientation between the magnetic moment and the current passing through the material. To measure AMR, a low DC current of 100 μA is passed through the fabricated device. A constant in-plane magnetic field of 0.1 T is applied to the sample using a projection magnet while the angle of the applied field was swept from 0 to 360°. The strength of the magnetic field is kept at a constant high value to ensure that the FM magnetization is saturated in the direction of the applied field. A plot of the device resistance versus angle of the applied field then yields the value of the AMR, as explained in Section 1.1.1.

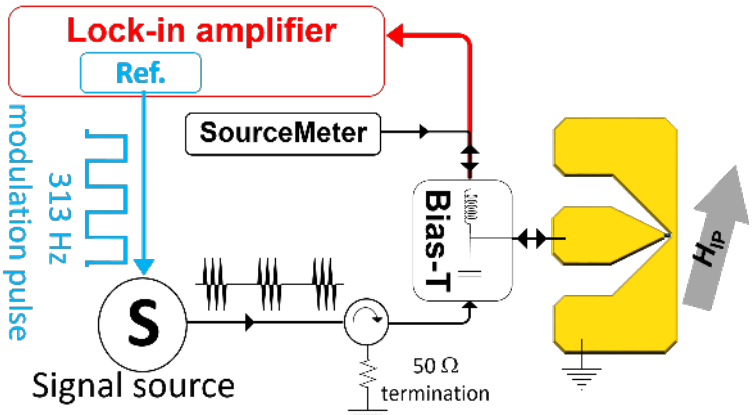

Figure 1.11: ST-FMR measurement setup schematic [123] for in-plane magnetized sample.

1.2.7.2 ST-FMR measurement

The spin transfer torque ferromagnetic resonance measurement technique (ST-FMR) [122] is an easy approach for studying the magnetodynamic properties at the micro- and nanoscale, where the use of conventional FMR spectroscopy is not possible. The ST-FMR technique does not require any external RF field, as the injected RF signal produces the spin-orbit torque needed to excite the ferromagnetic resonance in the magnetic layer. The magnetization oscillations cause a high-frequency change in the resistance by means of AMR. In the ST-FMR measurement, the current I_{RF} is chopped with a low-frequency signal and sent to the sample. The high-frequency change in the resistance results in an oscillating voltage which, if mixed with the injected I_{RF}, drops a DC voltage component when the frequency of injected signal I_{RF} approaches the ferromagnetic resonance of the magnetic layer at a given magnetic field. Although the mixed voltage is very small in amplitude (μV range), the use of a lock-in amplifier chopping the injected signal allows the background signal and noise to be suppressed further, allowing the mixed voltage to be detected. A schematic of the ST-FMR measurement setup is shown in Fig. 1.11. Note that an RF circulator is used to prevent the RF signal reflecting from the sample to reach the RF source.

The ST-FMR data is then fitted with the Kittel equation Eq. 1.7 to yield important parameters, such as the Gilbert damping coefficient, θ_{SH}, the effective magnetization $\mathbf{M}_{\mathrm{eff}}$, and the anisotropy. Knowledge of the operating frequency range and the magnitude of magnetic field and current required for the sample to operate is the starting point in designing a magnetic oscillator. Throughout this thesis, the ST-FMR technique has been used to characterize all the different magnetic material stacks.

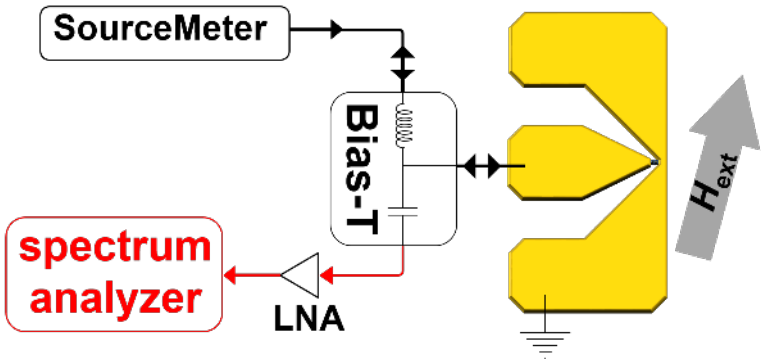

Figure 1.12: Schematic of AO measurement setup. [123]

1.2.7.3 Microwave measurement

Measuring the auto-oscillation (AO) of an oscillator is one of the most important characterizations in determining the behavior of SHNOs. In this measurement, a DC current is passed along the device while an external magnetic field is applied at certain OOP and IP angles. The applied current generates a spin current in the HM. As it diffuses into the FM, the spin current exerts a negative damping torque on the FM magnetization, eventually overcoming the intrinsic damping torque, leading to a sustainable precession of the FM magnetization. The precession gives rise to an oscillating resistance based on AMR. The oscillating resistance multiplied by the applied DC current produces an oscillating voltage with a frequency in the GHz range. The DC and microwave components coming out of the sample are sent to a bias-tee, where the DC component is blocked and the microwave components are sent to a low noise amplifier (LNA), before being captured by a Rhode & Schwarz FSV-40 spectrum analyzer. Values of resolution bandwidth (RBW) and video bandwidth (VBW) are chosen on the basis of signal coherency (linewidth). The entire measured frequency range includes the background noise level, which needs to be removed from the captured spectrum prior to analysis. The background noise level is not uniform over the entire scanned frequency range. For this reason, the spectra at very low DC current are captured in the first measurement trace in order to determine the noise floor for the entire frequency range. This noise floor is later subtracted from the captured PSD spectra to produce clean AO spectra. The clean AO spectra are presented in dB over noise (or simply dB). The measured PSDs are fitted to symmetric Lorentzian functions to determine the peak frequency, signal coherency (linewidth), and peak power. Our measurement setup also measures the sample DC voltage while it is being studied. We used a Keithley 6220 precision current source in combination with a 2182A nanovoltmeter to conduct the DC measurements.

1.2.7.4 Microfocused Brillouin light scattering spectroscopy

Brillouin light scattering spectroscopy [124] is a direct way of mapping and characterizing spin-waves at much smaller dimensions than is possible with conventional FMR techniques. In μ-BLS, the spatial resolution is technically limited by the laser spot size, which is defined by the diffraction limit of the laser wavelength and the objective used in the setup. The interaction between photons and magnons—the respective quanta of light and spin waves—plays a major role in the mechanism of BLS. The incoming photons can generate or annihilate magnons in an inelastic scattering process. The scattering process causes the photons to gain or lose energy, depending on the type of interaction with magnons, which is translated as a shift in the frequency and wavelength in the scattered light sent to an interferometer. The interferometer is the heart of the μ-BLS: it has a very high-frequency resolution to distinguish between many SW modes. Using a six-pass Tandem Fabry-Perot 1 interferometer (JRS Scientific Instruments), intensities can be captured in the frequency domain while a single photon counter enumerates the outcoming photons. The μ-BLS signal thus obtained is proportional to the square of the dynamic amplitude at the corresponding frequency.

Our μ-BLS uses 532 nm light from a solid-state laser. A dark field objective with a numerical aperture of $NA = 0.75$ focuses the laser beam, resulting in a laser spot size of about 300 nm. Using a three–dimensional scanning stage with 10 nm precision, the spatially resolved maps of the magnetization dynamics can be profiled. The μ-BLS is also equipped with a spectrum analyzer for capturing the AO of the device under study at the same time as the optical measurement is being carried out.

2

CMOS-compatible spin Hall nano-oscillators

STNOs and SHNOs are the building blocks of future spintronic microwave devices for a wide range of applications. Microwave signal generators [9, 35, 55, 83, 88], microwave detectors [125], memories [126–128], and bioinspired computing [39, 129–131] are some examples of such applications, many of which require CMOS compatibility for integration. Power consumption, microwave output power, and signal coherency are some of the other criteria needed to compete with established semiconductor microwave technologies. It will also be important to develop processes that are compatible with existing technologies in the spintronic industry; for instance, the MRAM industry uses an established technology based on MTJs made of CoFeB and MgO, which can be integrated at the back end of line (BEOL) in CMOS technology. Any new device compatible with MRAM materials and their processing will attract more attention from foundries—just as MRAM itself has ensured process compatibility with CMOS technology in order to facilitate its integration. In this chapter, we introduce some approaches aimed at enhancing the abilities of SHNOs. We first demonstrate the CMOS compatibility of an SHNO based on NiFe/Pt bilayers. A new type of SHNO based on W/CoFeB/MgO, compatible with MRAM technology, is then introduced. Perpendicular magnetic anisotropy (PMA) [15, 55, 132] plays a major role in achieving low power consumption and broad frequency tunability in W/CoFeB/MgO SHNOs. We will also show how tuning the PMA can lead to a propagating SW source through the introduction of high positive nonlinearity at low spin current density [15].

2.1 Hafnium dusting of NiFe/Pt SHNOs

Manuscript I : Gilbert damping (α) is a parameter of ferromagnetic materials. However, a ferromagnetic material's damping can be severely affected when it is placed adjacent to other layers, in particular in multilayer stacks. In the case of SOT devices, there is a damping enhancement phenomenon attributable to spin-flip scattering through spin-orbit coupling by phonons or defects in the ferromagnetic layer [133, 134]. The properties and quality of the interfaces to

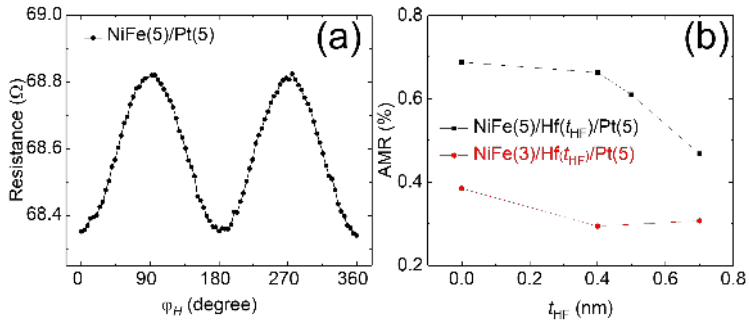

Figure 2.1: Hf thickness-dependency of AMR. (a) Magnetoresistance for the reference stack NiFe(5)/Pt(5), (b) extracted AMR versus Hf thickness ratio. Reproduced from Ref. [138] with the permission of AIP Publishing.

other materials also play a major role in enhancing the damping. The effective spin-mixing conductance, $G_{\text{eff}}^{\uparrow\downarrow}$, is a parameter capturing both interface and bulk phenomena. It affects the damping constant as follows: [135]

$$\alpha = \alpha_0 \; + \; \frac{\gamma\hbar^2}{2e^2 M_s t_{\text{FM}}} G_{\text{eff}}^{\uparrow\downarrow}, \tag{2.1}$$

where α_0 is the intrinsic damping of the FM single layer. $G_{\text{eff}}^{\uparrow\downarrow}$ includes terms that counteract each other [87]: the first represents the spin current being pumped from the FM to the FM/NM interface (I_s^{pump}) while the magnetization in the FM is precessing, causing spins to accumulate in NM; these can then flow back (I_s^{back} from the NM to the FM, counteracting the spins that are pumped by the FM. When the NM has a smaller spin accumulation, as in Pt, due to its strong spin sinking properties, there is a smaller backflow of spins to counteract the spin pumping term, leading to an inevitable increase in the damping constant. The both mentioned terms are rather intrinsic properties of the FM and HM. The other term, the spin memory loss (σ), determining the probability for an electron's spin to change its direction as it traverses the interface, originates from interfacial spin-orbit coupling (ISOC) contributing to the damping enhancement [136, 137].

We introduced an ultrathin layer of Hf to the interface between Pt and NiFe in order to modify the interface to suppress the $G_{\text{eff}}^{\uparrow\downarrow}$, thus reducing the damping constant—an important factor in defining the threshold current and the switching in SHNO and MTJ memory cells, respectively.

2.1.1 Fabrication of NiFe/Hf/Pt ST-FMR samples

We fabricated two series of trilayer stacks, NiFe(3)/Hf(t_{Hf})/Pt(5) and NiFe(5)/Hf(t_{Hf})/Pt(5) (the numbers in parentheses indicate the thickness in nm), with the Hf thickness having the following values: $t_{\text{Hf}} = 0$, 0.4, 0.5, and 0.7 nm. The stacks were patterned into 6 μm wide and 100 μm long bar-shaped structures using the optical lithography fabrication process described in Section 1.2.1.

2.1.2 Characterization of the NiFe/Hf/Pt samples

We first characterized how Hf dusting impacts the AMR of the bilayers. The AMR measurements were performed by sweeping the in-plane field angle from $\varphi_H = 0°$ to 360°, while the strength of the magnetic field was kept at $\mu_0 H_{\mathrm{IP}} = 0.1$ T. Figure 2.1a shows the AMR for a NiFe(5)/Pt(5) bilayer, as a reference sample, while Figure 2.1b displays how AMR depends on Hf thickness; its dependence is relatively weak, only showing a substantial decrease for the thickest Hf layer on the thicker NiFe film. Any detrimental effect of Hf dusting on the AMR is hence limited.

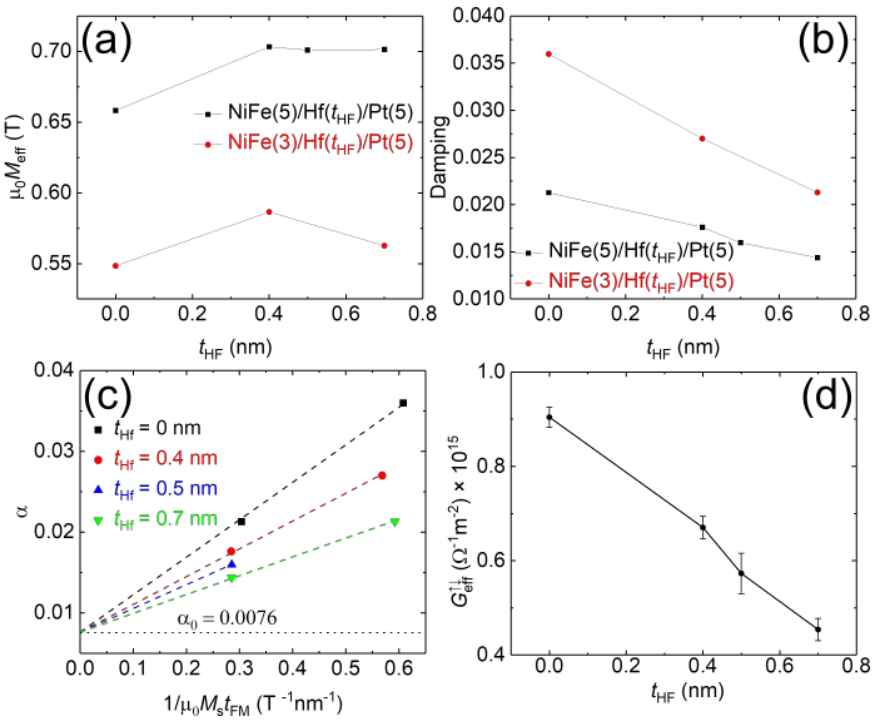

Figure 2.2: Extracted parameters from ST-FMR characterization for (a) M_{eff}, (b) t_{Hf}, (c) damping as a function of $1/\mu_0 M_s t_{\mathrm{Hf}}$, and (d) effective spin mixing conductance. Reproduced from Ref. [138] with the permission of AIP Publishing.

The ST-FMR characterization (explained in Section 1.2.7.2) at zero device current provides us with the magnetodynamical properties of the trilayers as a function of Hf dusting. Hf is found to have a moderate beneficial impact on the effective magnetization (Figure 2.2a) and a significant monotonic beneficial impact on the damping (Figure 2.2b).Extracted values for $1/\mu_0 M_s t_{\mathrm{FM}}$ are shown (dots) in Figure 2.2c, where M_s is replaced with M_{eff}, as the magnetocrystalline anisotropy in NiFe is very small. By substituting the values of $1/\mu_0 M_s t_{\mathrm{Hf}}$ into Eq. 2.1, $G_{\mathrm{eff}}^{\uparrow\downarrow}$ as a function of Hf thickness can be calculated,

as shown in Figure 2.2d. As it can be seen, the value for the effective spin-mixing conductance drops by about 50% at $t_{\mathrm{Hf}} = 0.7$ nm, a trend reflected in the damping values plotted in Figure 2.2b. Therefore, we interpret this reduction in $G_{\mathrm{eff}}^{\uparrow\downarrow}$ as a direct reduction of the interface spin loss at the NiFe/Pt.

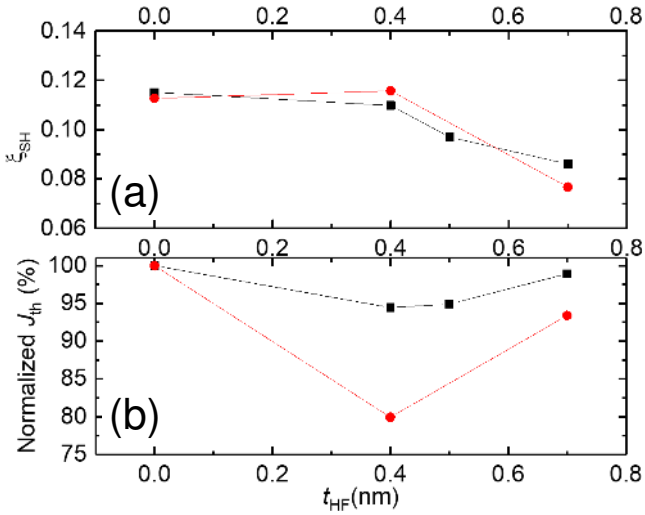

Figure 2.3: (a) Spin Hall efficiency versus Hf thickness; (b) the normalized calculated threshold current density. Reproduced from Ref. [138] with the permission of AIP Publishing.

We then conducted ST-FMR measurements at different device currents to obtain the spin Hall efficiency, ξ_{SH}, of the stacks. As can be seen in Figure 2.3a, ξ_{SH} is unaffected at moderate Hf thickness but then drops as the Hf thickness is further increased. The loss of interface transparency to transmit the generated spin current (arising from spin memory loss) may be the reason for the decay in spin Hall efficiency [139, 140].

There are thus two parameters that affect the AO threshold current while at the same time counteracting each other. The damping coefficient decreases with the increase in Hf thickness, while the spin Hall efficiency remains almost flat up to $t_{\mathrm{Hf}} = 0.4$ nm, from which point it falls. These two counteracting parameters lead us to the compromise for threshold current density shown in Figure 2.3b. Here the minimum occurs at $t_{\mathrm{Hf}} = 0.4$, suggesting the optimum thickness for Hf to reach about 20% reduction in the threshold current.

As a consequence of this study, we always dust the NiFe/Pt interface with 0.4–0.5 nm Hf for optimum magnetodynamical properties when using NiFe/Pt in our devices. However, depending on which device property one wants to optimize, the optimum Hf thickness might be slightly different. As we will see later in this thesis, mutual synchronization in SHNO chains and arrays depends on the extent of the auto-oscillating region, which may grow larger if the damping is further reduced. These details related to Hf dusting have not yet been explored but could inspire further studies.

2.2 CoFeB-based spin Hall nano-oscillators

Manuscript II : If spintronic microwave devices are to follow the progress of commercial MRAM and STT-MRAM [141], it is important to use materials and develop processes that are compatible with both MRAM and CMOS. Developing a microwave oscillator driven by the spin Hall effect thus requires high efficiency in the pure spin current generation, while making use of materials already used in the MRAM industry, such as MgO, CoFeB, W, and Ta. It has been shown in numerous studies that W [62, 63, 142], and Ta [64, 143] exhibit much higher spin Hall angles than Pt [9, 10, 37, 38]. In addition, Si substrates offer excellent thermal conductivity, helping to dissipate the heat generated by the rather high resistivity of NM layers such as β-phase W and Ta. This is in stark contrast to the poor thermal conductivity of thick SiO_2 often used as the substrate for spintronic microwave devices to minimize microwave losses. The high-temperature treatment for introducing PMA into CoFeB also does not lead to silicide formation at the substrate/NM interface when W [144] is used. W increases the thermal budget to 700, as long as the other parameters do not limit the processing. The increased thermal budget does not hold for other nonmagnetic metallic layer materials, such as Pt [145], Pd [146], or CuBi, which either tend to form silicides or interdiffuse when exposed to high temperature. The silicide layer is typically of low resistivity, and thus shunts the current from the NM layer, causing a severe degradation in spin current generation. In this section, we therefore propose SHNOs based on β-W/$Co_{20}Fe_{60}B_{20}$/MgO stacks fabricated on high resistivity (to keep microwave losses low) Si substrates. Our material stacks show a record high spin Hall angle of θ_{SH}=-0.53, the fabricated devices show a record low AO threshold current, and the frequency can be tuned over a very wide range.

The SHNO stack consists of a W(5)/$Co_{20}Fe_{60}B_{20}$(2)/MgO(2) multilayer deposited on high-resistivity silicon using our AJA Orion-8 magnetron sputtering system. DC and RF sputtering were used to deposit the metallic and insulating layers, respectively. After deposition, the stack was annealed at 300 °C for an hour, and then left to cool down to room temperature. The annealing process is required to crystallize the CoFeB to have good AMR and to realize high PMA (if desired). Crystallization begins at the interface between MgO and CoFeB while W acts as a Boron getter to facilitate this process [147]. In order to prevent the MgO layer from reacting with moisture, which would cause the layer to crack, 4 nm thick SiO_2 was sputtered on top of the stack. Table 2.1 shows the the deposition rates for different materials

Target	Power (W)	Pressure (mTorr)	Rate(Å/s)
W	10 (dc)	3	0.09
$Co_{20}Fe_{60}B_{20}$	20 (dc)	3	0.09
MgO	90 (RF)	3	0.04
SiO_2	150 (RF)	3	0.1

Table 2.1: Deposition conditions for a W/CoFeB/MgO/SiO_2 stack.

used in the stack. The layer resistivities were measured using a four-point probe technique, giving values of 200 $\mu\Omega$·cm and 90 $\mu\Omega$·cm for W and CoFeB, respectively. The high resistivity of W confirms the predominant formation of the β-phase, which has been reported in the literature to have a high spin Hall angle [63, 147]. The stacks then went through the SHNO fabrication process discussed in Section 1.2.

2.2.1 Characterization of the W/CoFeB/MgO devices

The first step in characterizing the stack was to determine the saturation magnetization (M_s), which is an important factor in determining the magnetic field required to observe AO. Using an alternating gradient field magnetometer (AGM), we obtained a value of $\mu_0 M_s$ = 1.17 T. Figure 2.4 shows the AGM measurement for the in-plane (Fig. 2.4a) and out-of-plane (OOP) (Fig. 2.4b) applied magnetic fields, respectively. While it is clear from both figures that the magnetization lies in the film plane (in-plane magnetized), Figure 2.4b indicates that the magnetic field required to align the magnetization in the OOP configuration is substantially reduced, as the film already saturates at about 0.7 T (and not at $\mu_0 M_s$ = 1.17 T) in the OOP direction. This reduction is a clear indication that PMA (K_1 in Eq. 1.7) of about 0.5 T has been induced in the CoFeB layer, counteracting the demagnetization field due to the magnetization [132, 148].

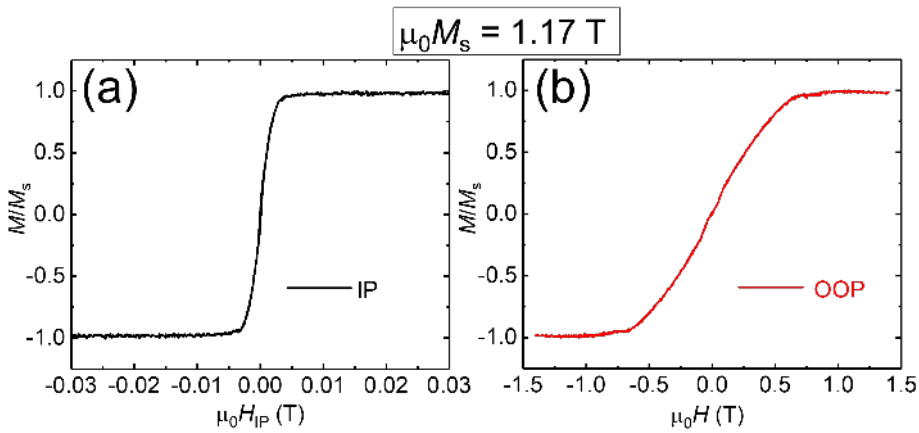

Figure 2.4: AGM characterization of a W/CoFeB/MgO stack for magnetic field applied (a) parallel to the plane of the film (IP) and (b) out of the plane (OOP) of the film.

We then conducted ST-FMR measurements (explained in section 1.2.7.2) on a 6 × 18 μm^2 bar, to obtain an effective magnetization of $\mu_0 M_{eff}$ = 0.71 T, a gyromagnetic ratio of $\gamma/2\pi$ = 30.9 GHz/T, a Gilbert damping of α = 1.36 × 10^{-2}, and a spin Hall angle of θ_{SH} = -0.53; we note that the extracted θ_{SH} is considerably higher than in the case of Pt (θ_{SH} = 0.06–0.2). It is again

interesting to compare $\mu_0 M_{\text{eff}} = 0.71$ T with the $\mu_0 M_S = 1.17$ T measured using alternating gradient magnetometry (AGM), which shows that a moderate PMA field of 0.46 T has been induced.

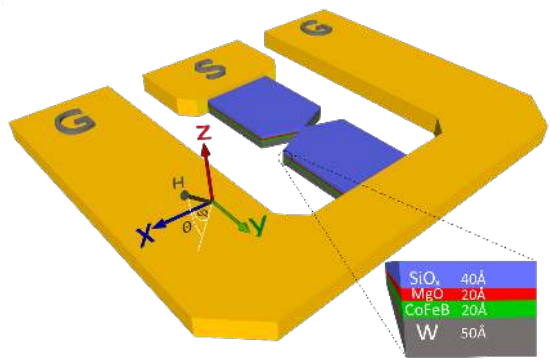

Figure 2.5: Three-dimensional schematic of the fabricated W/CoFeB/MgO-based SHNO; θ and ϕ denote the OOP and IP angles of applied magnetic field. Reproduced from Ref. [55] with the permission of AIP Publishing.

Figure 2.5 shows a three-dimensional schematic of the SHNO, including the CPW. The coordinate system shows the OOP (θ) and IP (ϕ) angles of the applied external magnetic field. The AMR of the device was measured to 0.34% (see inset of Figure 2.6d).

To investigate the AO, we performed microwave characterization as described in Section 1.2.7.3. We used an LNA amplifier with +43 dB gain to amplify the signal prior to capturing it with a Rohde Schwarz FSV 10–40 GHz spectrum analyzer. Figure 2.6 shows the power spectral density (PSD) of the SHNO as the applied DC current was swept from 0.3 mA to 0.9 mA for two OOP angles: 60° (Fig. 2.6a) and 75° (Fig. 2.6d). As explained in Ref. [149], the AO begins at one of the constriction edges, where the negative nonlinearity leads to a corresponding frequency red-shift with current; this is directly observed in Fig. 2.6a for currents below $\sim$ 0.5 mA. As the applied current increases, the AO mode leaves the edge, moves towards the constriction center, and expands throughout the constriction region; in this regime the nonlinearity changes sign to positive and, as a consequence, the frequency blue-shifts with current. However, the AO movement and expansion does not depend solely on the applied current. It is also affected by the OOP angle of the magnetic field, θ. Figure 2.6d shows a regime in which the AO mode has already detached from the constriction edges and moved toward the center constriction, even at low applied current; hence, the AO starts and continues in the positive nonlinearity regime. Figures 2.6(b,c) and (e,f) show the corresponding linewidth and integrated power extracted from Figures 2.6a and b, respectively. As the precessional volume increases with current, it increases the total energy of the

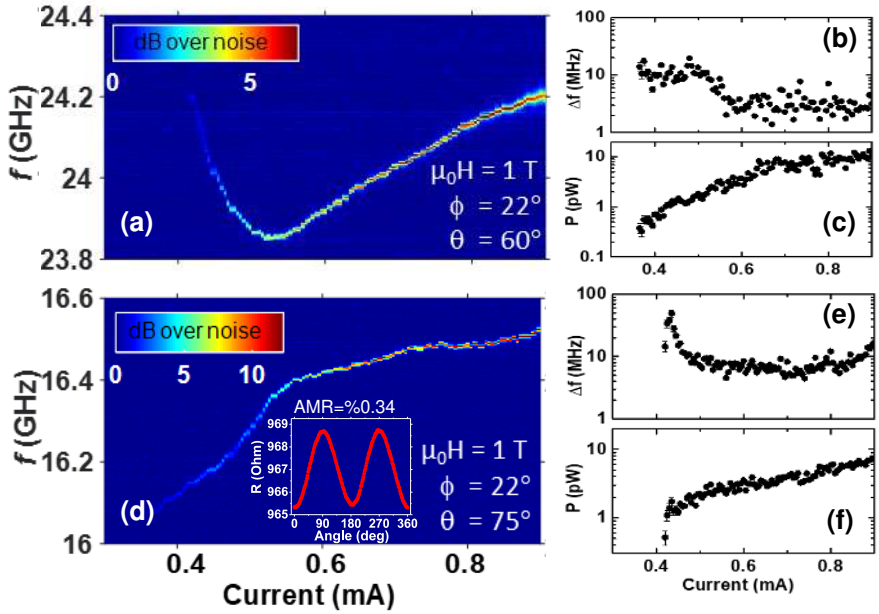

Figure 2.6: Microwave characterization of a W/CoFeB/MgO-based SHNO. (a, d) Spectral power density, (b, e) linewidth, and (c, f) integrated power, for $\theta = 60°$ and $\theta = 75°$. Reproduced from Ref. [55] with the permission of AIP Publishing.

AO mode. The noise is governed by the ratio of thermal to AO mode energy; therefore, higher AO mode energy suppresses the noise in the system giving rise to the signal-to-noise ratio (SNR). The linewidth is also improved with current as it is inversely proportional to the total energy of the AO.

In Figure 2.7 we investigate the frequency response of the SHNO vs. OOP angle of a $\mu_0 H = 1$ T applied field at a constant current of $I_{\mathrm{dc}} = 0.9$ mA; the operating frequency can be tuned over a very wide frequency range from 12 to 28 GHz. The inset to Figure 2.7 similarly shows how the AO frequency depends linearly on the applied field strength, here at a fixed OOP angle of $\theta = 80°$ and a current of I_{dc}=0.75 mA. Interestingly, the auto-oscillation is sustainable for magnetic field values much less than M_S, which is an obvious consequence of the PMA compensating for demagnetization field, *i.e.* helping the external magnetic field to bring the magnetization out of the film plane at a lower field value.

The key property of these CoFeB-based SHNOs, which affords them significant versatility for applications, is the emergence of strong PMA at the FM/oxide interface. The PMA can be tuned by adjusting the growth parameters of the stack, including CoFeB thickness, annealing temperature, and the type of seed layer. As we will see in later chapters, the PMA can also be controlled by external means using voltages applied to the MgO layer. As

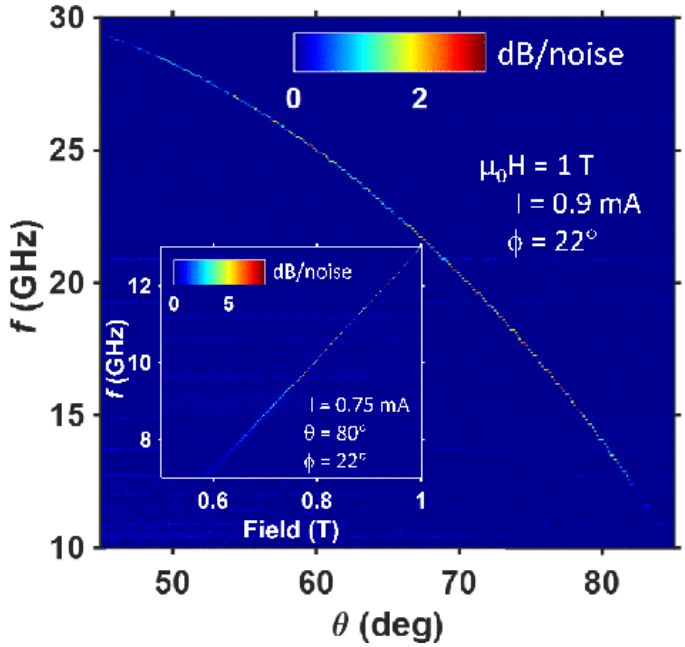

Figure 2.7: AO response to the OOP angle, θ, and the applied magnetic field sweep (inset). Reproduced from Ref. [55] with the permission of AIP Publishing.

we saw above, the PMA can partially cancel out the demagnetization field to reduce the required field and applied current for the SHNO operation. The next section describes how tuning the PMA can further enhance the performance of the SHNOs and open up an entirely new approach to not only excite edge modes and modes tied to the excitation region, but truly propagating spin waves.

2.3 Propagating spin waves in CoFeB–based spin Hall nano-oscillators

Manuscript III : Everything we have discussed so far has concerned SHNOs auto-oscillating on localized SW modes whose frequencies lie below the FMR, *i.e.* where no propagation outside the excitation region is allowed [149]. Mode localization is generally explained by the limited positive nonlinearity to push the frequency above the FMR frequency. However, in SHNOs based on magnetic films with large PMA, a large positive nonlinearity can push the AO to frequencies well above the FMR frequency, leading to the propagation of SWs with a finite wave vector [15]. Propagating spin waves can be used in applications such as magnonic waveguides [150–154] and wave-based computing [155, 156]. The wavelength of propagating SWs at microwave

frequencies can be much smaller than the structure size—unlike in optical systems where the orders of magnitude larger wavelength makes scaling difficult. Also, as we discussed in the previous section, PMA can result in an oscillator that operates at lower AO threshold current and required applied field.

In this section, we introduce an SHNO based on a W/CoFeB/MgO trilayer where a change in the thickness of the CoFeB from 2 nm to 1.4 nm results in a significant increase in the PMA field. The proposed device operates at yet lower threshold currents, while the enhanced PMA boosts the nonlinearity coefficient to push the auto-oscillation frequency above the FMR frequency, where SW propagation is both allowed and experimentally observed.

2.3.1 Device characterization

The starting stack was a trilayer of W(5)/$Co_{20}Fe_{60}B_{20}$(1.4)/MgO(2). We used the same fabrication process as described in Section 1.2.1. The most obvious difference is the CoFeB thickness of 1.4 nm. Conducting ST-FMR on a 6 × 18 μm bar revealed $\mu_0 M_{\text{eff}} = 0.31$ T, a gyromagnetic ratio $\gamma/2\pi = 29.9$ GHz/T, and a Gilbert damping constant $\alpha = 0.023$. The value for the saturation magnetization was obtained by AGM and estimated to $\mu_0 M_S = 0.93$ T. Compared to the same stack with 2 nm CoFeB, the PMA has been substantially enhanced, so an even lower AO threshold current is expected. The much higher PMA should also have a much more significant impact on the nonlinear magnetodynamics.

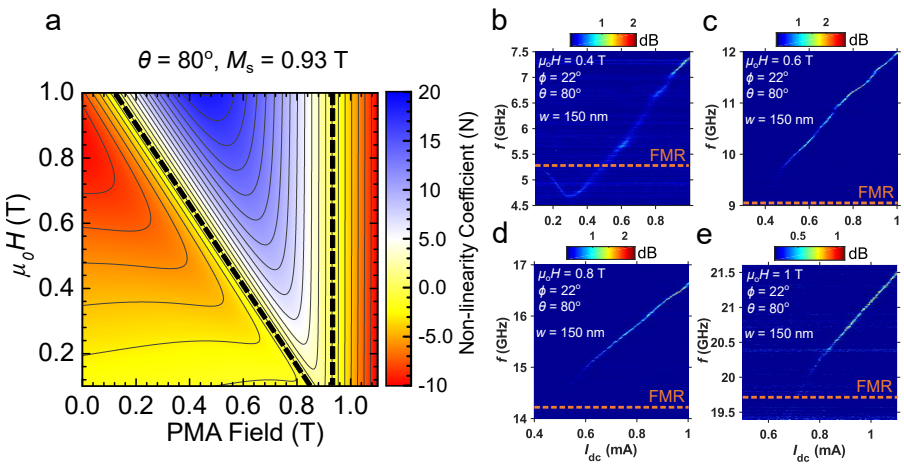

Figure 2.8: (a) Nonlinearity as a function of PMA and external magnetic field. AO PSD plot for (b) $\mu_0 H = 0.4$ T, (c) $\mu_0 H = 0.6$ T, (d) $\mu_0 H = 0.8$ T, and (e) $\mu_0 H = 1$ T. Reproduced from [15].

Figure 2.8b–e shows the AO measurement for a 150-nm-wide SHNO operating at different applied field strengths. In Figure 2.8b, the applied field of 0.4 T and the PMA are not sufficient to push the initial AO frequency above the calculated FMR frequency (red dotted line). However, once the

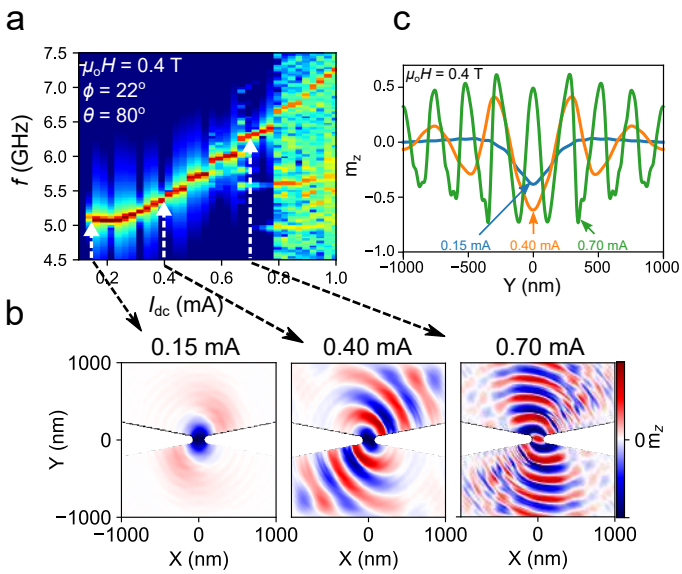

Figure 2.9: (a) Micromagnetic simulation of PSD for a 150 nm wide SHNO under the same condition as experimental PSD shown in Fig.2.8 b. Snapshot of instantaneous m_z at three different applied current in which the AO transitions from localized mode (at 0.15 mA) to propagating at higher current values (0.4 and 0.7 mA). The wave vector increases with current as it is also shown in (d) where a cut through Y–axis of (b) at three different currents. Reproduced from [15].

positive nonlinearity provided by the applied current (or more precisely, by the precession amplitude) kicks in, the AO frequency eventually manages to exceed the FMR frequency at about 0.5 mA. Figure 2.8A shows the calculated nonlinearity plotted for different PMA fields and external magnetic fields at an OOP angle of $\theta_{ex} = 80°$. At higher applied fields, in Figure 2.8c–e, the frequency of the linear SW mode of the system already lies above FMR, so the AO begins immediately above the FMR frequency as soon as the applied current reaches the auto-oscillation threshold.

The obtained experimental PSD shown in Figure 2.8b is reproduced by micromagnetic simulation considering the same condition as the experiment, e.g., the applied field, θ, ϕ, and current. The result are shown in Figure 2.9a. Figure 2.9b shows the snapshots of the m_z component of the precessing magnetization at three different current values. At low current, 0.15 mA, the AO mode clearly is localized and confined within the nano–constriction. For higher currents, i.e., 0.4 and 0.7 mA, the AO mode turns into propagating wave with the wave–verctor increasing with the current. The cut through Figure 2.9b along the Y-axis shows the m_z for three current values, 0.15, 0.4, and 0.7 mA.

The particular case of operation at 0.4 T allows for an interesting application where the current can be used to switch between localized and propagating SWs in the same devices. Ultimately, such SHNOs may deliver ultra–short SW

pulses and wave packets [157]. The propagating waves could also be useful in synchronizing chains and arrays of SHNOs by optimizing the damping constant to allow for long-range propagation.

2.4 Current modulation of spin Hall nano oscillator

Manuscript IV : Telecommunication systems require signal modulation in order to encode data for transmission. Most radio broadcast systems employ frequency modulation (FM) or amplitude modulation (AM). The modulation facilitates frequency division multiplexing (FDM), allowing multiple low-pass information signals to be transferred simultaneously on the same physical medium, by allocating separate passband channels (several carrier frequencies). SHNOs can offer amplitude and frequency modulation via their drive current. We have looked at SHNO modulation in different regimes and different nonlinearities. We then developed a model called nonlinear frequency and amplitude modulation (NFAM) to predict modulation performance and behavior.

The starting stack consisted of a 5 nm Pt and 5 nm Py ($Ni_{80}Fe_{20}$) bilayer, with a 5 nm SiO_2 protective layer. The stack went through the fabrication process described in Section 1.2.1. Figure 2.10a presents a schematic of the measurement setup in which a DC current was sent through a bias tee. An external RF signal at 80 MHz was added to the DC current using a microwave circulator (4–12 GHz). An SHNO with a 200 nm constriction is shown in the inset to Fig. 2.10b. The free-running frequency and output power, respectively, versus I_{dc} in the SHNO are shown in Figures 2.10b and c, respectively. The second derivative of the frequency with respect to the applied DC current is plotted in Figure 2.10d.

The NFAM model assumes that the instantaneous frequency and amplitude depend nonlinearly on the modulating signal $m(t) = I_m \sin(2\pi f_m t)$ as follows:

$$\begin{aligned} f_i(t) &= \sum_{h=0}^{v} k_h m^h(t), \\ A_c(t) &= \sum_{l=0}^{u} \lambda_l m^l(t), \end{aligned} \tag{2.2}$$

where I_m is the modulating current amplitude, f_m is the modulation frequency, k_h is the h^{th}-order frequency sensitivity coefficient, and k_0 is the unmodulated SHNO frequency. The λ_l specifies the l^{th}-order amplitude sensitivity coefficient. The coefficients k_h and λ_l are calculated by fitting polynomials to f vs. I_{dc} and P vs. I_{dc} of the free-running oscillator summarized in Table 2.2. The NFAM model predicts the output voltage amplitude spectrum

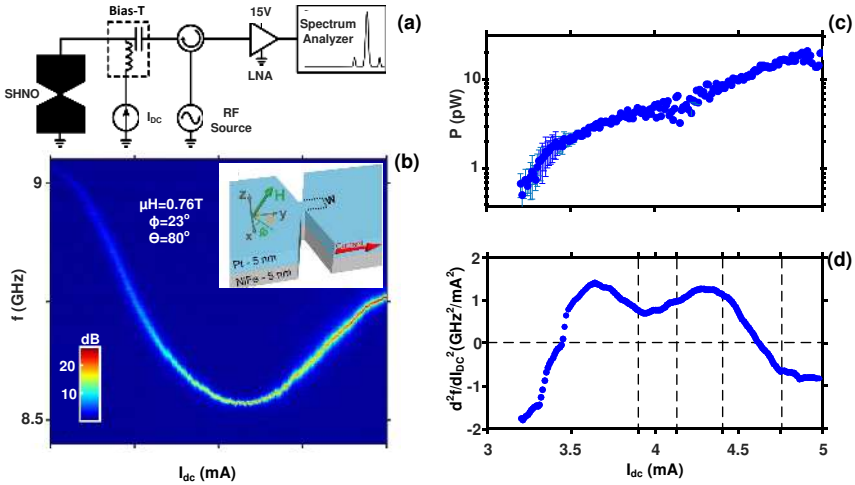

Figure 2.10: (a) Schematic of the measurement setup. (b) Color map of the power spectral density (dB over noise) vs. applied DC current of free-running SHNO in an out-of-plane field configuration, with φ=23° and θ=80°. The inset shows the schematic of the SHNO where φ and θ are shown in the coordination system. (c) Integrated power vs. current. (d) dI^2/dI^2 vs. current. The four operating points are marked by vertical dashed black lines. Reproduced from [17] with the permission of IEEE Publishing.

$S(f)$ as follows:

$$
\begin{aligned}
&S(f) = \\
&\frac{1}{4}\sum_{h=0}^{3}\gamma_h \sum_{n,m,p,q,r=-\infty}^{\infty} J_m(\beta_1)J_n(\beta_2)J_p(\beta_3)J_q(\beta_4)J_r(\beta_5) \\
&\quad\times\big\{\delta[f-f_c-(n+2m+3p+4q+5r+h)f_m] \\
&\quad+\delta[f-f_c-(n+2m+3p+4q+5r-h)f_m] \\
&\quad+\delta[f+f_c-(n+2m+3p+4q+5r+h)f_m] \\
&\quad+\delta[f+f_c-(n+2m+3p+4q+5r-h)f_m]\big\},
\end{aligned}
\tag{2.3}
$$

where $\beta_1 = k_1 I_m/f_m + 3k_3 I_m^3/4f_m$, $\beta_2 = k_2 I_m^2/4f_m + k_4 I_m^4/4f_m$, $\beta_3 = k_3 I_m^3/12f_m$, $\beta_4 = k_4 I_m^4/32f_m$, and $\beta_5 = k_5 I_m^5/80$ stand for the frequency indices of different orders, while $\gamma_0 = \lambda_0 + \lambda_2 I_m^2/2$, $\gamma_1 = \lambda_1 I_m + 3\lambda_3 I_m^3/4$, $\gamma_2 = \lambda_2 I_m^2/2$, and $\gamma_4 = \lambda_3 I_m^3/4$ are the amplitude modulation indices of different orders. The frequency also depends nonlinearly on the modulation current:

$$
f_c = k_0 + k_2 I_m^2 + 3k_4 I_m^4/8 + \ldots \tag{2.4}
$$

Knowing k_i and λ_i from the free-running behavior of the SHNO, the NFAM model can thus predict both f_c and the amplitudes of all sidebands located at

Table 2.2: Modulation sensitivity coefficients extracted from polynomials fitted to the free-running behavior of f vs. I and P vs. I. Reproduced from [17].

I (mA)	k_0(GHz)	$k_1(\frac{\text{GHz}}{\text{mA}})$	$k_2(\frac{\text{GHz}}{\text{mA}^2})$	$k_3(\frac{\text{GHz}}{\text{mA}^3})$	$k_4(\frac{\text{GHz}}{\text{mA}^4})$	$k_5(\frac{\text{GHz}}{\text{mA}^5})$	$\lambda_0(\text{pW}^{1/2})$	$\lambda_1(\frac{\text{pW}^{1/2}}{\text{mA}})$	$\lambda_2(\frac{\text{pW}^{1/2}}{\text{mA}^2})$	$\lambda_3(\frac{\text{pW}^{1/2}}{\text{mA}^3})$
3.9	8.5590	-0.2099	0.4737	-0.0007	0.2287	-0.0716	2.3281	0.9725	0.8116	3.9
4.13	8.5357	-0.02501	0.5789	0.2442	-0.3345	-0.9367	2.6545	1.6235	1.9751	2.6632
4.4	8.5847	0.3107	0.3276	-0.6333	-0.1591	0.6520	3.4212	3.5014	0.4954	-4.8189

$\pm sf_m$ relative to f_c. Here $s = n+2m+3p+4q+5r\pm h$ is an integer identifying the sideband order.

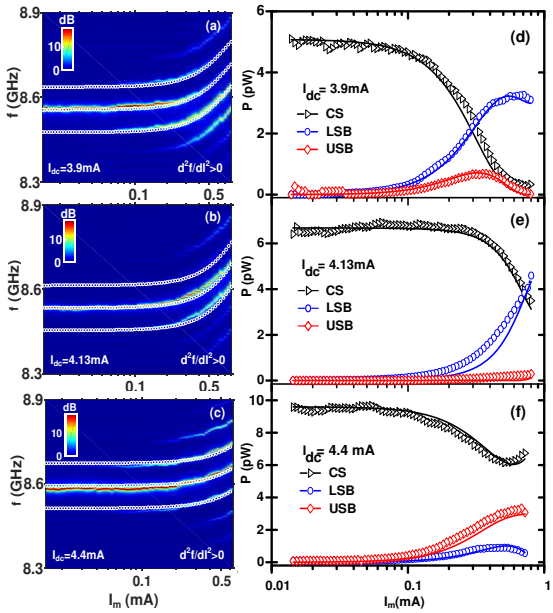

Figure 2.11: RF Modulation of the SHNO for three different DC operating points, $I_{\text{dc}} = 3.9$, 4.13 and 4.4 mA, corresponding to negative, zero, and positive nonlinearity regimes, respectively. (a)–(c) PSD plots showing the CS, LSB, and USB shifts and their dB over noise power, along with the frequency shift calculated by NFAM (white hollow circles). (d)–(f) Experimental integrated power with NFAM calculation of CS, first LSB, and USB, corresponding to (a)–(c). Reproduced from [17] with the permission of IEEE Publishing.

Figure 2.11a–c depicts the experimental values and NFAM calculation of frequency versus applied RF current (I_m) for an SHNO operating at three different applied DC currents, namely $I_{\text{dc}} = 3.9$, 4.13, and 4.4 mA, corresponding to negative, zero, and positive nonlinearity regimes, respectively. At all these operating points, d^2f/dI^2 is positive. The carrier and sideband frequency shifts are predicted analytically by the NFAM model (white hollow

circles) by obtaining the frequency indices of different the orders k_i (Table 2.2). Having obtained the values of λ_i (Table 2.2), NFAM can predict the integrated power of the carrier signal (CS), the first lower sideband (LSB), and the first upper sideband (USB), as shown in Figure 2.11d–f (solid lines). Clearly, the NFAM results are in excellent agreement with the experimental values of the integrated power upon modulation.

The NFAM model is thus a useful tool for predicting the modulation behavior of an SHNO given the free-running properties of the SHNO. Together with the ease of fabrication of nanoscale SHNOs, the NFAM model quantitatively describes information encoded in both frequency and amplitude, which can be used in the guidelines for designing the demodulator on the receiver side.

3

Two-dimensional spin Hall nano-oscillator arrays

Manuscript V : Nano-oscillators based on STT and/or SOT are promising candidates for nanoscale and CMOS-compatible microwave devices in future communications systems. Though there has been significant progress in developing new materials and designs to improve their output power and signal coherence (related to phase noise and linewidth), STNOs and SHNOs cannot yet compete with their conventional semiconductor microwave device counterparts. Synchronization of ensembles of STNOs was early on proposed to enhance both the output power and the signal coherence [158, 159]. However, progress towards realizing a large number of synchronized oscillators has been slow, due to the complex nature, and sometimes limited understanding, of their interactions. While simplified synchronization models capture their qualitative behavior, the large number of SW modes, the different types of interaction mechanisms, and the vast parameter space in terms of device layout, current, field magnitude, and both IP and OOP field angle, require computationally complex simulations to understand, replicate, and extend to larger arrays. Studies of mutual synchronization of STNOs and SHNOs is hence critically important for their potential future applications.

Inspired by the brain's operation, researchers have also attempted to use mutual synchronization to implement oscillatory networks that imitate rhythmic neuronal signals. The aim is to understand communication between phase-locked synchronized ensembles of excitatory neurons, making these artificial networks perform the information processing that our brain is capable of, in the form of particular cognitive tasks. For such tasks, our brain still outperforms any existing CMOS processor in terms of energy efficiency, speed, and fault tolerance.

Synchronization is also one of the most frequent phenomena in both nature and technology. Examples of synchronized networks include hippocampal and cortical neuronal activities [160, 161], fireflies [162], pacemaker cells in the heart [163], arrays of lasers and power generators [164], arrays of micromechanical oscillators [165], superconducting Josephson junction arrays [166, 167], and synchronization in spin transfer torque oscillators [8, 9, 35,

168]. However, implementing a large physical network that meets the technical requirements—such as room-temperature operation, scaling, integration, high speed, and low power consumption—has remained a challenge.

This chapter introduces the fabrication and characterization of up to 100 SHNOs arranged in two-dimensional (2D) arrays. We demonstrate microwave signal generation in all arrays, complete mutual synchronization in arrays with up to 64 oscillators, and partial synchronization in the arrays with 100 oscillators. We also demonstrate that mutual synchronization of such large oscillator ensembles dramatically improves the linewidth, with an order of magnitude better performance than any earlier literature values. Our results pave the way for large CMOS-compatible oscillatory networks, based on nanoscale SHNOs, which are further scalable in terms of both device size and array size, enabling them to meet the requirements mentioned above.

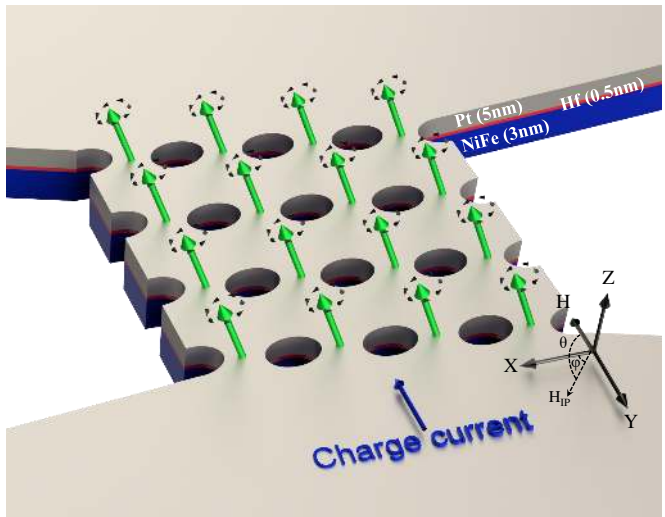

Figure 3.1: Schematic representation of a 4×4 SHNO array with $(w, p) = (120, 300)$. The schematic shows the direction of the applied magnetic field (H), in-plane component (H_{IP}) and the charge current direction. The black orbiting arrows indicate the precessing magnetization of each nanoconstriction. The Pt, Hf, and NiFe layers are colored gray, red, and blue and their thickness is shown in nm.

3.1 Fabrication of 2D SHNO arrays

As discussed in Chapter 2, introducing an ultrathin layer of Hf at the NiFe/Pt interface reduces the threshold current needed to excite AO in the ferromagnetic layer. We hence started with a trilayer of $Ni_{80}Fe_{20}$(3nm)/Hf(0.5nm)/Pt(5nm), deposited using magnetron sputtering. This was followed by the HSQ standard process, ion beam etching, and definition of the top contact, as described

in Chapter 1. We fabricated 24 square SHNO arrays with numbers of nanoconstrictions (N) ranging from 2×2 to 10×10 (*i.e.* from 4 to 100 nano-constrictions). The arrays are defined by the width of SHNOs, w, and their center to center distance (*i.e.*,pitch size), p.. Four pairs of w and p were chosen as follows: $(w, p) = (50, 100)$, $(80, 140)$, $(120, 200)$, and $(120, 300)$ with all values in nanometers. The different values of w and p were chosen to study the range and impact of the coupling strength. Figure 3.1 depicts the schematic of a 4×4 array of SHNOs in which the magnetization of each oscillator is illustrated by a green arrow precessing around the effective magnetic field H (the orbit of precession is shown by the black arrows). The OOP and IP angles, θ and ϕ, are defined in the coordinate system, while the blue arrow shows the direction of the charge current passing through the sample. The NiFe, Hf, and Pt layers are colored blue, red, and gray, respectively, while the numbers in parentheses show their thicknesses in nm.

Figure 3.2 shows SEM images of two-dimensional SHNO arrays for (w, p) = $(120, 200)$, accommodating 2×2 (4 SHNOs) to 10×10 (100 SHNOs).

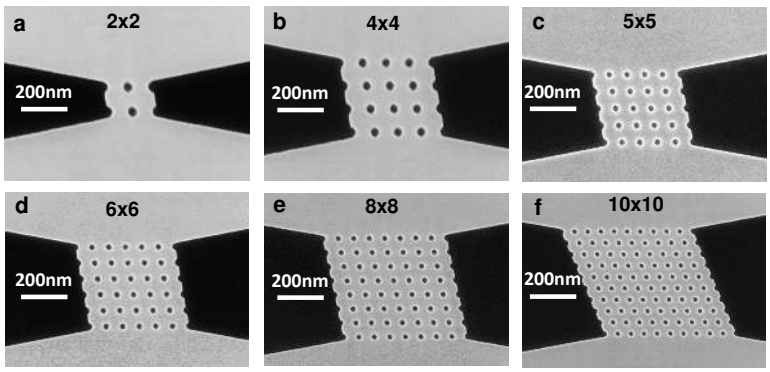

Figure 3.2: SEM images of two-dimensional SHNO arrays with (w, p) = $(120, 200)$ for different array sizes. (a) 2×2, (b) 4×4, (c) 5×5, (d) 6×6, (e) 8×8, and (f) 10×10 SHNOs.

3.2 Microwave measurements on 2D SHNO arrays

In order to measure the AO in 2D SHNO arrays, we carried out the microwave measurements described in Section 1.2.7.3. All measurements were performed with a magnetic field of 0.68 T, at an out-of-plane angle of 76° and an in-plane angle of 30°. Figure 3.3 represents the PSDs of the AO spectra for different number of constrictions (N) and different values of (w, p). Figure 3.3a–e demonstrate that all 2×2 arrays, regardless of width and separation (w, p), have sufficient coupling strength to bring all the oscillators into synchrony. As can be seen for the 2×2 arrays with (w, p)= $(50, 100)$ (Fig. 3.3a), the coupling is so

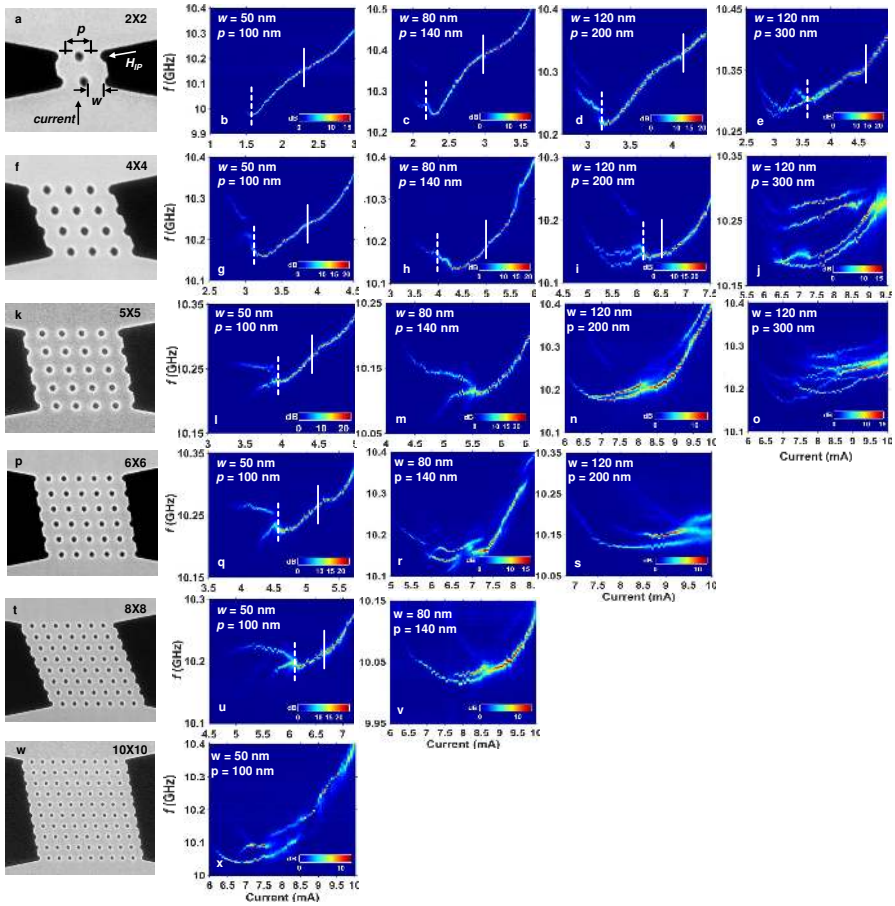

Figure 3.3: AO PSD measurements for SHNO arrays with $(w, p) = (50, 100)$, $(80, 140)$, $(120, 200)$, and $(120, 300)$ for different array size. (a–e) 2×2, (f–j) 4×4, (k–o) 5×5, (p–s) 6×6, (t–v) 8×8, and (w–x) 10×10 SHNOs. The leftmost column with the SEM images is only to indicate the array size (number of SHNOs in the arrays) corresponding to each row. The white dashed lines indicate the current values at which a robust mutually synchronized state is achieved.

strong that all oscillators essentially begin their AO in their synchronized state. At all larger separations, we can observe individual oscillators approaching the synchronized state; this is intuitively consistent with the decay in both dipolar and exchange coupling strength as we position the oscillators further away from each other. As the size of the arrays grows in terms of N, those arrays with larger pitch size (i.e., $p = 300$ nm) do not experience sufficiently strong coupling to bring the entire ensemble into a synchronized state; this is shown in Figure 3.3j, where the SHNOs in the 4×4 array fail to reach a common synchronized state. The 5×5 array fails to synchronize for both

$(w, p) = (120, 200)$ and $(120, 300)$, as Figure 3.3n and o illustrate, while the synchronization still holds for smaller values of (w, p). The PSDs (the colored bar shown in dB over noise) show a drastic increase in the output power once the oscillators are operating in unison and can be used as an additional indicator of complete mutual synchronization. Looking at the PSD plots reveals that only the arrays with the smallest $(w, p) = (50, 100)$ achieves global synchronization for the 6×6 and 8×8 SHNO arrays (Fig. 3.3u), indicating that the strongest coupling is indeed achieved for the smallest pitch. However, even this coupling strength is insufficient to synchronize the entire 10×10 array, as the PSD indicates a severe drop in output power of any observable peak (Fig. 3.3x).

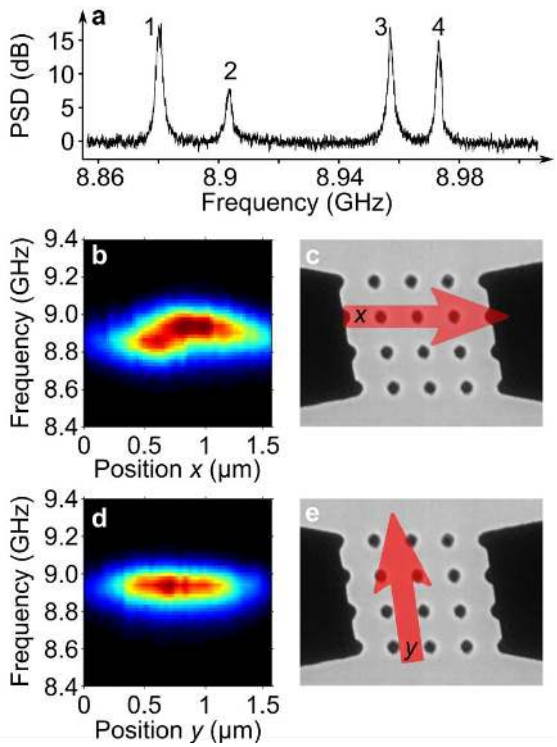

Figure 3.4: (a) PSD plot of a 4×4 array with $(w, p) = (120, 300)$ biased at fixed DC current. Four individual peaks are detected, corresponding to each synchronized chain. (b) BLS map of the line scan across the chains shown in (c). (d) BLS map of the line scan along the chains shown in (e). The frequency shows an obvious shift for the scan across the chains, while it remains constant for the scan along the chains.

As the AO mode tends to expand along the DC current direction [149], it is more likely that the coupling should be strongest within chains where both exchange coupling and dipolar coupling can contribute, and weaker between chains where only dipolar coupling should be important. Figure 3.4a shows the PSD spectrum of a 4×4 array with $(w, p) = (120, 300)$ operating at 7 mA

in a magnetic field of 0.68 T with an out-of-plane angle of 76° and an in-plane angle of 30°. Four distinct individual peaks can be observed; Intuitively, we would guess that the four peaks are associated with the mode expansions along the chains, so each peak represents one synchronized chain in our 4×4 array. We can test this idea using direct observation with a μ–BLS microscope. We therefore conducted μ–BLS line scans across and along the chains, as shown in the SEM images in Figure 3.4c and e, respectively. The corresponding BLS maps of frequency content vs. position for each scan direction are shown in Figure 3.4b, and d. It can be seen that for the scan along the chains, the BLS mode remains constant in frequency and does not change; for the scan across the chains, however, there is a clear red-shift in frequency for the chains at the corners.We can hence conclude that the coupling along the chains indeed dominates over the coupling between chains and that synchronization begins within the chains, followed by chain-to-chain synchronization. As the value of p grows, the arrays fail to synchronize when the number of SHNOs increases.

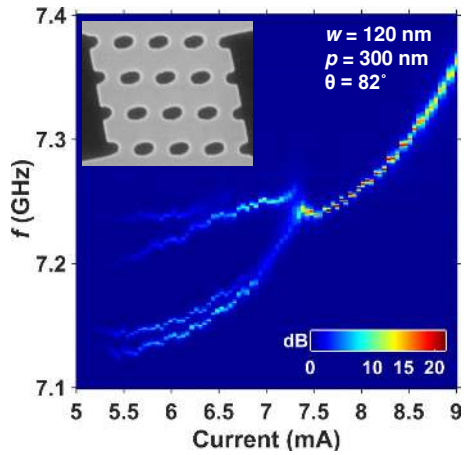

Figure 3.5: AO measurement of the 4×4 SHNO array with $(w, p) = (120, 300)$, measured at $\theta = 82°$. In contrast to the AO measured at $\theta = 76°$ shown in Figure 3.3j, the mode expansion at higher OOP angle enhances the interaction between the SHNOs over the entire array, allowing them all to operate in harmony.

It might seem that the synchronization of larger arrays with larger values of p is not feasible; however, as synchronization is all about tuning the coupling and the AO mode overlap, it is possible to synchronize certain arrays with larger values of p. For instance, the 4×4 array with $(w, p) = (120, 300)$ shown in Figure 3.3j does not exhibit global synchronization (although synchronization within its chains was achieved); however, if the array is measured at higher OOP angle (θ), as shown in Figure 3.5, the mode expansion provides a different configuration for the coupling between the oscillators, so that all SHNOs operate in unison, as predicted by Dvornik et al. [149]. The significance of

tunable coupling will be highlighted when oscillatory arrays are used for computing paradigms, where all the information is encoded in the coupling between the oscillators.

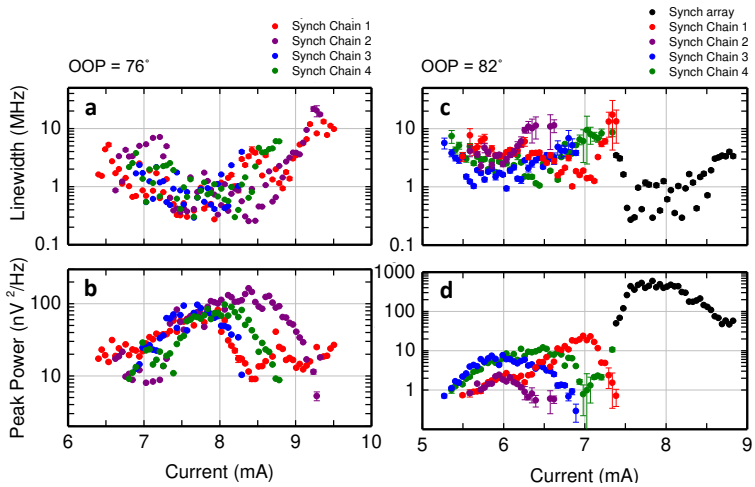

Figure 3.6: The 4×4 SHNO array with $(w, p) = (120, 300)$ measured at different θ; (a) and (c) linewidth analysis, and (b) and (d) peak power analysis, of the array for θ= 76° and θ = 82°, respectively.

The linewidth and peak power values for the 4×4 array measured at $\theta = 76°$ and $\theta = 82°$ are shown in Figure 3.6, of which panels a and b represent the extracted linewidth and peak power values for the PSD shown in Figure 3.3j for $\theta = 76°$. The four chains are associated with four individual frequency branches which approach each other with higher applied current, although they fail to synchronize as a whole. As the SHNOs within the chains synchronize, the linewidth of each frequency branch is improved (reaching about 200 kHz) for applied current values up to 8.5 mA, as shown in Figure 3.6a. Also, the peak power increases up to 150 nV^2/Hz, as Figure 3.6b depicts. However, there is no significant improvement in either the linewidth or the peak power, as global synchronization cannot be achieved. Once the measurement is done at $\theta = 82°$, the individual chains of SHNOs synchronize at 7.5 mA applied current. As Figure 3.6c indicates, the linewidth values experience a significant enhancement from the minimum value of 1 MHz for individual chains to about 200 kHz for the entire synchronized array—an improvement by a factor of five. On the other hand, as Figure 3.6d shows, the maximum peak power of a single chain increases from 20 nV^2/Hz to nearly 600 nV^2/Hz for the synchronized array, which represents a factor of 30 improvement.

We extracted the values for linewidth and peak power for all the SHNO arrays that achieved a robust synchronization at θ= 76° in Fig. 3.3. Figure 3.7 shows the extracted linewidth and peak power values for the arrays operating at the current values shown by the solid white lines in Figure 3.3. The green data points in Figure 3.7a represent the linewidth values corresponding to arrays

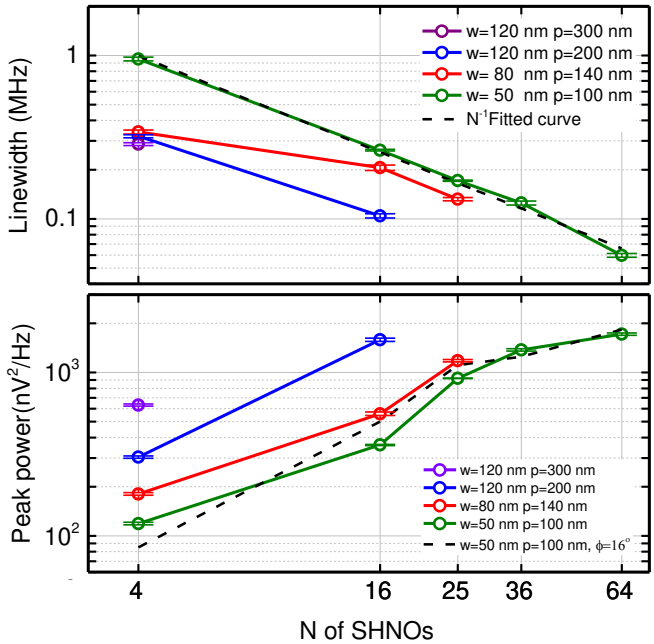

Figure 3.7: Linewidth and peak power values for SHNO arrays operating at synchronized state biased at DC current values, indicated by white solid lines in Figure 3.3. (a) Linewidth values of the arrays versus the number of the SHNOs in each array. (b) The extracted peak power values for the operating points shown in (a).

with $(w, p) = (50, 100)$ vs. array size. As can be seen, the linewidth improves as the array grows in size, provided the synchronization holds. Interestingly, the trend in the linewidth can be fitted perfectly with a $1/N$ function (the black dashed line) which is in excellent agreement with the theoretical predictions for how synchronization will improve the linewidth. Since the linewidth is inversely proportional to the total "intrinsic" SW internal power, the other data points representing the linewidth values for the arrays with larger values of w (the red, blue, and violet symbols) show much smaller linewidths and higher peak powers for the same number of SHNOs in the synchronized array. This behavior is consistent with the size of the precessing volume in the FM, which is greater for larger values of w. The bigger precessing volume thus leads to higher intrinsic SW internal power, and consequently to lower linewidth for arrays with larger values of w. Figure 3.7b shows the peak power values corresponding to the data points in Figure 3.7a. Again, the peak power increases as the array size grows for all the synchronized arrays. However, looking at the arrays with $(w,p) = (50, 100)$, the growth of the peak power does not follow a N^2 dependency. In theory, the N^2 dependency can be achieved if all of the oscillators are phase-locked with zero phase difference (shift);

however, in reality, there is likely a relative phase difference between the oscillators. This shift can originate from various sources, such as differences in the size of the oscillators, non–uniformity in the spin current density that drives each oscillator, and broken coupling symmetry at the edge of the arrays. All these factors cause distributions in the natural frequency of the SHNOs. By considering the mesa resistance (R_m), the individual nano–constriction resistance (R_c), the applied current (I_{dc}), and the array size, we use the relative phase shift $\delta\phi$ between neighboring chains and R_{ac} (the alternate resistance caused by AMR) as a fitting parameter to estimate the experimental peak power values. The calculated peak powers are shown in Figure 3.7b as a black dashed line that corresponds to a chain-to-chain relative phase shift of 16°. The black dashed line emphasizes the importance of phase difference on the peak power and explains why a growing phase shift can eventually lead to a rollover in the peak power as the array size scales.

3.3 Neuromorphic computing using 2D SHNO arrays

The use of oscillators in neuromorphic computing encompasses a wide and varied research field. In a very recent work, Romera et al. [129] used four vortex STNOs, electrically connected in series, for reservoir computing, achieving recognition of seven different vowels spoken by 35 speakers. Using a linear combination of 12 frequency components in the spoken vowels, they mapped the input frequencies into two RF signals injected into an antenna close to the STNO chain. The frequencies of one or more of the free-running STNOs became phase-locked to one or the other (or both) of the injected RF signals when their frequencies were close to the natural frequency of each STNO. Depending on how the STNOs injection–locked to the two RF signals, a two-dimensional synchronization map with synchronization regions corresponding to the seven different vowels was achieved.

Despite this exciting proof of concept, the proposed approach will be challenging to scale up in terms of number of STNOs. Their connections were provided by wire bonding, and the coupling between the oscillators was too weak for large scale-up. The demonstrated system was also based on vortex oscillators operating at 350 MHz. To reach a certain injection–locked state will require a certain number of periods, hence limiting the recognition speed significantly. There is therefore a need to both scale up and speed up these or similar systems if they will be used with more complex and more time–consuming tasks.

Here we want to demonstrate that our 2D SHNO arrays are able to reproduce the same synchronization maps, as shown in [129]. In the previous chapter, Figure 3.8b showed an array of 4×4 SHNOs, where the oscillators in each chain fall into an internally synchronized state, showing four distinct peaks (Fig. 3.8c). We will use these four chains as the four neurons, corresponding to the four vortex oscillators in [129]. Figure 3.8a illustrates the interaction between the two input signal neurons and the four individual neurons in our

2D array (in this case, chains) showing that the chains are coupled to their neighbors and also to the external signal. When we inject two microwave currents with frequencies f_A and f_B directly into the SHNO array, the same type of synchronization map can be reproduced, as shown in Figure 3.8d. To perform injection locking [169], we combined the two microwave signals (f_A and f_B) generated by two R&S SMB100A Microwave Signal Generators operating at frequency range close to $2f_{\mathrm{SHNO}}$. The combined signals were then fed to a microwave circulator connected to the RF port of the bias-tee to inject the two microwave signals directly to the SHNO array. The injected signals can strongly perturb the array and phase–lock to the individual chains when injected with enough power (*i.e.*, -2 dBm in our case) and at a frequency close to the chain's frequency. The injected signals,f_A and f_B, phase–lock with the second harmonic of the SHNOs, $2f_{\mathrm{SHNO}}$ while their sun–harmonics, $f_A/2$ and $f_B/2$ phase–lock with the SHNOs at f_{SHNO}. The output signal was then sent back through the RF port of the bias–tee and then to the third port of the circulator to the LNA before it was captured by SA. The injection locking at $2f_{\mathrm{SHNO}}$ range assures no damage to the LNA (amplifying the signal in 4-10 GHz range) caused by high power injected signals, f_A and f_B.

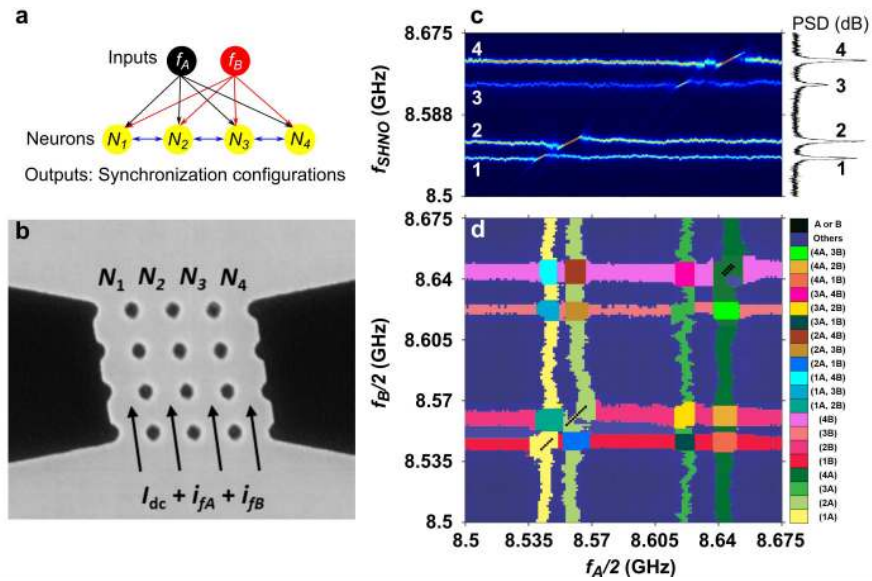

Figure 3.8: Demonstration of synchronization map with a 4×4 SHNO array. (a) Layout of the artificial neurons. While each neuron N_i is coupled to the neighboring neurons, they are all coupled to the external microwave signals f_A and f_B. (B) SEM image of the array, depicting each chain of SHNOs as a neuron. (C) the injection locking of N_1 to N_4 to f_A and f_B. (d) Map of different synchronization regions corresponding to oscillators locked to $f_A/2$ and $f_B/2$. A total of 20 distinct synchronization regions are mapped.

Figure 3.8c indicates the frequency locking range of each chain when it

locks to the $f_A/2$ signal. The locking range can also be seen by looking at the width of the stripes in Figure 3.8d. Our demonstration indicates the possibility of carrying out the same type of reservoir computing at frequencies up to 8.6 GHz, which is about 25 times faster than the case with STOs running at 350 MHz.

There have been many other proposals and approaches to using oscillator networks for different computation paradigms, including:

- Vortex coloring of graphs belonging to the class of combinatorial optimization problems with nondeterministic polynomial-time complexity, based on the oscillators' phase. [42]
- Oscillatory arrays with multilevel neurons for pattern recognition in the frequency domain. [43, 44]
- Auto-associative memory and pattern recognition with an oscillator network; this involves looking at the strength of synchronization defined by the output power, in which tuning the phases (the coupling in the Kuramoto model) will change the synchronization strength. [45–47]
- Oscillatory network based on a Kuramoto phase oscillator for image segmentation. Two interacting two-dimensional oscillator networks with different couplings within rows and within columns are used. [48, 170]
- Oscillator network-based Ising machine for solving combinatorial optimization problems. [49–51]

A two-dimensional network of interacting oscillators is the central feature of almost all of the proposed neuromorphic approaches to computing. It is particularly important to point out that all the approaches mentioned above require oscillator-to-oscillator coupling for their operation. The two-dimensional SHNO networks offer very strong coupling in both dimensions, and will encourage renewed interest and efforts in the hardware realization of the theoretical and simulation examples above. The input patterns are encoded in the coupling between the oscillators within 2D arrays (phases or natural frequencies), or by global coupling enforced by external means. In our case, the coupling between the oscillators in the 2D SHNO arrays is determined by dipolar and exchange interactions that are tunable by applied current and external field. Both dipolar and exchange interactions decay, with the distance leading to a predominant nearest– neighbor coupling. There are thus short-range and long-range coupling interactions, which are needed to imitate the synaptic coupling between neurons. To this end, the synaptic coupling between artificial neurons should be tunable individually, so that pairwise coupling can be strengthened or weakened.

The next chapter, therefore, describes how individual tuning of SHNOs can affect their frequency, their coupling, and even their synchronization to neighboring oscillators within a chain.

4

Voltage controlled SHNOs: The oscillator remembers

Manuscript VI & VII : In the earlier three chapters, we laid the foundation for coupled nanoscale spintronic oscillators, compatible with CMOS technology and scalable down to a few tens of nanometers. In this chapter, we will present the last piece of the puzzle needed to complete our foundation: the tuning of individual oscillators in an array and the tuning of their mutual coupling. This will be necessary if an oscillator network is to be used as an artificial neural network whose synaptic weights (or couplings) need to be adjusted during either the training process or when using the system.

In the work by Romera et al. [129], mentioned in the previous chapter, they took advantage of four individual STNOs, each having an individual DC bias line to tune their individual frequencies. Individual tuning of the STNOs allowed the synchronization map to be reconfigured and optimized to accommodate each ensemble of vowels inside a single synchronized region in the map, as shown in Figure 2a–d in [129]. By training the network with many vowel samples, and adjusting the synchronization map, the STNOs were able to recognize the test vowels with a recognition rate of up to 85%.

While we showed in the previous chapter that our 2D SHNO arrays were able to reproduce the same synchronization maps, they, too, could have benefited from individual tuning of the different chains. Moreover, individual tuning will essentially be required to perform almost any type of bioinspired computing. For this reason, we have to find or develop an efficient way to tune the frequency of our oscillators. As power efficiency demands less power consumption, applying an electric field via gating seems to be the best candidate, as the power consumption for tuning is determined by the leakage current through the dielectric material. If done properly, this leakage would be negligible.

In order to achieve individual tuning by voltage in our system, we need to find a material and structure whose properties are affected by the electric field caused by the voltage. One candidate was interface perpendicular magnetic anisotropy (PMA), as observed in our W/CoFeB/MgO-based SHNOs. The PMA at the CoFeB/oxide (mainly MgO) interface is one of the main driving forces behind MRAM technology, and it is known that both the PMA [171,

172] and the SW damping [171] can be controlled by applying a voltage to this interface.

Applying an electric field to the CoFeB/MgO interface with PMA modulates the charge or the spin density in the $3d$ orbitals of Fe. The $3d$ orbitals are hybridized with the $2p$ orbitals of the oxygen atoms. A relative change is introduced in the spin density of the occupied orbitals with the application of an electric field, which induces a change in the PMA [173]. In MTJs with perpendicular magnetized free layer, the demagnetization field is significantly compensated by the PMA emerging from the interface. The MRAM switching current density can thus be significantly reduced and the density of MRAM memory cells increased.

As we discussed in Section 1.1.3, the FMR frequency is determined by the effective field, which contains a term for the anisotropy, including the PMA. A change in the PMA is hence reflected as a change in the FMR frequency in the linear regime, which consequently also changes the AO frequency. The very first demonstration of frequency tunability for an SOT-driven oscillator was reported by Liu et. al [174]; in his work, a frequency change of 6 MHz/V was achieved. The oscillator consisted of a bilayer of NiFe/Pt gated through a 20-nm-thick AlO_x layer. The relatively small magnetic anisotropy induced at the NiFe/AlO_x interface results in a small AO frequency change, caused by the electric field. Hence, investigating the PMA in W/CoFeB/MgO stacks, where it is more strongly tunable by both the growth conditions and the applied voltage, seems to be a promising approach to satisfying the requirements.

In this chapter, we introduce SHNOs based on W/$(Co_{0.75}Fe_{.25})_{75}B_{25}$/MgO/$AlO_x$ and controlled by an electric field. This field, provided by the gating operation, is found to modulate both the Gilbert damping and the PMA of the ferromagnetic layer. Moreover, the voltage can force multiple oscillators to fall back-and-forth into a synchronized/non–synchronized state. The gating through the insulating layer also adds another functionality to the device: that of memristive switching of the gate insulator. Such memristive behavior gives our device the ability to remember the last input it was provided.

4.1 Sample fabrication

We started with five different stacks of W(5)/$(Co_{0.75}Fe_{.25})_{75}B_{25}$(1.7)/MgO(2) (thicknesses in nm), where the thickness of CoFeB was varied from 1.1 to 1.9 nm to obtain different levels of PMA. The MgO layer in all stacks was protected from ambient humidity by a 2 nm AlO_x layer.The stacks were subsequently annealed at 300 °C for 1 hour to induce PMA. The vibrating–sample magnetometer (VSM) technique was used in order to obtain the hysteresis loops of the magnetic stacks, as shown in Figure 4.1. Figure 4.1a and b show the hysteresis loops for out-of-plane and in-plane applied field, respectively. The figures in the bottom row represent the small field range for the figures in the upper row. From the figures, it is clear that only two thicknesses of CoFeB–1.9 nm (orange line) and 1.7 nm (green line)–provide in-plane magnetized films, although they both show very strong PMA. For

the 1.7 nm-thick CoFeB, the magnetization can be aligned perpendicularly to the film surface by applying a magnetic field of only a few hundred Oersted (bottom row in Figure 4.1a). The PMA strength can hence be very high, inducing a strong out-of-plane magnetized film that requires a very large in-plane magnetic field to make the magnetization lie in the film plane (i.e., CoFeB (1.1nm), black line in the upper row Figure 4.1b)

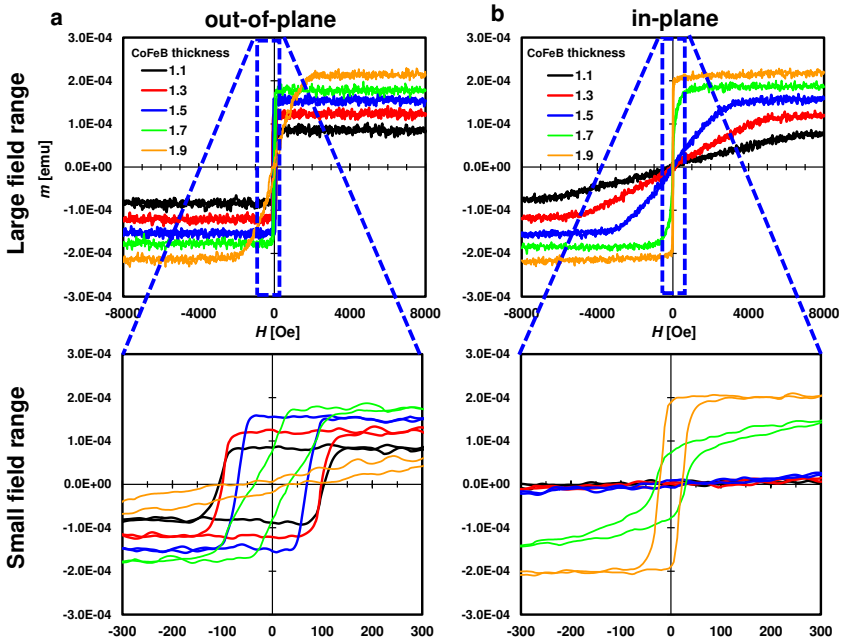

Figure 4.1: VSM measurement of W(5)/$(Co_{0.75}Fe_{.25})_{75}B_{25}$(t)/MgO(2)/$AlO_x$(2) (thicknesses in nm) stacks for (a) out-of-plane and (b) in-plane applied fields. The bottom row figures are magnified to show the smaller applied field range in the upper row.

For final fabrication, we chose the W(5)/$(Co_{0.75}Fe_{.25})_{75}B_{25}$(1.7)/MgO(2)/$AlO_x$(2) stack as it is an in-plane magnetized film with substantial PMA that almost compensates the demagnetization field entirely. The first step in the fabrication process to define the SHNO followed the process described in Section 1.2.1. The thickness of the HSQ was chosen such that, having etched the entire stack to the substrate, there was no HSQ (or only a thin layer) left on the AlO_x. The sample was then covered by 15 nm of sputtered silicon nitride Si_3N_4 to isolate the entire substrate and sample sidewalls from the top electrodes. In the next step, the gate line was defined by sputtering a bilayer of Ti(2 nm)/Cu(40 nm), followed by EBL using a thick layer of ma-N2400 negative resist as the etching mask. The pattern of the gate electrode was transferred to the Ti/Cu bilayer using the IBE technique. After removing the remaining negative resist, the sample went through optical lithography using

1.5 μm thick S1813 positive resist to define vias in Si_3N_4, giving access to the SHNO metal layers for the contact pads. Finally, the electrical contacts, including two SG-CPWs for microwave (the lower SG in Figure 4.2d) and DC (the upper SG in Figure 4.2d) measurements were defined by optical lithography and lift-off. Figure 4.2a and b show schematics of the fabricated device depicting the thickness and order of the layers.

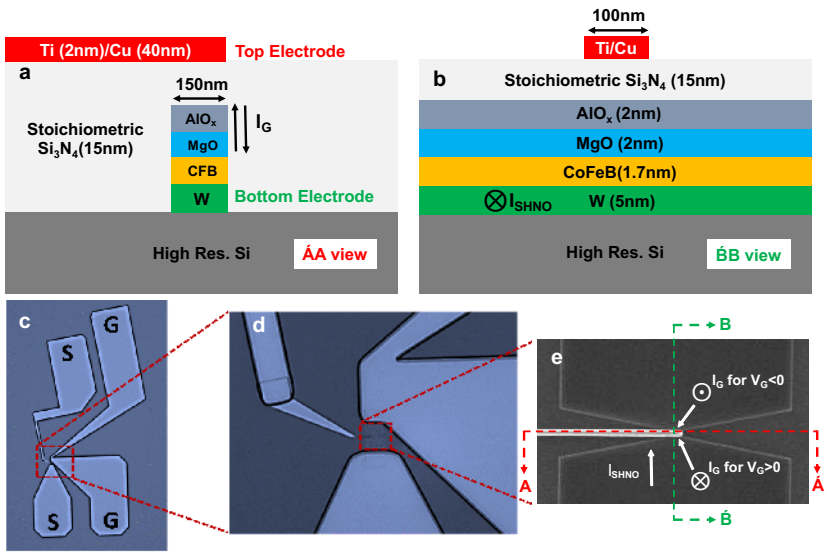

Figure 4.2: (a) and (b) schematic of the gated SHNO indicating the thickness of each layer, the constriction width, and the gate width. (c) Optical image of the fabricated devices with the top contacts for microwave measurements (bottom SG pads) and DC measurements (top SG pads). (d) Magnified image of the SHNO mesa. (e) SEM image of the SHNO with corresponding polarities for I_{SHNO}, V_G, and I_G.

4.2 Electrical measurement I: Voltage controlled PMA and damping

Figure 4.3a–c shows the AO measurements for different applied gate voltages. The positive gate voltage results in a reduction in the PMA (K_1), which translates as an increase in M_{eff} ($M_{\mathrm{eff}} = M_s - K_1 - K_2$), shown in the inset to Figure 4.3d. The FMR frequency thus decreases, as does the AO frequency. The same argument holds for negative gate voltages, resulting a blue-shift in the AO frequency (Fig. 4.3e). Figure 4.3d shows the reduction in the Gilbert damping constant when the voltage is swept from negative to positive values, which reflects itself into the auto-oscillation threshold current (see Fig. 4.3a–c). Experiments by other groups show the importance of oxygen ion migration

during the application of negative and positive gate voltages in FM/oxide interfaces [175, 176]. The migration of oxygen ions may explain the damping changes in our devices, as oxygen contributes to the formation of an over oxidized magnetic layer, increasing the intrinsic damping in the FM. Pulling the oxygen ions from the interface transforms the O-rich interface into an O-poor interface, enhancing the magnetic quality of the FM and reducing damping.

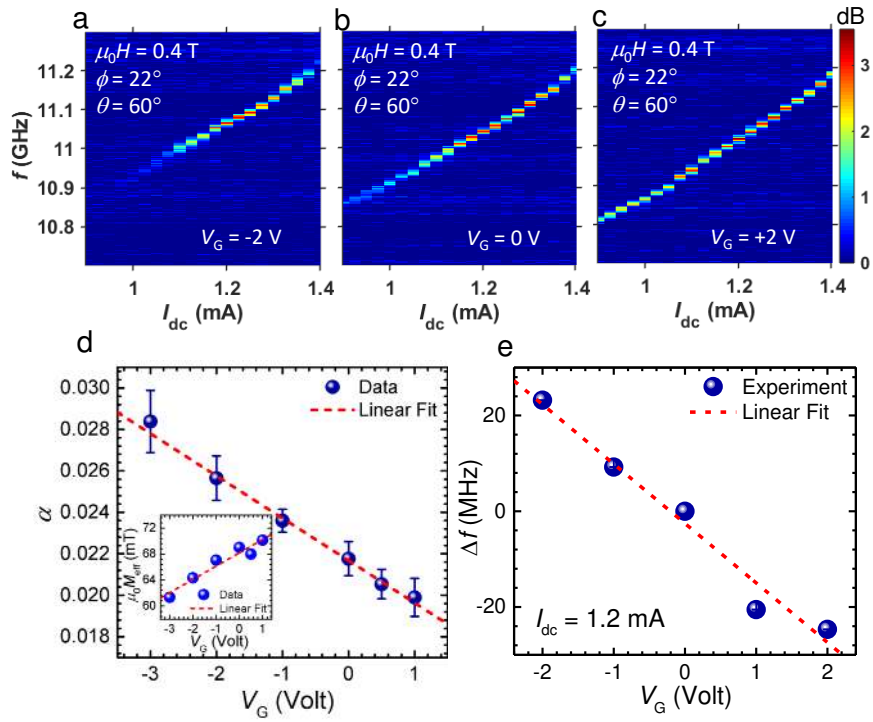

Figure 4.3: AO measurements of SHNOs for different gate voltages: (a) -2 V, (b) 0 V, and (c) +2 V. (d) Gilbert damping, M_{eff} (inset) modulation, and (e) frequency change versus the applied gate voltage.

4.3 Electrical measurement II: The gate is a memristor

During the electrical measurement, we observed that the maximum positive voltage that we can apply to the insulating layer before the gate dielectric breaks down is about +2 V. However, the limit for negative voltages without breakdown may be as much as -4 V. We later observed that, after a breakdown at a positive voltage, the gate dielectric recovers when a large negative voltage is applied. This process can be repeated indefinitely. Finally, we found that our multilayer dielectric material and its contacts,

W(5)/CoFeB(1.7/)MgO(2)/AlOx(2)/SiN_x(15)/Ti(2)/Cu(40), act as a tunable resistor in which the resistance state can be set by the current compliance when the dielectric multilayer breakdown occurs. It also turns out that the I–V curve of the gate crosses the origin. All these signs point towards our multilayer dielectric material being a memristor.

In the following, we will characterize the memristive behavior of our gate. We use the term V_m rather than V_G for the rest of the discussion in order to be consistent with the terms used for characterizing memristors. The memristor (gate) voltage was swept from -2 V to +2 V in the forward sweep, and from +2 V to -2 V in the backward sweep, in order to obtain the memristive behavior. During the forward sweep, the memristor behaves as an insulator, and the leakage current is in order of few nA; this corresponds to a high resistance state (HRS) of 0.12–1 GΩ. At a certain positive voltage, the memristor current (I_m) abruptly increases to the current compliance value (CC) set at the voltage source, reaching a low resistance state (LRS). This voltage is called V_{set}. The opposite value in the negative voltage range at which the memristor switches back to the HRS is called V_{reset}. Figure 4.4 shows the multilevel resistance levels achieved by setting different current compliance values (CC). The CC defines how large the conducting path is allowed to grow through the multilayer dielectric material. It thus sets the resistance of the conducting path. Higher CC values allow larger conducting paths; hence, smaller resistance values can be obtained. Note that the resistance state is defined by the slope of the linear region of each I–V curve crossing the origin.

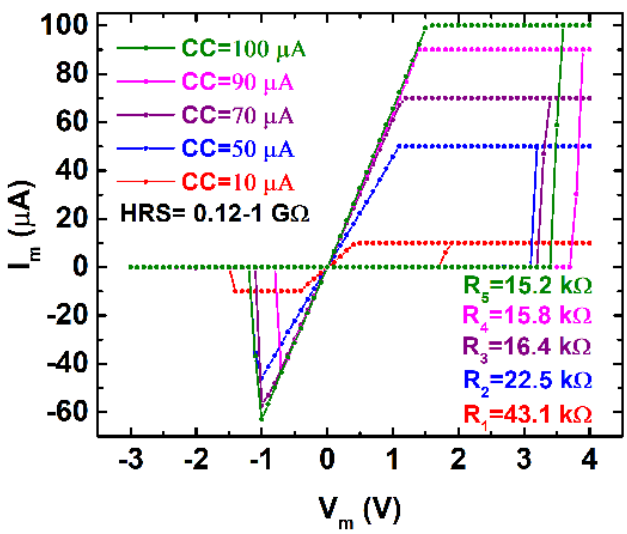

Figure 4.4: Multilevel memristive switching of the multilayer gate dielectric defined by different CCs to obtain HRS and LRSs.

Let us now examine how the memristor behavior affects the behavior of the

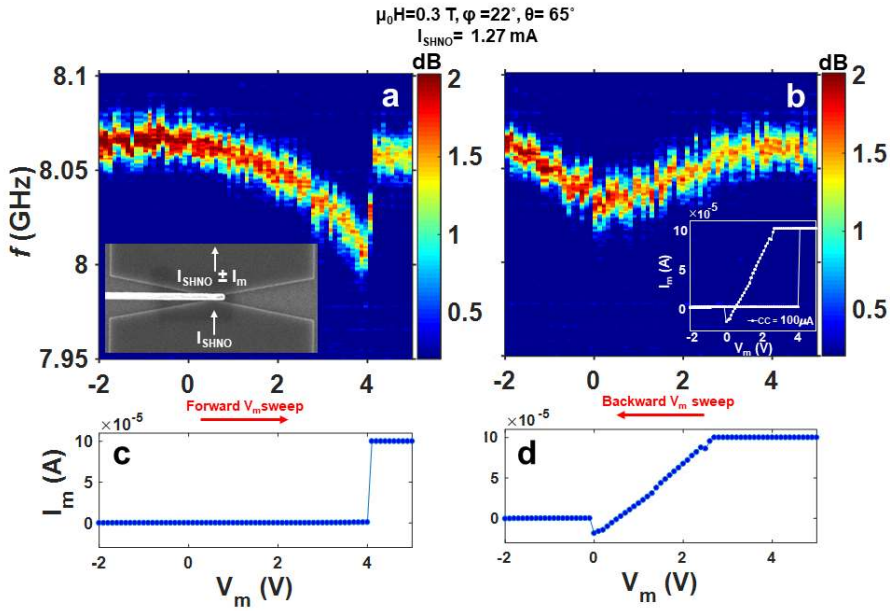

Figure 4.5: Memristive behavior of the fabricated gate affecting the SHNO AO. Effect of V_m on AO for (a) forward sweep. (b) backward sweep. Memristor current I_m for (c) forward and (d) backward sweeps. The inset in (a) shows the SHNO current and memristor current being added or subtracted from I_{SHNO}.

SHNO in the HRS and LRS regions. Figure 4.5a and b show the AO response of the SHNO corresponding to the memristive behavior of the fabricated gate on top of the SHNO. Figure 4.5c and d show the memristive switching for the forward and backward voltage sweeps, respectively, with the SHNO operating at $I_{\text{SHNO}} = 1.27$ mA. While the memristor is operating in its HRS (Fig. 4.5a), the frequency experiences a red-shift as V_m approaches the positive values, while I_m is a measure of the leakage current. At $V_m = 4$ V, the I_m abruptly increases to CC= 100 μA, and the AO frequency of the SHNO exhibits a jump, because a portion of the I_m is added to the I_{SHNO}. The new AO frequency corresponds to the memristor LRS set by the CC. In the backward sweep (Fig. 4.5b), the AO frequency undergoes a linear reduction in proportion to the resistance LRS state. The frequency decrease continues until V_m reaches V_{reset}, *i.e.* until the memristor re-enters its HRS. From V_{reset} to -2 V, a purely electric field-driven effect governs the frequency change. Note that the polarity of I_m can reach negative values, so the memristor shunts a portion of I_{SHNO}, as shown in Figure 4.5d.

By setting different resistant values for the memristor, we can map the frequency of SHNO to the memristor resistance states, HRS and LRS. What the memristor does in this way is to memorize the frequency of the SHNO as it

switches between different resistant states. Although the memristive switching mechanism in our structure is not well understood, a possible explanation is that oxygen ions migrate through the conductive filament consisting of metal atoms, as discussed in [177].

4.4 Electrical measurement III: Memristive control of mutual synchronization

As mentioned earlier, a purely electric field-driven change in the frequency of SHNO in the HRS region is expected, while the LRS region rules the frequency change by injecting or shunting some DC current to the SHNO. Both effects could allow us to control individual SHNOs in chains or arrays. To investigate this possibility, we fabricated SHNO chains with independent gates to individual constrictions.

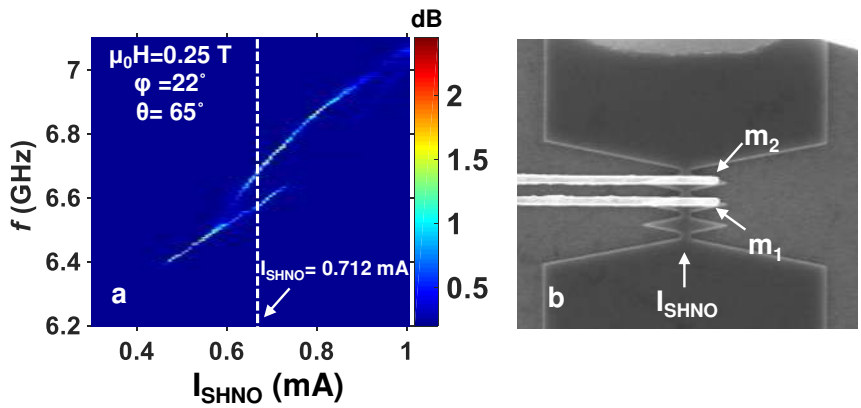

Figure 4.6: (a) Plot of AO PSD for I_{SHNO} sweep when no gate voltage is applied to m_1 and m_2. The synchronization breaks at larger I_{SHNO}. (b) SEM image of the SHNO showing m_1 and m_2 memristor top contacts.

We fabricated two gate contacts, m_1 and m_2, over the bridges connecting the second SHNO to the third one, and the third one to the fourth one, respectively (SEM image shown in Fig. 4.6b). The connecting bridges are the regions where the modes overlap, the interaction occurs, and the synchronization is initiated.

Figure 4.6a shows the AO profile of a chain of four SHNOs, in which the four oscillators are synchronized for low values of the I_{SHNO}, while the synchronization state breaks apart into two frequency branches for larger I_{SHNO}. To investigate the effect of the voltage while the memristor operates in HRS, we kept I_{SHNO} at 0.712 mA; under this operating condition, at least one oscillator operates out of the synchronized state. The memristor voltage, V_{m1} was swept from negative voltage to positive voltage in the forward sweep (shown under Fig. 4.7a by a red arrow). For the backward sweep, V_{m1} was

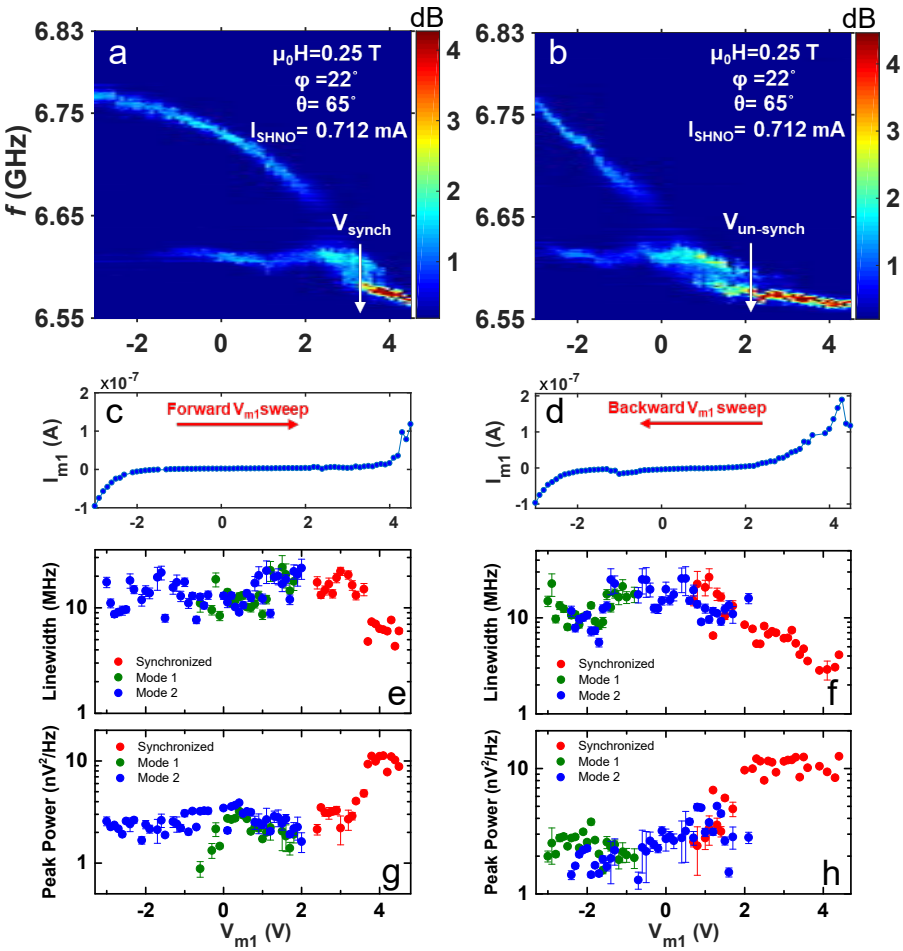

Figure 4.7: Effect of memristor voltage on the AO profile of four SHNOs in a chain. (a) and (b) the PSD plot for V_{m1} sweeps for constant $I_{\mathrm{SHNO}} = 0.712$ mA (dotted white line in Fig.4.6a). By sweeping V_{m1}, synchronization is regained at VV_{synch} in (a) and broken again at $\mathrm{V_{unsynch}}$ in (b). (c) and (d) $\mathrm{m_1}$ current versus the applied voltage for both forward and backward sweeps. (e)–(f) and (g)–(h) Linewidths and peak power plots corresponding to (a) and (b).

varied from positive values to the starting negative value from which the forward sweep began (shown in Fig. 4.7b). As can be seen, during the forward sweep, the upper frequency branch experiences a red-shift of as V_{m1} approaches positive values. The upper branch meets the lower frequency branch at $\mathrm{V_{synch}}$, where the synchronization occurs. Figure 4.7e and g reveal a noticeable drop in the linewidth and an increase in the peak power when the two frequency branches synchronize at $\mathrm{V_{synch}}$, and continue in unison for all larger positive voltages. A 203 MHz overall frequency change corresponding to 28 MHz/V is achieved in the forward sweep. In the backward sweep (Fig. 4.7b), the

oscillators seem to remain synchronized even for V_{m1} lower than V_{synch}. The extended synchronization range is also confirmed by Figure 4.7f and h, in which the linewidth and peak power remain improved until $V_{unsynch}$, at which the synchronized state collapses. Note that, for both sweeps shown in Figure 4.7, the memristor current I_{m1} is measured and plotted in Figure 4.7c and d. Since I_{m1} did not show any absolute value greater than 150 nA, the memristor was believed to be operating in the HRS.

In this chapter, we have shown how adding a gate to the top of an SHNO not only allows tuning of the frequency of the individual oscillator, but can also produce modulation in the damping constant. Adding a memristive gate offers an embedded memory on top of the oscillator, which can either manipulate or remember the previous frequency states of the device. Moreover, when it comes to the chains and arrays of SHNOs, gating is a very feasible route for tuning the coupling. The approach we have discussed here paves the way toward implementing all computing paradigms based on coupled oscillatory networks that require individual tuning. In oscillatory coupled network computation, all the information is encoded in the coupling between the oscillators, and a tiny change in the state of one oscillator is reflected throughout the entire array through its effects on the coupling landscape.

5

Future approaches and prospects

This thesis has provided all the building blocks needed for a range of technology-ready spin-based oscillators. It began with the introduction of a high–throughput high-resolution EBL process. The thesis then described CMOS-compatible SHNOs, optimizing their operating conditions for low power consumption, wideband operating frequency, tunable propagating SW emitters, and large coupled networks of oscillators. Finally, we dealt with means of connecting voltage–controlled inputs to the oscillators for tuning, controlled synchronization, and turning them on and off at will.

From the fabrication point of view, the HSQ standard process has the reproducibility required to produce very large two-dimensional SHNO arrays. However, we expect the future of such arrays to involve MTJs embedded on top, in order to significantly enhance the output power through TMR. In MTJ fabrication, vertical cylindrical pillars are defined with minimum deviation on the edges. The resist used as the etching mask should be sufficiently thick to withstand the plasma etching for the MTJ stacks, which can consist of ten or more layers. We thus need a process that offers sufficiently thick resist as an etching mask and with minimum compromise on resolution, contrast, and ease of processing. We believe that the HSQ high-contrast process proposed in the first chapter is the means to satisfy these requirements. There is thus the considerable potential to improve the fabrication process, leading to a significant impact on device performance.

Power consumption is important for future integration with CMOS. Hf dusting of SHNOs can reduce the current density, showing that there is room for further optimization. Decreasing the current density is particularly important for large oscillator arrays, where the heat generated in nanoscale regions can severely affect the device stability and reproducibility. We introduced W/CoFeB/MgO stacks in order to improve device performance even further. These stacks not only achieve a spin Hall angle of 53%—pushing the SHNO deep into the sub-milliampere operational regime—but they also offer an MRAM-industry-friendly approach for future integration. W/CoFeB/MgO-based SHNOs offer broad frequency tunability thanks to

the emerging PMA at the CoFeB/MgO interface. If the SHNOs are provided with sufficient PMA, they can also be used as emitters of propagating SWs with the wavelength–tunable by the applied current or the magnetic field. Propagating SWs are of interest to many research groups working on magnonic and wave-based computing. SWs are promising candidates for implementing ultrafast spin-based logic gates and magnonic waveguides that do not suffer from a diffraction limit on scaling, as optical waveguides do. We can now discover how propagating SWs facilitate the synchronization of larger chains and arrays of SHNOs. SHNO synchronization assisted by SW propagation is a whole new approach to research into the coupling mechanism and the robustness of synchronization.

We have shown nonlinear frequency and amplitude modulation using SHNOs. Modulation is one of the most common functions in communication systems, where it is performed by bulky and power-hungry semiconductor-based oscillators. Embedding a nanoscale oscillator capable of operating as a modulator is a step forward to achieving compact communication systems. Predicting the behavior of the modulation using the NFAM model gives us guidelines for designing the demodulator at the receiver end. The next step is to implement an extended design to optimize other parameters, such as modulation index, maximum achievable bandwidth, efficiency, and noise.

The two-dimensional synchronization of SHNOs is a leap forward in realizing tunable microwave sources operating at GHz frequencies with unprecedented signal coherency, achieving a Q factor of 170,000. Though the output power of these arrays is not very high, since the output is based on AMR, the next step will be to integrate MTJs and using TMR readout so as to boost the output power significantly. Signal coherency can be maintained once the MTJs share the free layers through which they synchronize. MRAM foundries already offer commercial MTJ processing down to a few tens of nanometers. Moving towards 2D arrays of W/CoFeB/MgO— the building blocks of future MTJ-SHNOs—would be imperative. Using such arrays, it would be possible to study synchronization for both SW bullets and propagating SWs. MTJ-SHNOs can serve as excellent replacements for bulky semiconductor-based oscillators once the output power, linewidth, and frequency stability criteria are met.

The most exciting phenomenon in 2D SHNO arrays, as described in Chapter 3, is the interaction between oscillators, which forces them to operate partially or entirely in unison once sufficient coupling is provided. Each SHNO can be considered as a neuron operating at microwave frequency and connected to neighboring neurons via magnetic interaction. Networks of coupled oscillators can in this way emulate neuronal activities to perform some operations that the Von Neumann paradigm is not optimized for. Coupled-oscillator network computation is based on the principle "***let the physics do the computing***": all information is encoded in the couplings (interactions) between the oscillators and the oscillators' state (frequency or phase). Note that inputting and tuning a processing unit based on oscillatory networks requires access to individual oscillators. In Chapter 4, we introduced a possible path toward tuning the oscillators within a chain; this can be easily extended to two-dimensional arrays.

Having all the necessary ingredients, we believe that the time has come to take the next step towards investigating different computing paradigms for the coupled network of oscillators, and to show how analog SHNO devices can outperform conventional CMOS units by mimicking the way that the brain processes information and by harnessing multicore operation and parallelism at a speed of tens of GHz.

Bibliography

[1] M. N. Baibich, J. M. Broto, A. Fert, F. N. Van Dau, F. Petroff, P. Etienne, G. Creuzet, A. Friederich, and J. Chazelas, "*Giant magnetoresistance of (001) Fe/(001) Cr magnetic superlattices*", Physical review letters **61**, 2472 (1988).

[2] G. Binasch, P. Grünberg, F. Saurenbach, and W. Zinn, "*Enhanced magnetoresistance in layered magnetic structures with antiferromagnetic interlayer exchange*", Physical review B **39**, 4828 (1989).

[3] O. Golonzka, J.-G. Alzate, U. Arslan, M. Bohr, P. Bai, J. Brockman, B. Buford, C. Connor, N. Das, B. Doyle, et al., "*MRAM as embedded non-volatile memory solution for 22FFL FinFET technology*", in 2018 IEEE International Electron Devices Meeting (IEDM) (IEEE, 2018), pp. 18–1.

[4] Y. K. Lee, Y. Song, J. Kim, S. Oh, B.-J. Bae, S. Lee, J. Lee, U. Pi, B. Seo, H. Jung, et al., "*Embedded STT-MRAM in 28-nm FDSOI logic process for industrial MCU/IoT application*", in 2018 IEEE Symposium on VLSI Technology (IEEE, 2018), pp. 181–182.

[5] J. Åkerman, "*Toward a universal memory*", Science **308**, 508–510 (2005).

[6] X. Dong, X. Wu, G. Sun, Y. Xie, H. Li, and Y. Chen, "*Circuit and microarchitecture evaluation of 3D stacking magnetic RAM (MRAM) as a universal memory replacement*", in 2008 45th ACM/IEEE Design Automation Conference (IEEE, 2008), pp. 554–559.

[7] J. Akerman, P. Brown, M. DeHerrera, M. Durlam, E. Fuchs, D. Gajewski, M. Griswold, J. Janesky, J. J. Nahas, and S. Tehrani, "*Demonstrated reliability of 4-Mb MRAM*", IEEE Transactions on Device and Materials Reliability **4**, 428–435 (2004).

[8] S. Tsunegi, T. Taniguchi, R. Lebrun, K. Yakushiji, V. Cros, J. Grollier, A. Fukushima, S. Yuasa, and H. Kubota, "*Scaling up electrically synchronized spin torque oscillator networks*", Scientific reports **8**, 13475 (2018).

[9] A. Awad, P. Dürrenfeld, A. Houshang, M. Dvornik, E. Iacocca, R. Dumas, and J. Åkerman, "*Long-range mutual synchronization of spin Hall nano-oscillators*", Nature Physics **13**, 292 (2017).

[10] P. Dürrenfeld, A. A. Awad, A. Houshang, R. K. Dumas, and J. Åkerman, "*A 20 nm spin Hall nano-oscillator*", Nanoscale **9**, 1285–1291 (2017).

[11] M. Haidar, A. A. Awad, M. Dvornik, R. Khymyn, A. Houshang, and J. Åkerman, "*A single layer spin-orbit torque nano-oscillator*", Nature communications **10**, 2362 (2019).

[12] M. Tarequzzaman, A. Jenkins, T. Böhnert, J. Borme, L. Martins, E. Paz, R. Ferreira, and P. Freitas, "*Broadband voltage rectifier induced by linear bias dependence in CoFeB/MgO magnetic tunnel junctions*", Applied Physics Letters **112**, 252401 (2018).

[13] A. Tulapurkar, Y. Suzuki, A. Fukushima, H. Kubota, H. Maehara, K. Tsunekawa, D. Djayaprawira, N. Watanabe, and S. Yuasa, "*Spin-torque diode effect in magnetic tunnel junctions*", Nature **438**, 339 (2005).

[14] A. Awad, S. Muralidhar, R. Alemán Ademir.and Khymyn, M. Dvornik, D. Lu, D. Hanstorp, and J. Åkerman, "*Stimulated k–vector selective magnon emission in NiFe films using femtosecond laser pulse trains*", arXiv preprint arXiv:1908.03388 (2019).

[15] H. Fulara, M. Zahedinejad, R. Khymyn, A. Awad, S. Muralidhar, M. Dvornik, and J. Åkerman, "*Spin-Orbit-Torque Driven Propagating Spin Waves*", arXiv preprint arXiv:1904.06945 (2019).

[16] P. K. Muduli, Y. Pogoryelov, S. Bonetti, G. Consolo, F. Mancoff, and J. Åkerman, "*Nonlinear frequency and amplitude modulation of a nanocontact-based spin-torque oscillator*", Physical Review B **81**, 140408 (2010).

[17] M. Zahedinejad, A. A. Awad, P. Dürrenfeld, A. Houshang, Y. Yin, P. K. Muduli, and J. Åkerman, "*Current Modulation of Nanoconstriction Spin-Hall Nano-Oscillators*", IEEE Magn. Lett. **8**, 1–4 (2017).

[18] Y. Pogoryelov, P. Muduli, S. Bonetti, E. Iacocca, F. Mancoff, and J. Åkerman, "*Frequency modulation of spin torque oscillator pairs*", Applied Physics Letters **98**, 192501 (2011).

[19] Y. Pogoryelov, P. Muduli, S. Bonetti, F. Mancoff, and J. Åkerman, "*Spin-torque oscillator linewidth narrowing under current modulation*", Applied Physics Letters **98**, 192506 (2011).

[20] P. Muduli, Y. Pogoryelov, Y. Zhou, F. Mancoff, and J. Åkerman, "*Spin torque oscillators and RF currents—Modulation, locking, and ringing*", Integrated Ferroelectrics **125**, 147–154 (2011).

[21] P. Muduli, Y. Pogoryelov, F. Mancoff, and J. Akerman, "*Modulation of individual and mutually synchronized nanocontact-based spin torque oscillators*", IEEE transactions on magnetics **47**, 1575–1579 (2011).

[22] R. Sharma, P. Dürrenfeld, M. Ranjbar, R. Dumas, J. Åkerman, and P. Muduli, "*Modulation rate study in a spin-torque oscillator-based wireless communication system*", IEEE Transactions on Magnetics **51**, 1–4 (2015).

[23] R. Sharma, N. Sisodia, E. Iacocca, A. A. Awad, J. Åkerman, and P. Muduli, "*A high-speed single sideband generator using a magnetic tunnel junction spin torque nano-oscillator*", Scientific reports **7**, 13422 (2017).

[24] J. C. Slonczewski, "*Current-driven excitation of magnetic multilayers*", Journal of Magnetism and Magnetic Materials **159**, L1–L7 (1996).

[25] S. Bonetti, V. Tiberkevich, G. Consolo, G. Finocchio, P. Muduli, F. Mancoff, A. Slavin, and J. Åkerman, "*Experimental evidence of self-localized and propagating spin wave modes in obliquely magnetized current-driven nanocontacts*", Physical review letters **105**, 217204 (2010).

[26] S. Bonetti, V. Puliafito, G. Consolo, V. S. Tiberkevich, A. N. Slavin, and J. Åkerman, "*Power and linewidth of propagating and localized modes in nanocontact spin-torque oscillators*", Physical Review B **85**, 174427 (2012).

[27] M. Madami, S. Bonetti, G. Consolo, S. Tacchi, G. Carlotti, G. Gubbiotti, F. Mancoff, M. A. Yar, and J. Åkerman, "*Direct observation of a propagating spin wave induced by spin-transfer torque*", Nature nanotechnology **6**, 635 (2011).

[28] M. Madami, E. Iacocca, S. Sani, G. Gubbiotti, S. Tacchi, R. Dumas, J. Åkerman, and G. Carlotti, "*Propagating spin waves excited by spin-transfer torque: A combined electrical and optical study*", Physical Review B **92**, 024403 (2015).

[29] A. Slavin and V. Tiberkevich, "*Spin wave mode excited by spin-polarized current in a magnetic nanocontact is a standing self-localized wave bullet*", Physical review letters **95**, 237201 (2005).

[30] V. E. Demidov, S. Urazhdin, and S. O. Demokritov, "*Direct observation and mapping of spin waves emitted by spin-torque nano-oscillators*", Nature materials **9**, 984 (2010).

[31] R. K. Dumas, E. Iacocca, S. Bonetti, S. Sani, S. M. Mohseni, A. Eklund, J. Persson, O. Heinonen, and J. Åkerman, "*Spin-wave-mode coexistence on the nanoscale: a consequence of the oersted-field-induced asymmetric energy landscape*", Physical review letters **110**, 257202 (2013).

[32] S. M. Mohseni, S. Sani, J. Persson, T. A. Nguyen, S. Chung, Y. Pogoryelov, P. Muduli, E. Iacocca, A. Eklund, R. Dumas, et al., "*Spin torque–generated magnetic droplet solitons*", Science **339**, 1295–1298 (2013).

[33] F. Macià, D. Backes, and A. D. Kent, "*Stable magnetic droplet solitons in spin-transfer nanocontacts*", Nature nanotechnology **9**, 992 (2014).

[34] S. Kaka, M. R. Pufall, W. H. Rippard, T. J. Silva, S. E. Russek, and J. A. Katine, "*Mutual phase-locking of microwave spin torque nano-oscillators*", Nature **437**, 389 (2005).

[35] A. Houshang, E. Iacocca, P. Dürrenfeld, S. Sani, J. Åkerman, and R. Dumas, "*Spin-wave-beam driven synchronization of nanocontact spin-torque oscillators*", Nature nanotechnology **11**, 280 (2016).

[36] S. Sani, J. Persson, S. M. Mohseni, Y. Pogoryelov, P. Muduli, A. Eklund, G. Malm, M. Käll, A. Dmitriev, and J. Åkerman, "*Mutually synchronized bottom-up multi-nanocontact spin–torque oscillators*", Nature communications **4**, 2731 (2013).

[37] V. E. Demidov, S. Urazhdin, H. Ulrichs, V. Tiberkevich, A. Slavin, D. Baither, G. Schmitz, and S. O. Demokritov, "*Magnetic nano-oscillator driven by pure spin current*", Nature materials **11**, 1028 (2012).

[38] V. Demidov, S. Urazhdin, A. Zholud, A. Sadovnikov, and S. Demokritov, "*Nanoconstriction-based spin-Hall nano-oscillator*", Applied Physics Letters **105**, 172410 (2014).

[39] M. Zahedinejad, A. A. Awad, S. Muralidhar, R. Khymyn, H. Fulara, H. Mazraati, M. Dvornik, and J. Åkerman, "*Two-dimensional mutual synchronization in spin Hall nano-oscillator arrays*", arXiv preprint arXiv:1812.09630 (2018).

[40] T. M. Spicer, P. S. Keatley, M. Dvornik, T. H. Loughran, A. Awad, P. Dürrenfeld, A. Houshang, M. Ranjbar, J. Åkerman, V. V. Kruglyak, et al., "*Time resolved imaging of the non-linear bullet mode within an injection-locked nano-contact spin Hall nano-oscillator*", Applied Physics Letters **113**, 192405 (2018).

[41] T. M. Spicer, P. S. Keatley, T. H. Loughran, M. Dvornik, A. Awad, P. Dürrenfeld, A. Houshang, M. Ranjbar, J. Åkerman, V. V. Kruglyak, et al., "*Spatial mapping of torques within a spin Hall nano-oscillator*", Physical Review B **98**, 214438 (2018).

[42] A. Parihar, N. Shukla, M. Jerry, S. Datta, and A. Raychowdhury, "*Vertex coloring of graphs via phase dynamics of coupled oscillatory networks*", Scientific reports **7**, 911 (2017).

[43] A. Velichko, M. Belyaev, and P. Boriskov, "*A Model of an Oscillatory Neural Network with Multilevel Neurons for Pattern Recognition and Computing*", Electronics **8**, 75 (2019).

[44] T. Zhang, M. Haider, Y. Massoud, and J. Alexander, "*An Oscillatory Neural Network Based Local Processing Unit for Pattern Recognition Applications*", Electronics **8**, 64 (2019).

[45] A. Kumar and P. Mohanty, "*Autoassociative memory and pattern recognition in micromechanical oscillator network*", Scientific reports **7**, 411 (2017).

[46] D. E. Nikonov, G. Csaba, W. Porod, T. Shibata, D. Voils, D. Hammerstrom, I. A. Young, and G. I. Bourianoff, "*Coupled-oscillator associative memory array operation for pattern recognition*", IEEE Journal on Exploratory Solid-State Computational Devices and Circuits **1**, 85–93 (2015).

[47] Y. Fang, V. V. Yashin, S. P. Levitan, and A. C. Balazs, "*Pattern recognition with "materials that compute"*", Science advances **2**, e1601114 (2016).

[48] A. Novikov and E. Benderskaya, "*Oscillatory network based on Kuramoto model for image segmentation*", in International Conference on Parallel Computing Technologies (Springer, 2015), pp. 210–221.

[49] T. Wang, L. Wu, and J. Roychowdhury, "*New Computational Results and Hardware Prototypes for Oscillator-based Ising Machines*", in Proceedings of the 56th Annual Design Automation Conference 2019 (ACM, 2019), p. 239.

[50] T. Wang and J. Roychowdhury, "*OIM: Oscillator-based Ising Machines for Solving Combinatorial Optimisation Problems*", arXiv preprint arXiv:1903.07163 (2019).

[51] I. Mahboob, H. Okamoto, and H. Yamaguchi, "*An electromechanical Ising Hamiltonian*", Science advances **2**, e1600236 (2016).

[52] T. McGuire and R. Potter, "*Anisotropic magnetoresistance in ferromagnetic 3d alloys*", IEEE Transactions on Magnetics **11**, 1018–1038 (1975).

[53] M. N. Baibich, J. M. Broto, A. Fert, F. N. Van Dau, F. Petroff, P. Etienne, G. Creuzet, A. Friederich, and J. Chazelas, "*Giant magnetoresistance of (001) Fe/(001) Cr magnetic superlattices*", Physical review letters **61**, 2472 (1988).

[54] J. S. Moodera, L. R. Kinder, T. M. Wong, and R. Meservey, "*Large magnetoresistance at room temperature in ferromagnetic thin film tunnel junctions*", Physical review letters **74**, 3273 (1995).

[55] M. Zahedinejad, H. Mazraati, H. Fulara, J. Yue, S. Jiang, A. A. Awad, and J. Åkerman, "*CMOS compatible W/CoFeB/MgO spin Hall nano-oscillators with wide frequency tunability*", Appl. Phys. Lett. **112**, 132404 (2018).

[56] M. Zhang, X. Wang, F. Song, and R. Zhang, "*Layered Topological Insulators and Semimetals for Magnetoresistance Type Sensors*", Advanced Quantum Technologies **2**, 1800039 (2019).

[57] M. D'yakonov and V. Perel, "*Possibility of orienting electron spins with current*", Soviet Journal of Experimental and Theoretical Physics Letters **13**, 467 (1971).

[58] M. Dyakonov and V. Perel, "*Current-induced spin orientation of electrons in semiconductors*", Physics Letters A **35**, 459–460 (1971).

[59] J. Hirsch, "*Spin hall effect*", Physical Review Letters **83**, 1834 (1999).

[60] A. Bakun, B. Zakharchenya, A. Rogachev, M. Tkachuk, and V. Fleisher, "*Detection of a surface photocurrent due to electron optical orientation in a semiconductor*", Sov. Phys. JETP Lett **40**, 1293 (1984).

[61] L. Liu, T. Moriyama, D. Ralph, and R. Buhrman, "*Spin-torque ferromagnetic resonance induced by the spin Hall effect*", Physical review letters **106**, 036601 (2011).

[62] C.-F. Pai, L. Liu, Y. Li, H.-W. Tseng, D. C. Ralph, and R. A. Buhrman, "*Spin transfer torque devices utilizing the giant spin Hall effect of tungsten*", Applied Physics Letters **101**, 122404 (2012).

[63] H. Mazraati, S. Chung, A. Houshang, M. Dvornik, L. Piazza, F. Qejvanaj, S. Jiang, T. Q. Le, J. Weissenrieder, and J. Åkerman, "*Low operational current spin Hall nano-oscillators based on NiFe/W bilayers*", Appl. Phys. Lett. **109**, 242402 (2016).

[64] L. Liu, C.-F. Pai, Y. Li, H. Tseng, D. Ralph, and R. Buhrman, "*Spin-torque switching with the giant spin Hall effect of tantalum*", Science **336**, 555–558 (2012).

[65] Z. Tang, Y. Kitamura, E. Shikoh, Y. Ando, T. Shinjo, and M. Shiraishi, "*Temperature dependence of spin hall angle of palladium*", Applied Physics Express **6**, 083001 (2013).

[66] N. H. D. Khang, Y. Ueda, and P. N. Hai, "*A conductive topological insulator with large spin Hall effect for ultralow power spin–orbit torque switching*", Nature materials, 1 (2018).

[67] P. Laczkowski, Y. Fu, H. Yang, J.-C. Rojas-Sánchez, P. Noel, V. Pham, G. Zahnd, C. Deranlot, S. Collin, C. Bouard, et al., "*Large enhancement of the spin Hall effect in Au by side-jump scattering on Ta impurities*", Physical Review B **96**, 140405 (2017).

[68] L. D. Landau, *Collected papers of LD Landau* (Pergamon, 1965).

[69] T. L. Gilbert, "*A phenomenological theory of damping in ferromagnetic materials*", IEEE transactions on magnetics **40**, 3443–3449 (2004).

[70] N. Nakajima, T. Koide, T. Shidara, H. Miyauchi, H. Fukutani, A. Fujimori, K. Iio, T. Katayama, M. Nývlt, and Y. Suzuki, "*Perpendicular magnetic anisotropy caused by interfacial hybridization via enhanced orbital moment in Co/Pt multilayers: Magnetic circular x-ray dichroism study*", Physical Review Letters **81**, 5229 (1998).

[71] J.-H. Park, C. Park, T. Jeong, M. T. Moneck, N. T. Nufer, and J.-G. Zhu, "*Co/ Pt multilayer based magnetic tunnel junctions using perpendicular magnetic anisotropy*", Journal of Applied Physics **103**, 07A917 (2008).

[72] T. Kato, Y. Matsumoto, S. Kashima, S. Okamoto, N. Kikuchi, S. Iwata, O. Kitakami, and S. Tsunashima, "*Perpendicular anisotropy and Gilbert damping in sputtered Co/Pd multilayers*", IEEE Transactions on Magnetics **48**, 3288–3291 (2012).

[73] M. Sicot, S. Andrieu, F. Bertran, and F. Fortuna, "*Electronic properties of Fe, Co, and Mn ultrathin films at the interface with MgO (001)*", Physical Review B **72**, 144414 (2005).

[74] T. Maruyama, Y. Shiota, T. Nozaki, K. Ohta, N. Toda, M. Mizuguchi, A. Tulapurkar, T. Shinjo, M. Shiraishi, S. Mizukami, et al., "*Large voltage-induced magnetic anisotropy change in a few atomic layers of iron*", Nature nanotechnology **4**, 158 (2009).

[75] Y. Shiota, T. Maruyama, T. Nozaki, T. Shinjo, M. Shiraishi, and Y. Suzuki, "*Voltage-assisted magnetization switching in ultrathin Fe80Co20 alloy layers*", Applied Physics Express **2**, 063001 (2009).

[76] J. Sinha, M. Hayashi, A. J. Kellock, S. Fukami, M. Yamanouchi, H. Sato, S. Ikeda, S. Mitani, S.-h. Yang, S. S. Parkin, et al., "*Enhanced interface perpendicular magnetic anisotropy in Ta/ CoFeB/ MgO using nitrogen doped Ta underlayers*", Applied Physics Letters **102**, 242405 (2013).

[77] A. Manchon, C. Ducruet, L. Lombard, S. Auffret, B. Rodmacq, B. Dieny, S. Pizzini, J. Vogel, V. Uhlíř, M. Hochstrasser, et al., "*Analysis of oxygen induced anisotropy crossover in Pt/Co/M Ox trilayers*", Journal of Applied Physics **104**, 043914 (2008).

[78] S. Ikeda, K. Miura, H. Yamamoto, K. Mizunuma, H. Gan, M. Endo, S. Kanai, J. Hayakawa, F. Matsukura, and H. Ohno, "*A perpendicular-anisotropy CoFeB–MgO magnetic tunnel junction*", Nature materials **9**, 721 (2010).

[79] Y. Ou, D. Ralph, and R. Buhrman, "*Strong perpendicular magnetic anisotropy energy density at Fe alloy/HfO2 interfaces*", Applied Physics Letters **110**, 192403 (2017).

[80] B. Rodmacq, A. Manchon, C. Ducruet, S. Auffret, and B. Dieny, "*Influence of thermal annealing on the perpendicular magnetic anisotropy of Pt/Co/AlOx trilayers*", Physical Review B **79**, 024423 (2009).

[81] G. Yu, L.-T. Chang, M. Akyol, P. Upadhyaya, C. He, X. Li, K. L. Wong, P. K. Amiri, and K. L. Wang, "*Current-driven perpendicular magnetization switching in Ta/CoFeB/[TaOx or MgO/TaOx] films with lateral structural asymmetry*", Applied Physics Letters **105**, 102411 (2014).

[82] W. Kim, J. Jeong, Y. Kim, W. Lim, J. Kim, J. Park, H. Shin, Y. Park, K. Kim, S. Park, et al., "*Extended scalability of perpendicular STT-MRAM towards sub-20nm MTJ node*", in 2011 International Electron Devices Meeting (IEEE, 2011), pp. 24–1.

[83] T. Chen, R. K. Dumas, A. Eklund, P. K. Muduli, A. Houshang, A. A. Awad, P. Dürrenfeld, B. G. Malm, A. Rusu, and J. Åkerman, "*Spin-torque and spin-Hall nano-oscillators*", Proceedings of the IEEE **104**, 1919–1945 (2016).

[84] W. Zhang, W. Han, X. Jiang, S.-H. Yang, and S. S. Parkin, "*Role of transparency of platinum–ferromagnet interfaces in determining the intrinsic magnitude of the spin Hall effect*", Nature Physics **11**, 496 (2015).

[85] C.-F. Pai, Y. Ou, L. H. Vilela-Leão, D. Ralph, and R. Buhrman, "*Dependence of the efficiency of spin Hall torque on the transparency of Pt/ferromagnetic layer interfaces*", Physical Review B **92**, 064426 (2015).

[86] J.-C. Rojas-Sánchez, N. Reyren, P. Laczkowski, W. Savero, J.-P. Attané, C. Deranlot, M. Jamet, J.-M. George, L. Vila, and H. Jaffrès, "*Spin pumping and inverse spin Hall effect in platinum: the essential role of spin-memory loss at metallic interfaces*", Physical review letters **112**, 106602 (2014).

[87] Y. Liu, Z. Yuan, R. J. Wesselink, A. A. Starikov, and P. J. Kelly, "*Interface enhancement of Gilbert damping from first principles*", Physical review letters **113**, 207202 (2014).

[88] L. Liu, C.-F. Pai, D. Ralph, and R. Buhrman, "*Magnetic oscillations driven by the spin Hall effect in 3-terminal magnetic tunnel junction devices*", Physical review letters **109**, 186602 (2012).

[89] M. Ranjbar, P. Drrenfeld, M. Haidar, E. Iacocca, M. Balinskiy, T. Le, M. Fazlali, A. Houshang, A. Awad, R. Dumas, et al., "*CoFeB-based spin Hall nano-oscillators*", IEEE Magnetics Letters **5**, 1–4 (2014).

[90] Z. Duan, A. Smith, L. Yang, B. Youngblood, J. Lindner, V. E. Demidov, S. O. Demokritov, and I. N. Krivorotov, "*Nanowire spin torque oscillator driven by spin orbit torques*", Nature communications **5**, 5616 (2014).

[91] A. Slavin and V. Tiberkevich, "*Nonlinear auto-oscillator theory of microwave generation by spin-polarized current*", IEEE Transactions on Magnetics **45**, 1875–1918 (2009).

[92] A. Slavini and P. Kabos, "*Approximate theory of microwave generation in a current-driven magnetic nanocontact magnetized in an arbitrary direction*", IEEE Transactions on Magnetics **41**, 1264–1273 (2005).

[93] C. Huygens, *Letters to de Sluse,(letters; no. 1333 of 24 February 1665, no. 1335 of 26 February 1665, no. 1345 of 6 March 1665)*, 1895.

[94] M. Bennett, M. F. Schatz, H. Rockwood, and K. Wiesenfeld, "*Huygens's clocks*", Proceedings of the Royal Society of London. Series A: Mathematical, Physical and Engineering Sciences **458**, 563–579 (2002).

[95] B. Van der Pol, *A theory of the amplitude of free and forced triode vibrations, Radio Rev. 1 (1920) 701-710, 754-762; Selected Scientific Papers, vol. I*, 1960.

[96] Y. Kuramoto, "*International symposium on mathematical problems in theoretical physics*", Lecture notes in Physics **30**, 420 (1975).

[97] Y. Kuramoto, *Chemical oscillations, waves, and turbulence* (Courier Corporation, 2003).

[98] F. Mancoff, N. Rizzo, B. Engel, and S. Tehrani, "*Phase-locking in double-point-contact spin-transfer devices*", Nature **437**, 393 (2005).

[99] A. Ruotolo, V. Cros, B. Georges, A. Dussaux, J. Grollier, C. Deranlot, R. Guillemet, K. Bouzehouane, S. Fusil, and A. Fert, "*Phase-locking of magnetic vortices mediated by antivortices*", Nature nanotechnology **4**, 528 (2009).

[100] W. H. Rippard, M. R. Pufall, S. Kaka, T. J. Silva, and S. E. Russek, "*Current-driven microwave dynamics in magnetic point contacts as a function of applied field angle*", Physical Review B **70**, 100406 (2004).

[101] L. Chua, "*Memristor-the missing circuit element*", IEEE Transactions on circuit theory **18**, 507–519 (1971).

[102] D. B. Strukov, G. S. Snider, D. R. Stewart, and R. S. Williams, "*The missing memristor found*", nature **453**, 80 (2008).

[103] R. Stanley Williams, "*How we found the missing memristor*", in *Chaos, CNN, Memristors and Beyond: A Festschrift for Leon Chua With DVD-ROM, composed by Eleonora Bilotta* (World Scientific, 2013), pp. 483–489.

[104] J. J. Yang, M. D. Pickett, X. Li, D. A. Ohlberg, D. R. Stewart, and R. S. Williams, "*Memristive switching mechanism for metal/oxide/metal nanodevices*", Nature nanotechnology **3**, 429 (2008).

[105] B. Mohammad, M. A. Jaoude, V. Kumar, D. M. Al Homouz, H. A. Nahla, M. Al-Qutayri, and N. Christoforou, "*State of the art of metal oxide memristor devices*", Nanotechnology Reviews **5**, 311–329 (2016).

[106] S. G. Kim, J. S. Han, H. Kim, S. Y. Kim, and H. W. Jang, "*Recent Advances in Memristive Materials for Artificial Synapses*", Advanced Materials Technologies **3**, 1800457 (2018).

[107] R. Pan, J. Li, F. Zhuge, L. Zhu, L. Liang, H. Zhang, J. Gao, H. Cao, B. Fu, and K. Li, "*Synaptic devices based on purely electronic memristors*", Applied Physics Letters **108**, 013504 (2016).

[108] M. H. B. Jamaa, S. Carrara, J. Georgiou, N. Archontas, and G. De Micheli, "*Fabrication of memristors with poly-crystalline silicon nanowires*", in 2009 9th IEEE Conference on Nanotechnology (IEEE-NANO) (IEEE, 2009), pp. 152–154.

[109] M. D. Pickett, G. Medeiros-Ribeiro, and R. S. Williams, "*A scalable neuristor built with Mott memristors*", Nature materials **12**, 114 (2013).

[110] Z. Yang, C. Ko, and S. Ramanathan, "*Oxide electronics utilizing ultrafast metal-insulator transitions*", Annual Review of Materials Research **41**, 337–367 (2011).

[111] S. Lequeux, J. Sampaio, V. Cros, K. Yakushiji, A. Fukushima, R. Matsumoto, H. Kubota, S. Yuasa, and J. Grollier, "*A magnetic synapse: multilevel spin-torque memristor with perpendicular anisotropy*", Scientific reports **6**, 31510 (2016).

[112] A. F. Vincent, J. Larroque, W. Zhao, N. B. Romdhane, O. Bichler, C. Gamrat, J.-O. Klein, S. Galdin-Retailleau, and D. Querlioz, "*Spin-transfer torque magnetic memory as a stochastic memristive synapse*", in 2014 IEEE International Symposium on Circuits and Systems (ISCAS) (IEEE, 2014), pp. 1074–1077.

[113] C. D. Wright, L. Wang, M. M. Aziz, J. A. V. Diosdado, and P. Ashwin, "*Phase-change processors, memristors and memflectors*", physica status solidi (b) **249**, 1978–1984 (2012).

[114] T. Tuma, A. Pantazi, M. Le Gallo, A. Sebastian, and E. Eleftheriou, "*Stochastic phase-change neurons*", Nature nanotechnology **11**, 693 (2016).

[115] P. Dürrenfeld, *Spin torque and spin Hall nano-oscillators with single magnetic layers* (2015).

[116] A. Houshang, "*Synchronization Phenomena in Spin Torque and Spin Hall Nano-Oscillators*", (2017).

[117] A. E. Grigorescu, M. C. van der Krogt, and C. W. Hagen, "*Sub-10-nm structures written in ultra-thin HSQ resist layers using electron-beam lithography*", in Advances in Resist Materials and Processing Technology XXIV, Vol. 6519 (International Society for Optics and Photonics, 2007), 65194A.

[118] L. Mollard, G. Cunge, S. Tedesco, B. Dal'zotto, and J. Foucher, "*HSQ hybrid lithography for 20 nm CMOS devices development*", Microelectronic engineering **61**, 755–761 (2002).

[119] I.-B. Baek, J.-H. Yang, W.-J. Cho, C.-G. Ahn, K. Im, and S. Lee, "*Electron beam lithography patterning of sub-10 nm line using hydrogen silsesquioxane for nanoscale device applications*", Journal of Vacuum Science & Technology B: Microelectronics and Nanometer Structures Processing, Measurement, and Phenomena **23**, 3120–3123 (2005).

[120] M. Rommel, B. Nilsson, P. Jedrasik, V. Bonanni, A. Dmitriev, and J. Weis, "*Sub-10 nm resolution after lift-off using HSQ/PMMA double layer resist*", Microelectronic Engineering **110**, 123–125 (2013).

[121] J. K. Yang and K. K. Berggren, "*Using high-contrast salty development of hydrogen silsesquioxane for sub-10-nm half-pitch lithography*", Journal of Vacuum Science & Technology B: Microelectronics and Nanometer Structures Processing, Measurement, and Phenomena **25**, 2025–2029 (2007).

[122] J. Sankey, P. Braganca, A. Garcia, I. Krivorotov, R. Buhrman, and D. Ralph, "*Spin-transfer-driven ferromagnetic resonance of individual nanomagnets*", Physical review letters **96**, 227601 (2006).

[123] H. Mazraati, "Linear, Non-Linear, and Synchronizing Spin Wave Modes in Spin Hall Nano-Oscillators", PhD thesis (KTH Royal Institute of Technology, 2018).

[124] S. O. Demokritov, B. Hillebrands, and A. N. Slavin, "*Brillouin light scattering studies of confined spin waves: linear and nonlinear confinement*", Phys. Rep. **348**, 441–489 (2001).

[125] C. Wang, Y.-T. Cui, J. Sun, J. Katine, R. Buhrman, and D. Ralph, "*Sensitivity of spin-torque diodes for frequency-tunable resonant microwave detection*", Journal of Applied Physics **106**, 053905 (2009).

[126] S. Shi, Y. Ou, S. Aradhya, D. Ralph, and R. Buhrman, "*Fast low-current spin-orbit-torque switching of magnetic tunnel junctions through atomic modifications of the free-layer interfaces*", Physical Review Applied **9**, 011002 (2018).

[127] M. Wang, W. Cai, D. Zhu, Z. Wang, J. Kan, Z. Zhao, K. Cao, Z. Wang, Y. Zhang, T. Zhang, et al., "*Field-free switching of a perpendicular magnetic tunnel junction through the interplay of spin–orbit and spin-transfer torques*", Nature electronics **1**, 582 (2018).

[128] N. H. D. Khang, Y. Ueda, and P. N. Hai, "*A conductive topological insulator with large spin Hall effect for ultralow power spin–orbit torque switching*", Nature materials, 1 (2018).

[129] M. Romera, P. Talatchian, S. Tsunegi, F. A. Araujo, V. Cros, P. Bortolotti, J. Trastoy, K. Yakushiji, A. Fukushima, H. Kubota, et al., "*Vowel recognition with four coupled spin-torque nano-oscillators*", Nature **563**, 230 (2018).

[130] W. A. Borders, H. Akima, S. Fukami, S. Moriya, S. Kurihara, Y. Horio, S. Sato, and H. Ohno, "*Analogue spin–orbit torque device for artificial-neural-network-based associative memory operation*", Applied Physics Express **10**, 013007 (2016).

[131] D. Fan, S. Maji, K. Yogendra, M. Sharad, and K. Roy, "*Injection-locked spin hall-induced coupled-oscillators for energy efficient associative computing*", IEEE Transactions on Nanotechnology **14**, 1083–1093 (2015).

[132] X. Liu, W. Zhang, M. J. Carter, and G. Xiao, "*Ferromagnetic resonance and damping properties of CoFeB thin films as free layers in MgO-based magnetic tunnel junctions*", Journal of Applied Physics **110**, 033910 (2011).

[133] S. Mizukami, Y. Ando, and T. Miyazaki, "*Ferromagnetic resonance linewidth for NM/80NiFe/NM films (NM= Cu, Ta, Pd and Pt)*", Journal of magnetism and magnetic materials **226**, 1640–1642 (2001).

[134] Y. Tserkovnyak, A. Brataas, and G. E. Bauer, "*Enhanced Gilbert damping in thin ferromagnetic films*", Physical review letters **88**, 117601 (2002).

[135] M. L. Polianski and P. W. Brouwer, "*Current-Induced Transverse Spin-Wave Instability in a Thin Nanomagnet*", Phys. Rev. Lett. **92**, 026602 (2004).

[136] L. Zhu, D. Ralph, and R. Buhrman, "*Spin-Orbit Torques in Heavy-Metal–Ferromagnet Bilayers with Varying Strengths of Interfacial Spin-Orbit Coupling*", Physical review letters **122**, 077201 (2019).

[137] M. W. Keller, K. S. Gerace, M. Arora, E. K. Delczeg-Czirjak, J. M. Shaw, and T. Silva, "*Near-unity spin Hall ratio in N i x C u 1- x alloys*", Physical Review B **99**, 214411 (2019).

[138] H. Mazraati, M. Zahedinejad, and J. Åkerman, "*Improving the magnetodynamical properties of NiFe/Pt bilayers through Hf dusting*", Applied Physics Letters **113**, 092401 (2018).

[139] M.-H. Nguyen, C.-F. Pai, K. X. Nguyen, D. A. Muller, D. C. Ralph, and R. A. Buhrman, "*Enhancement of the anti-damping spin torque efficacy of platinum by interface modification*", Applied Physics Letters **106**, 222402 (2015).

[140] Y. Ou, C.-F. Pai, S. Shi, D. Ralph, and R. Buhrman, "*Origin of fieldlike spin-orbit torques in heavy metal/ferromagnet/oxide thin film heterostructures*", Physical Review B **94**, 140414 (2016).

[141] K. Jabeur and G. Prenat, "*Design of a full 1Mb STT-MRAM based on advanced FDSOI technology*", in MATEC Web of Conferences, Vol. 125 (EDP Sciences, 2017), p. 01003.

[142] Q. Hao and G. Xiao, "*Giant spin Hall effect and switching induced by spin-transfer torque in a W/Co 40 Fe 40 B 20/MgO structure with perpendicular magnetic anisotropy*", Physical Review Applied **3**, 034009 (2015).

[143] M. Cecot, Ł. Karwacki, W. Skowroński, J. Kanak, J. Wrona, A. Żywczak, L. Yao, S. van Dijken, J. Barnaś, and T. Stobiecki, "*Influence of intermixing at the Ta/CoFeB interface on spin Hall angle in Ta/CoFeB/MgO heterostructures*", Scientific reports **7**, 968 (2017).

[144] M. Siegal, W. Graham, and J. Santiago, Journal of Applied Physics **66**, 6073–6076 (1989).

[145] S. Cohen, P. Piacente, G. Gildenblat, and D. Brown, Journal of Applied Physics **53**, 8856–8862 (1982).

[146] S. P. Murarka, Intermetallics **3**, 173–186 (1995).

[147] C. Zhang, S. Fukami, K. Watanabe, A. Ohkawara, S. DuttaGupta, H. Sato, F. Matsukura, and H. Ohno, "*Critical role of W deposition condition on spin-orbit torque induced magnetization switching in nanoscale W/CoFeB/MgO*", Applied Physics Letters **109**, 192405 (2016).

[148] S. Peng, M. Wang, H. Yang, L. Zeng, J. Nan, J. Zhou, Y. Zhang, A. Hallal, M. Chshiev, K. L. Wang, et al., Scientific reports **5**, 18173 (2015).

[149] M. Dvornik, A. A. Awad, and J. Åkerman, "*Origin of Magnetization Auto-Oscillations in Constriction-Based Spin Hall Nano-Oscillators*", Physical Review Applied **9**, 014017 (2018).

[150] V. Kruglyak, S. Demokritov, and D. Grundler, "*Magnonics*", Journal of Physics D: Applied Physics **43**, 264001 (2010).

[151] S. Neusser and D. Grundler, "*Magnonics: spin waves on the nanoscale*", Advanced Materials **21**, 2927–2932 (2009).

[152] V. Demidov, M. Kostylev, K. Rott, J. Münchenberger, G. Reiss, and S. Demokritov, "*Excitation of short-wavelength spin waves in magnonic waveguides*", Applied Physics Letters **99**, 082507 (2011).

[153] Y. Yin, F. Pan, M. Ahlberg, M. Ranjbar, P. Dürrenfeld, A. Houshang, M. Haidar, L. Bergqvist, Y. Zhai, R. K. Dumas, et al., "*Tunable permalloy-based films for magnonic devices*", Physical Review B **92**, 024427 (2015).

[154] S. Bonetti and J. Åkerman, "*Nano-contact spin-torque oscillators as magnonic building blocks*", in *Magnonics* (Springer, 2013), pp. 177–187.

[155] B. Lenk, H. Ulrichs, F. Garbs, and M. Münzenberg, "*The building blocks of magnonics*", Physics Reports **507**, 107–136 (2011).

[156] S. Klingler, P. Pirro, T. Brächer, B. Leven, B. Hillebrands, and A. V. Chumak, "*Design of a spin-wave majority gate employing mode selection*", Applied Physics Letters **105**, 152410 (2014).

[157] B. Divinskiy, V. E. Demidov, S. O. Demokritov, A. B. Rinkevich, and S. Urazhdin, "*Route toward high-speed nano-magnonics provided by pure spin currents*", en, Appl. Phys. Lett. **109**, 252401 (2016).

[158] Y. Zhou and J. Åkerman, "*Perpendicular spin torque promotes synchronization of magnetic tunnel junction based spin torque oscillators*", Applied Physics Letters **94**, 112503 (2009).

[159] R. K. Dumas, S. R. Sani, S. M. Mohseni, E. Iacocca, Y. Pogoryelov, P. K. Muduli, S. Chung, P. Dürrenfeld, and J. Åkerman, "*Recent advances in nanocontact spin-torque oscillators*", IEEE transactions on magnetics **50**, 1–7 (2014).

[160] Y. Penn, M. Segal, and E. Moses, "*Network synchronization in hippocampal neurons*", Proceedings of the National Academy of Sciences **113**, 3341–3346 (2016).

[161] J. Veit, R. Hakim, M. P. Jadi, T. J. Sejnowski, and H. Adesnik, "*Cortical gamma band synchronization through somatostatin interneurons*", Nature Neuroscience **20**, 951 (2017).

[162] J. Buck, "*Synchronous rhythmic flashing of fireflies. II.*", The Quarterly review of biology **63**, 265–289 (1988).

[163] L. Glass, "*Synchronization and rhythmic processes in physiology*", Nature **410**, 277 (2001).

[164] W. Zhou, S. Slivken, and M. Razeghi, "*Phase-locked, high power, mid-infrared quantum cascade laser arrays*", Applied Physics Letters **112**, 181106 (2018).

[165] Y. Fang, V. V. Yashin, S. P. Levitan, and A. C. Balazs, "*Pattern recognition with "materials that compute"*", Science Advances **2**, e1601114 (2016).

[166] K. Segall, M. LeGro, S. Kaplan, O. Svitelskiy, S. Khadka, P. Crotty, and D. Schult, "*Synchronization dynamics on the picosecond time scale in coupled Josephson junction neurons*", Physical Review E **95**, 032220 (2017).

[167] M. A. Galin, E. A. Borodianskyi, V. Kurin, I. Shereshevskiy, N. Vdovicheva, V. M. Krasnov, and A. Klushin, "*Synchronization of Large Josephson-Junction Arrays by Traveling Electromagnetic Waves*", Physical Review Applied **9**, 054032 (2018).

[168] Y. Li, X. De Milly, O. Klein, V. Cros, J. Grollier, and G. De Loubens, "*Selective control of vortex polarities by microwave field in two robustly synchronized spin-torque nano-oscillators*", Applied Physics Letters **112**, 022405 (2018).

[169] Y. Zhou, J. Persson, and J. Åkerman, "*Intrinsic phase shift between a spin torque oscillator and an alternating current*", Journal of applied Physics **101**, 09A510 (2007).

[170] T. Raiko and H. Valpola, "*Oscillatory neural network for image segmentation with biased competition for attention*", in *From brains to systems* (Springer, 2011), pp. 75–85.

[171] A. Okada, S. Kanai, M. Yamanouchi, S. Ikeda, F. Matsukura, and H. Ohno, "*Electric-field effects on magnetic anisotropy and damping constant in Ta/CoFeB/MgO investigated by ferromagnetic resonance*", Applied Physics Letters **105**, 052415 (2014).

[172] W.-G. Wang, M. Li, S. Hageman, and C. L. Chien, "*Electric-field-assisted switching in magnetic tunnel junctions*", en, Nature Materials **11**, 64–68 (2012).

[173] K. Miura, S. Yabuuchi, M. Yamada, M. Ichimura, B. Rana, S. Ogawa, H. Takahashi, Y. Fukuma, and Y. Otani, "*Voltage-induced magnetization dynamics in CoFeB/MgO/CoFeB magnetic tunnel junctions*", Scientific reports **7**, 42511 (2017).

[174] R. Liu, L. Chen, S. Urazhdin, Y. Du, et al., "*Controlling the Spectral Characteristics of a Spin-Current Auto-Oscillator with an Electric Field*", Physical Review Applied **8**, 021001 (2017).

[175] R. Mishra, F. Mahfouzi, D. Kumar, K. Cai, M. Chen, X. Qiu, N. Kioussis, and H. Yang, "*Electric-field control of spin accumulation direction for spin-orbit torques*", Nature communications **10**, 248 (2019).

[176] R. Mishra, D. Kumar, and H. Yang, "*Oxygen-Migration-Based Spintronic Device Emulating a Biological Synapse*", Physical Review Applied **11**, 054065 (2019).

[177] Y. Zhang, H. Wu, Y. Bai, A. Chen, Z. Yu, J. Zhang, and H. Qian, "*Study of conduction and switching mechanisms in Al/AlOx/WOx/W resistive switching memory for multilevel applications*", Applied Physics Letters **102**, 233502 (2013).